Macromolecules in Disordered Environments: From Flexible to Semiflexible Polymers

Von der Fakultät für Physik und Geowissenschaften
der Universität Leipzig
genehmigte
D I S S E R T A T I O N
zur Erlangung des akademischen Grades

Doctor Rerum Naturalium
Dr. rer. nat.,

vorgelegt

von Dipl.-Phys. Sebastian Schöbl
geboren am 11.09.1981 in Zeitz.

Gutachter: Prof. Dr. Wolfhard Janke, Universität Leipzig
Dr. Henri Orland, C.E.A. Saclay

Tag der Verleihung: 18. März 2013

Bibliographische Informationen

Schöbl, Sebastian
Macromolecules in Disordered Environments:
From Flexible to Semiflexible Polymers
Universität Leipzig, Dissertation
123 S., 105 Lit., 73 Abb., 3 Tab.

Referat:

This work is a numerical examination of a semiflexible polymer exposed to a disorder landscape consisting of hard disks. For a small parameter range and simple constraints it is known that disorder leads to structural transitions of the equilibrium properties of polymers. The scope of this work strongly extends this range by going to both high disorder densities and large stiffnesses of the polymers. The competing length scales of polymer stiffness and average distance between the obstacles of the potential along with the way of assembling the disorder lead to a wide range of effects such as crumpling and stretching of polymer configurations due to the disorder or a modulation of the polymer's characterizing observables with the correlation function of the potential. The high accuracy results presented in this work have been obtained by means of sophisticated Monte Carlo simulations. The refinement of a rarely applied but highly promising method to a state of the art algorithm in connection with latest numerical techniques made it possible to investigate the impact of hard-disk disorder on semiflexible polymer conformations on a broad scale.

Contents

List of Figures

List of Tables

1. Introduction

1.1. Preface

Polymers, in simple terms large molecules composed of repeating structural units (monomers), have obtained great importance from the early 1900s on. A big variety of materials and drugs contain polymers or polymeric derivatives. Furthermore, the understanding of polymeric systems has brought deep insight into the structure of matter. Generally spoken, polymers have become an integral constituent to many fields and the research interest on them is on the increase. One of those subjects that has become extremely prominent is biophysics.

Metrological advances during the last twenty years facilitated direct measurements of the properties of polymers and polymer networks [1, 2] or even of single molecules [3]. Among them are techniques using magnetic beads [4] and optical tweezers [5], as well as optical tracking for single polymers [6, 7] and light scattering methods for polymer networks [8]. The experiments suggest that the mechanical properties—in addition to biochemical processes—of polymers play a crucial role for the basic structure and functionality of cells, the fundamental building blocks of nature and life. An example is the cytoskeleton [9], a multifunctional scaffold providing mechanical stability to eukaryotic cells. It is a network consisting of polymers. Experiments and measurements [10, 11, 12, 13] show, that the mechanical properties of these systems can well be described by coarse-grained models, even though on a microscopic scale they are built up of interacting molecules.

The polymer models that describe the purely mechanical part—especially bending (except for the flexible model)—of polymers can be divided into three classes, flexible, semiflexible, and stiff polymers. The characterizing length scale is the *persistence length* ℓ_p. It is defined as the length within that the tangent vectors along the contour of a polymer become decorrelated by thermal fluctuations. On length scales shorter than the persistence length, polymers behave as stiff rods, whereas on longer scales they exhibit flexible behavior. The characteristic length scale is due to the competition between thermal fluctuations, tending to overcome local structures, and the bending energy, trying to reduce energy by aspiring a rod-like conformation. The two limiting cases—flexible and stiff—have been discussed in great detail throughout literature. The theoretical model that describes the flexible limit is called freely jointed chain[1] [14]; the stiff limit is captured by the *weakly bending rod* (WBR) [15]. Extensive analytical calculations are for the most part restricted to the two limiting cases. Experiments, however, suggest that the biologically relevant range reaches from semi-

[1] The related continuum model is the Gaussian chain.

flexible to stiff polymers [16, 17]. Prominent examples are microtubules, intermediate filaments, and actin filaments, which assemble the complex polymer scaffold which maintains the stability and integrity of eukaryotic cells. These three types are typical representatives of semiflexible polymers having a persistence length on the order of 10^{-1}–$10^{3}\mu$m [18, 19, 20, 17, 21]. The canonical model for semiflexible polymers is the *wormlike chain*, also called Kratky-Porod model [22].

1.2. Polymers in their natural environment

The above-mentioned models, the freely jointed chain, the wormlike chain, and its stiff limit, the weakly bending rod, describe a coarse-grained view on isolated polymers. The common situation, however, is mainly determined by interaction of the polymers with their (natural) environment. On the one hand these interactions are energetic, as for the case of crosslinkers, on the other hand they are caused by geometrical constraints constituted, e.g., by other macromolecules. The latter type of interaction is commonly referred to as "steric". Consequently, the physical models that describe the experimental situations must involve those interactions.

Experiments on transport phenomena and polymers in porous media [23, 24, 25] already required theoretical models for flexible polymers in disordered systems in the 1980s. Since then these models have been widely discussed. Cates and Ball [26] examined the statistics of a Gaussian chain polymer without excluded volume in a quenched random potential modelled as Gaussian white noise (GWN), for two and three dimensions. Quenched refers to the way of performing the average over different disorder realizations in order to be independent of the special choice of a single realization. The time scale of disorder fluctuations is assumed to be much larger than that of the polymer for the case of quenched disorder. The disorder is thus kept fixed for a single equilibrium average of the polymer. This is in contrast to the annealed average, where polymer and disorder fluctuations are on the same time scale. This work considers solely quenched averages. Cates and Ball claim and show by calculating the free energy that the polymer shrinks to a region which has lower energy than its neighbors. Repeating this argument for a polymer that is pinned at one end leads to a tadpole-shaped conformation. The polymer coils up in the local energy minimum around its pinpoint only stretching out a single branch to reach it. This shriveling was also found by Edwards and Muthukumar [27]. Further approaches for flexible polymers were made in, e.g., [28, 29, 30, 31, 32, 33], to quote only a few of them. Considering additionally self-avoiding interaction was done by, e.g., Goldschmidt and Shiferaw [34] or Machta and Kirkpatrick [35].

In spite of the biological relevance of semiflexible polymer networks, as for example the cytoskeleton, much less attention has been devoted to semiflexible polymers, yet. An early approach to treat semiflexible polymer networks analytically was proposed by Edwards [36]. In his model, the so-called tube model, the complex network consists of an entangled solution of polymers. The network-induced confining forces that act on a single polymer are modeled as tube-like cages with a width that depends on the

density of the network and on the stiffness of the polymers. De Gennes described the movement of the polymers that escape from the tubes as slow snake-like motion called reptation [37]. He considered the situation of a polymer in a landscape of impenetrable objects. The idea to assume the network to act on a single component as perturbing disorder potential was taken up by Hinsch and Frey [38] who examined the behavior of a semiflexible polymer exposed to impenetrable topological constraints. They were thus able to reproduce the curvature distribution of a polymer in a polymer network. With their theoretical description they built up on an experimental investigation of the influence of topological constraints on semiflexible polymers by Romanowska *et al.* [39] who imaged confinement tubes for individual polymers of an F-actin solution.

Dua and Vilgis [40] considered a bending term in their analytic investigations of a polymer in a landscape of uncorrelated point disorder. They predicted analytically the occurrence of localization and delocalization of a semiflexible polymer in dependence on the ratio of the mean separation of the obstacles and the persistence length. For a mean separation of the obstacles that is larger than the persistence length, the polymers are localized. As soon as the persistence length exceeds the mean separation between the obstacles, the polymer gets delocalized.

The above explained cases described mostly situations, where a potential or topological constraints in the form of obstacles modified the conformations and properties of the polymers. Another way of involving confinement was chosen in [41, 42, 43, 44, 45], namely inducing it by the geometry of the boundaries. Cifra [45], for example, analyzed the properties of a semiflexible polymer with excluded volume interaction confined to a channel or slit. As long as the persistence length is smaller than the channel width d_c, the polymer forms a coil whose properties can be described by the blob model, invented by de Gennes [46] and extended to persistent chains by Schaeffer, Joanni, and Pincus [47]. In this model, the semiflexible polymer can be understood as ideal chain on a certain length scale, the so-called blob scale. For the case of Cifra, this scale is prespecified by the width of the channel. The arising structure is that of a sequence of blobs along the channel for $\ell_p < d_c$. As soon as the persistence length becomes larger than the width of the confining channel, the blob model can no longer be applied. The polymer does no longer form a coil but starts to stretch due to the confinement.

Some other attempts to model the disorder as part of the chain, e.g., as random fixed angles between a number of bonds of the chain, were done in [48, 49, 50].

In this work, I investigate the impact of disorder in the form of immovable hard disks on the equilibrium properties of semiflexible polymers by means of Monte Carlo simulations. I consider two different, archetypical classes of disorder: (i) lattice disorder and (ii) fluid disorder. The former is generated by putting the disks onto the sites of a square lattice with a certain occupation probability p. For the case of flexible polymers my work is published in [51]. The disorder on the lattice exhibits both aspects described above. On the one hand it blocks certain areas. That way the polymer is forced to bypass them. On the other hand, for a certain choice of parameters, it builds up channels and cavities thus having the effect of a limiting boundary as in the case described by Cifra. The other way of arranging the disorder, (ii), is modelling it as hard-disk fluid. It is analyzed how the fluid correlations of the disorder alter

the properties of the polymer and how they are reflected in the according distribution functions. Beyond the scope of polymers and biophysics, the problem at hand poses an interesting mathematical and especially algorithmic challenge. The stiffness and length constraints along with the spatial confinement lead to both high energy barriers and extreme fragmentation of configuration space. These conditions ask for highly sophisticated methods that sample space subtly and efficiently in order to provide high accuracy data for the estimation of distributions.

1.3. Algorithmic challenge

Computer simulations couple analytical theory and experiment. A strong point of computer simulations is the reproducibility and the ability to both control important parameters of the system and prevent unwanted side effects. For these reasons, computer simulations have become an indispensable tool for investigating the systems described in the above sections. Both lattice and off-lattice models have been studied by computer simulations of polymers in disorder [52, 53, 54, 55, 56]. Baumgärtner and Muthukumar [33] investigated a Gaussian chain polymer without self-avoidance by computer simulations. A cubic lattice is randomly occupied by impenetrable boxes up to a specified volume fraction. From Monte Carlo simulations they found similar results as Cates and Ball. The repulsion of the boxes acts on the polymer as effective attractive potential between the monomers which finally leads [57] to shriveling and collapse of the polymer for increasing number of obstacles. In the case of Baumgärtner and Muthukumar, the obstacle density is in a regime where standard methods such as the Metropolis algorithm (see next paragraph) still can be applied. This is even more favored by the fact that only flexible polymers are simulated.

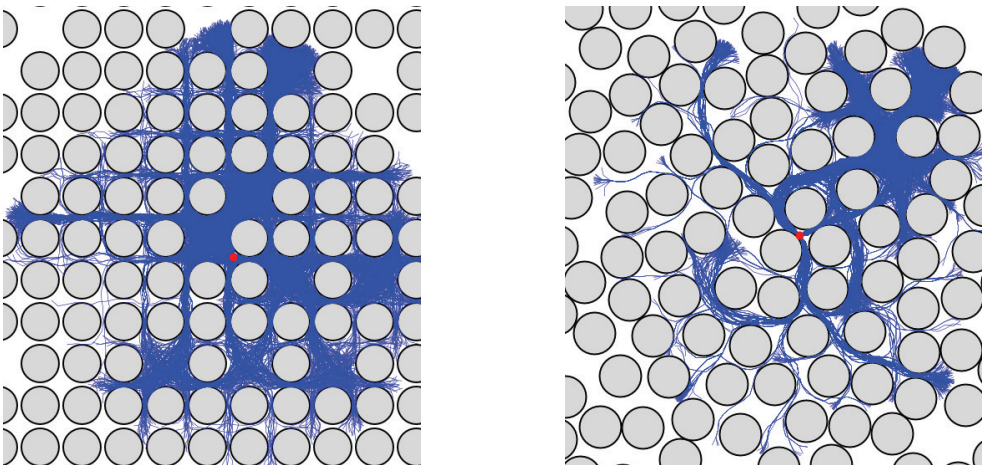

Figure 1.1.: Exemplary polymer ensembles in lattice (left) and fluid disorder (right) at volume fraction $\rho = 0.6$.

Figure 1.1 is an illustration of the questions addressed in this work. The figure shows a typical disorder configuration consisting of hard disks. Additionally, four polymer configurations that share a common starting point are depicted. The challenging task is to find the equilibrium distribution of polymers in the presence of a potential consisting of hard disks that reduces configuration space by fragmenting it. Additionally, there is the length scale constraint induced by the persistence of the polymer. Although the problem can easily be grasped from Fig. 1.1, it is quite hard to solve it by means of computer simulations. Consequently, one has to find algorithms that sample space in such a way that the exact solution is approximated accurately enough. This is indeed not a trivial task. Especially in a high-density disorder landscape, the existence of many local solutions hampers correct sampling and thus makes it difficult to find (approximate) a global solution. As soon as the area fraction of the disorder exceeds a certain value, the application of, e.g., a standard Markov chain Monte Carlo (MCMC) method based upon the Metropolis algorithm [58] does not work well anymore. The basic principle of this algorithm is building up an initial polymer chain and then updating it in order to sample the configuration space. These methods result in a rejection rate that makes it impossible to create enough configurations to compute observables, yielding a diverging *autocorrelation time*, the time scale over which observations of the system look similar. One way of treating this problem for the case of rugged energy landscapes is the application of techniques based upon the replica exchange method [59, 60]. Another alternative was proposed by Berg and Neuhaus [61, 62] as well as by Janke [63], the multicanonical Monte Carlo method. Here it is used as a benchmark and as comparison to the method applied throughout this work [51].
The method I use is a growth algorithm which is explained in detail in Sec. 3. The main idea is to generate equilibrium ensembles of grafted polymers by successively

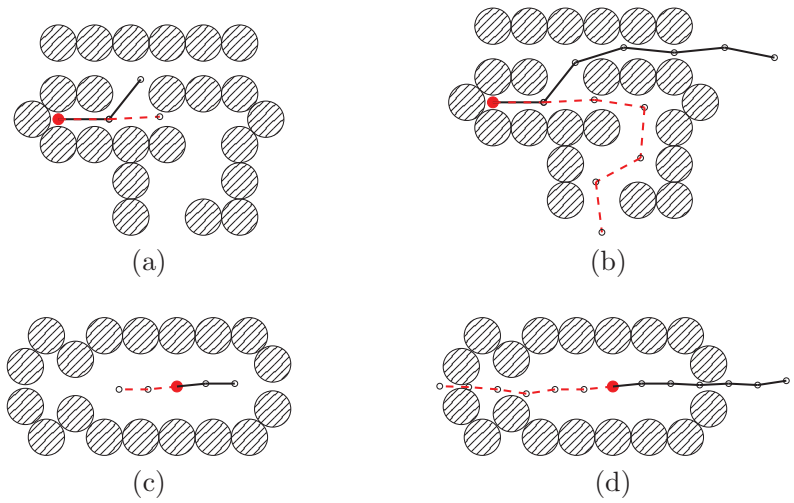

Figure 1.2.: On the perils of premature optimization.

polymerizing a number of shorter chains in all available directions at once. It is very promising for the problem at hand as it gradually samples configuration space in a very high resolution, thus being able to find paths out of local trappings which prevents the algorithm from getting stuck in metastable states. The basic routine—if used without guiding field, population control parameter, etc. (Sec. 3)—is, however, an algorithm of the 'greedy'-type. This issue is sketched in Fig. 1.2 in a very simplified way. Consider the question of setting up a 6-segment semiflexible polymer chain in a confining geometry by growing it segment per segment sequentially. Local optimization would favor the dashed (red) line in both cases of Figs. 1.2(a) and (c), once for energetic reasons (smaller bending angle), in the other case for entropic reasons (larger passage is entropically more favorable). In both cases [Figs. 1.2(b) and (d)], the solid (black) configuration is globally more favorable. This problem can be overcome by biasing the distributions. This has of course to be cured again afterwards in order to keep the statistics correct. The strong point of this method is that it samples configuration space with a dense and subtle network of configurations. In this way the strongly fragmented space can be investigated with a high resolution. The enormous advantage thereof will fall into place by looking at the numerical results of this work in Sec. 4. The details of the algorithm and how the greedy problem is tackled are explained in Sec. 3.

The rest of this thesis is organized as follows. In Chapter 2, the models used throughout this work are discussed. The numerical algorithms and methods are described in Chapter 3. Chapter 4 contains the numerical results. In Chapter 5, I finally summarize and conclude.

2. Polymer model and disorder

2.1. Polymer model

Semiflexible polymers, such as actin, can—strongly coarse-grained—be thought of as chains of monomers connected by torsion springs whose resistance to bending renders the polymer inflexible on short length scales. Therefore the springs can be thought of bonds that have a fixed length. The polymers are made semiflexible by adding an energy penalty for bending neighboring bonds. An appropriate physical model for those polymers is the Heisenberg chain.

2.1.1. Heisenberg chain model

The Heisenberg chain is a bead-stick model consisting of $N+1$ beads at positions $\mathbf{r}_i$ connected by bonds of fixed length b. Therefore, the contour has a length of $L = Nb$. My considerations are made for the case of two dimensions and a phantom chain where self-avoiding constraints are neglected. Additionally, the polymers are all pinned at the same pinpoint. The consequences that evolve if the pinning—which plays a role as soon as a disorder background is involved—is given up are briefly discussed in Sec. 4.6. The connecting line between two monomers defines a unit tangent vector $\mathbf{t}_i = (\mathbf{r}_{i+1} - \mathbf{r}_i)/b$ (Fig. 2.1). The elastic properties are governed by the bending energy

$$\mathcal{H} = -J \sum_{i=1}^{N-1} \mathbf{t}_i \mathbf{t}_{i+1}, \tag{2.1}$$

where $\mathbf{t}_i \mathbf{t}_{i+1} = \cos(\theta_{i,i+1})$ determines the angle between neighboring bonds and $J > 0$ is a coupling constant. The limiting case of zero coupling between neighboring bonds results in the freely jointed chain which is a common model for flexible polymers. The correlations between the two-dimensional tangent vectors of the free Heisenberg chain decay at inverse temperature $\beta = 1/k_\mathrm{B}T$ as [64]

$$\langle \mathbf{t}_i \cdot \mathbf{t}_{i+k} \rangle = \left[\frac{I_1(\beta J)}{I_0(\beta J)} \right]^k, \tag{2.2}$$

where $I_\mu(x)$ is the modified Bessel function of the first kind of order μ.

2.1.2. Continuum limit of the Heisenberg chain

To carry out the continuum limit of the Heisenberg chain, we take the Hamiltonian Eq. (2.1) and let $N, J \to \infty$ while $b \to 0$ with $Jb = \text{const.}$ and $Nb = L$ (constant length constraint).

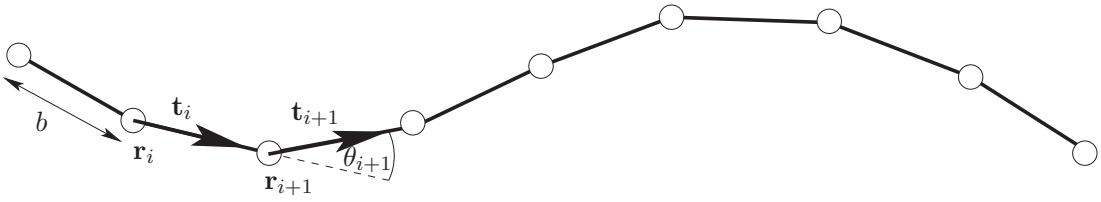

Figure 2.1.: Sketch of the Heisenberg chain model.

For performing the limit, the following identity is used:

$$-\mathbf{t}_{i+1} \cdot \mathbf{t}_i = \frac{1}{2}[(\mathbf{t}_i - \mathbf{t}_{i+1})^2 - 2]. \tag{2.3}$$

Inserting this into Eq. (2.1) leads to

$$\mathcal{H} = \frac{Jb}{2} \sum_{i=1}^{N-1} b \left(\frac{\mathbf{t}_{i+1} - \mathbf{t}_i}{b} \right)^2 - \sum_{i=1}^{N-1} J. \tag{2.4}$$

Using the fact that the term in brackets of Eq. (2.4) is the discrete derivative of the tangent vector $\mathbf{t}$, passing into

$$\lim_{b \to 0} \left(\frac{\mathbf{t}_{i+1} - \mathbf{t}_i}{b} \right) = \frac{\partial \mathbf{t}(s)}{\partial s}, \tag{2.5}$$

in the limit of $b \to 0$, and changing furthermore the sum to an integral

$$\sum_{i=1}^{N-1} b \to \int_0^L ds \tag{2.6}$$

we obtain the Hamiltonian (except for a constant)

$$\mathcal{H} = \frac{\kappa}{2} \int_0^L ds \left(\frac{\partial \mathbf{t}(s)}{\partial s} \right)^2 = \frac{\kappa}{2} \int_0^L ds \left(\frac{\partial^2 \mathbf{R}(s)}{\partial s^2} \right)^2 \tag{2.7}$$

with $\kappa = Jb$ being the bending stiffness and $\mathbf{R}(s)$ describing the contour parametrized by arc length s.

2.1.3. Wormlike chain model

The above Hamiltonian [Eq. (2.7)] is the Hamiltonian of the wormlike chain. The wormlike chain (WLC) is one of the most famous and widely spread models for describing semiflexible polymers. It provides an appropriate description for long slender polymers, completely masking the microscopic details on the monomer scale. It is a continuum model described by a space curve $\mathbf{R}(s)$ with constant contour length L.

Hence this model only considers the influence of the bending energy, whereas backbone stretching deformations are suppressed. Backbone stretching becomes relevant for forces that exceed the physiological scope of biopolymers, which are described by the above models. The constraint of constant contour length is kept by requiring $(\partial_s \mathbf{R})^2(s) = \mathbf{t}^2(s) = 1$. A central property of the wormlike chain is its *persistence length* ℓ_p, which is the tangent vector correlation length [14],

$$\langle \mathbf{t}(s)\mathbf{t}(0)\rangle = e^{-s/\ell_p}. \tag{2.8}$$

In analogy to the continuum limit of the Heisenberg chain Hamiltonian, we consider the following approximation[2]. For large βJ or small b, and therefore large N, the modified Bessel function in Eq. (2.2) yields [65]:

$$I_\mu(x) \approx \frac{e^x}{\sqrt{2\pi x}} \left\{ 1 - \frac{4\mu^2 - 1}{8x} + \frac{(4\mu^2 - 1)(4\mu^2 - 9)}{2!8x^2} - \mathcal{O}(x^{-3}) \right\}. \tag{2.9}$$

Thus, for large $\beta J \propto N$ and $l = kb$ one finds for the tangent correlations by inserting Eq. (2.9) into Eq. (2.2) to leading order:

$$\langle \mathbf{t}_i \cdot \mathbf{t}_{i+k} \rangle = \exp\left(-\frac{k_B T}{2Jb} l \right). \tag{2.10}$$

A comparison of Eq. (2.10) with Eq. (2.8) and identifying l with s results in

$$\ell_p = 2\frac{Jb}{k_B T} = 2\frac{\kappa}{k_B T}. \tag{2.11}$$

The persistence length is thus the ratio between bending stiffness κ and thermal energy $k_B T$ and is therefore a measure of the stiffness of a polymer. I call the persistence length measured in units of total polymer length $\xi = \ell_p / L$. In general dimension d it holds [66]:

$$\ell_p = \frac{2}{d-1} \frac{\kappa}{k_B T}. \tag{2.12}$$

There are three regimes defining three classes of polymers:

$$\begin{cases} b \approx \ell_p \ll L & \text{flexible} \\ b \ll \ell_p < L & \text{semiflexible} \\ b \ll L \ll \ell_p & \text{stiff.} \end{cases} \tag{2.13}$$

Controlled analytical calculations are usually limited to the extreme cases of flexible or stiff polymers.

At last I want to remark on the mean square end-to-end distance $\langle R_{\mathrm{ee}}^2 \rangle$. Using the definition $\langle R_{\mathrm{ee}}^2 \rangle = \langle (b \sum_{i=1}^N \mathbf{t}_i)^2 \rangle$ together with Eq. (2.2), its calculation is straightforward and amounts in the continuum limit to (cp. e.g. [14]):

$$\langle R_{\mathrm{ee}}^2 \rangle = 2\ell_p L \left\{ 1 - \frac{\ell_p}{L} [1 - \exp(-L/\ell_p)] \right\}. \tag{2.14}$$

[2] A further approach for calculating the tangent-tangent correlations can be found in, e.g., [14].

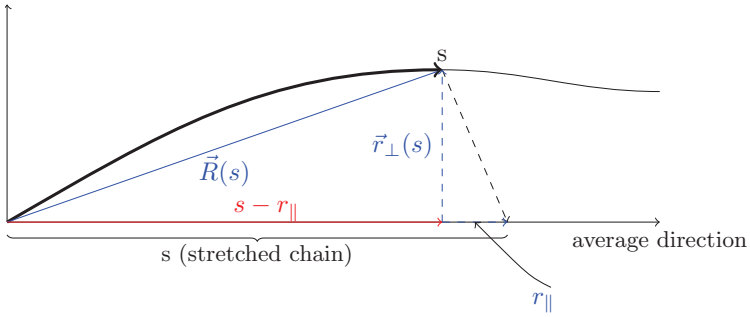

Figure 2.2.: Arc length parametrization of the WLC.

2.1.4. Weakly bending rod and end-to-end distribution function

In order to characterize a polymer, one may calculate the tangent-tangent correlations or the *end-to-end distribution function* $P(\mathbf{R})$, i.e. the probability distribution for the distance vector $\mathbf{R}$ of the two filament ends. For the purpose here it is averaged over all directions to obtain $P(R)$ which is also called radial distribution function.

In this work it is primarily used for analyzing the results of Monte Carlo simulations. For the case of free, stiff polymers, the end-to-end distribution function can be evaluated analytically in the *weakly bending rod* (WBR) limit.

As addressed in 2.1.2, the wormlike chain can be described as a continuous space curve. It is parametrized by its arc length s by specifying deviations from a straight line (cp. Fig. 2.2):

$$\mathbf{R}(s) = (\mathbf{r}_\perp(s), s - r_\parallel(s))). \tag{2.15}$$

The arc length constraint is given by

$$(\mathbf{R}'(s))^2 = (\mathbf{t}(s))^2 = \mathbf{r}_\perp'^2 + (1 - r_\parallel')^2 = 1. \tag{2.16}$$

For very stiff polymers ($\ell_p \to \infty$), $\mathbf{r}_\perp'^2 = O(\epsilon) \ll 1$, this parametrization becomes very useful. The stiffness refers to the ratio between L and ℓ_p

$$\epsilon := \frac{L}{\ell_p} \ll 1. \tag{2.17}$$

Using the arc length constraint, Eq. (2.16), yields

$$r_\parallel' = 1 - \sqrt{1 - \mathbf{r}_\perp'^2} = \frac{1}{2}\mathbf{r}_\perp'^2 + O(\epsilon^2) = O(\epsilon). \tag{2.18}$$

Thus in the WBR approximation, the WLC can to order $O(\epsilon^{1/2})$ be written as $\mathbf{R}(s) = (\mathbf{r}_\perp(s), s)$.

Based upon the WBR approximation, Wilhelm and Frey [15] derived an analytical expression for the end-to-end distribution function in two and three dimensions. The

two dimensional form reads:

$$P(r) = \frac{1}{2\pi\mathcal{N}} \frac{2\kappa}{\sqrt{\pi}} \sum_{l=0}^{\infty} \frac{(2l-1)!!}{2^l l!} \frac{1}{[2\kappa(1-r)]^{5/4}} \times \exp\left[-\frac{(l+1/4)^2}{2\kappa(1-r)}\right] D_{3/2}\left[2\frac{l+1/4}{\sqrt{2\kappa(1-r)}}\right] \tag{2.19}$$

where $D_{3/2}(x)$ is a parabolic cylinder function. $P(r)$ converges very quickly such that terms of higher order than three showed no more improvement. Another approach was performed by Hamprecht, Janke, and Kleinert [67, 68] who used a recursion relation for the even moments of the end-to-end distribution function.

2.2. Disorder

The background potential consists of hard disks with diameter σ that interact with the monomers of the polymer via hard-core repulsion described by the potential

$$V_\sigma(r) = \begin{cases} \infty & \text{for} \quad d < \sigma/2, \\ 0 & \text{else}, \end{cases} \tag{2.20}$$

where d is the distance between a monomer and a hard-disk center. Thus, the monomers—here described by points—may not be placed onto the area of a disk.

Throughout this work, two ways of arranging the disks are used. For one thing I put the disks onto the sites of a square lattice, for another thing they are arranged as monodisperse hard-disk fluid configurations. The periodic square lattice structure of the first assembly leads to long straight channels as can be seen in Fig. 2.3(a). This is different for the fluid arrangement [Fig. 2.3(b)]. Furthermore, the lack of correlations of the disks (or existence of merely trivial correlations; see next paragraph) for the case of the lattice structure leads to strong spatial inhomogeneities of the potential and clustering plays a dominant role. This seems to be different for the fluid arrangement, where the interaction of the disks "homogenizes" the potential for the parameter range of the scope here. This entails strong consequences for the properties of the potential and hence of the impact on the polymers which are in detail discussed in Sec. 4.

2.2.1. Lattice disorder

The lattice arrangement was chosen in order to be able to control the distance between neighboring disks by adjusting the lattice constant a and the disk diameter σ appropriately. I thus was able to investigate the applied methods in a "controlled" disorder environment. More details on the methods and the exact parameters used to generate the disorder configurations will be given in Sec. 3.2 and Sec. 4.2, respectively. Each site of the square lattice is occupied independently with a certain occupation probability p.

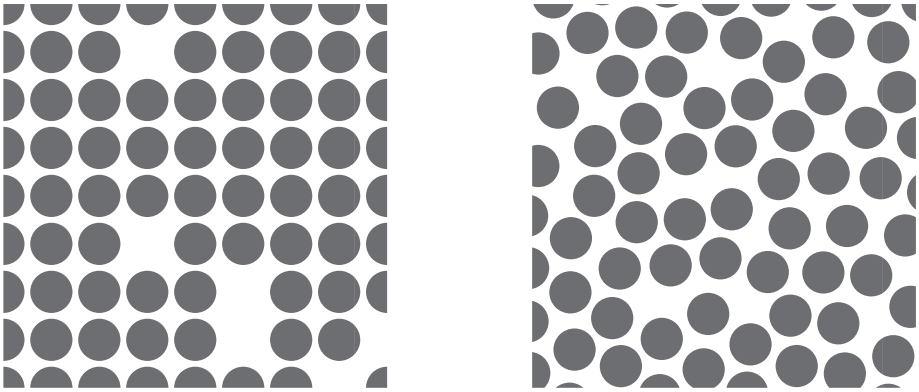

(a) (b)

Figure 2.3.: Different kinds of disorder considered in this work: (a) lattice disorder; (b) fluid disorder.

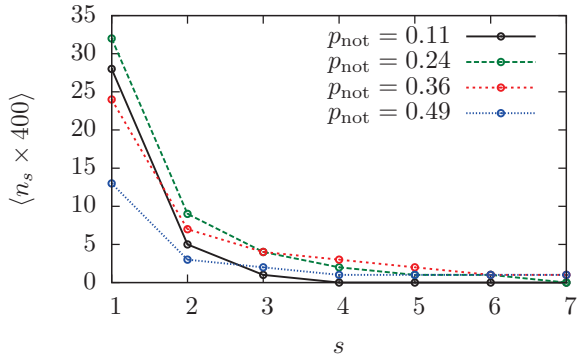

Figure 2.4.: Plot of the mean number of clusters in dependence on the cluster size. The connecting lines are for better visibility. The average number of clusters of a certain size per disk n_s is multiplied by 400 in order to get the average number per lattice. The lattice consists of 400 sites.

Consequently, there are no correlations between neighboring disks besides the constraint that the minimum distance between two disks is a, the lattice constant. This again leads to clustering which plays a crucial role for the lattice arrangement. In order to get some insight into the structure of the disorder, one can calculate the average number of clusters of a certain size at a given occupation probability p [69]. The estimates of the cluster-size distribution are valid in the low-density regime $p < p_c$, where $p_c = 0.59$ is the percolation threshold. As we are interested in the space that is available for a polymer in disorder, we have to consider the probability of empty

Table 2.1.: Average number of clusters depending on the cluster size s. The data are rounded to integer values and correspond to the data of Fig. 2.4.

s	p_{not}			
	0.11	0.24	0.36	0.49
1	28	32	24	13
2	5	9	7	3
3	1	4	4	2
4	0	2	3	1
5	0	1	2	1
6	0	1	1	1
7	0	0	1	1

clusters. Therefore, we take the probability to find an empty site which is $p_{\mathrm{not}} = 1-p$. Consequently we are looking at $p_{\mathrm{not}} < p_{c_{\mathrm{not}}}$, where $p_{c_{\mathrm{not}}}$ is the empty-site percolation threshold. For the calculation of the cluster-size distribution one uses so-called perimeter polynomials. For the square lattice they are given in Sykes and Glen [70] for clusters up to size 17. The average number of clusters of size s per lattice site is given by:

$$n_s = \sum_t g_{st} p_{\mathrm{not}}^s (1 - p_{\mathrm{not}})^t = p_{\mathrm{not}}^s \times D_s(p), \tag{2.21}$$

where t is the perimeter, g_{st} the number of lattice animals, i.e. cluster realizations with size s and perimeter t, and D_s the perimeter polynomial belonging to cluster size s. If we are interested in empty site clusters, the perimeter t denotes the occupied sites surrounding a cluster. The perimeter also includes holes in clusters. In order to get the average number of clusters at a certain size s and empty-site occupation p_{not} per lattice, we multiply n_s by the number of lattice sites (400 in this work). Figure 2.4 shows the average number of clusters in dependence on the cluster size. Table 2.1 shows the corresponding values. The data of Fig. 2.4 and Table 2.1 have to be understood as rough estimates because the lattices considered here are rather small. Another important information besides the cluster size is to know where nearby empty space is. As there are no long-range correlations (see above), the probability to find two empty sites n sites apart is constant for all n. Thus the only information of nearby void space besides the cluster size distribution is the lattice constant a and the disk diameter σ. Obviously, four disks arranged on a quad confine void space (see Fig. 4.6). Depending on the ratio of disk diameter σ and lattice constant a, the void space is connected to the rest of the lattice by channels of different sizes [Figs. 4.6(a) and (b)] or is even inaccessible [Fig. 4.6(c)]. The last case (inaccessible) is somewhat pathologic and only considered for the case of disorder on the lattice.

2.2.2. Fluid disorder

A monodisperse hard-disk fluid is defined as a system of disks with diameter σ at area fraction ρ that interact via hard-core repulsion, i.e., the interaction potential $u(r)$ is given by

$$u(r) = \begin{cases} \infty & \text{for} \quad r \leq \sigma, \\ 0 & \text{for} \quad r > \sigma, \end{cases} \tag{2.22}$$

where r is the distance between the centers of two disks. Although rather simplistic, the hard-disk fluid has successfully served as model system for real fluids, colloidal systems, etc. Hard-sphere[3] systems also played a crucial role in the development of stochastic numerical methods such as the Markov Chain Monte Carlo algorithm. It was first applied to such a system by Metropolis *et al.* [58]. Especially structural effects such as percolation and jamming as well as the liquid-solid phase transition [71] can be studied well. The liquid-solid transition of hard spheres was examined by Alder and Wainwright [72] already in 1957 by computer simulations. Modern investigations locate the melting point for hard-disk fluids slightly above $\rho = 0.7$ [73]. For polydisperse systems even a glass transition and glass behavior can be observed [74]. In the hard-disk model, all realizations have the same potential energy and so there is no energetic reason to prefer any allowed realization over another. The driving forces in a hard-sphere system are of entropic nature. These entropic effects show a rich phenomenology and are still incompletely understood, especially in two dimensions.

Structure of hard-disk fluids [75, 76, 77]

The hard-disk fluid has two length scales, the average distance between the centers of the disks r and the disk diameter σ. The first can be expressed in terms of the number density of a homogeneous system $\hat{\rho} = N/A$, with N being the number of disks[4] and A the area enclosing the disks. The area fraction

$$\rho = \hat{\rho}\pi\sigma^2/4 \tag{2.23}$$

combines these two length scales. The common procedure to explore an equilibrium physical system in statistical mechanics is to calculate the partition sum which comprises all the information of the specific system. Once having obtained the partition sum, one can compute the related thermodynamic mean values. As the partition sum contains the complete information of the entire observed system, one can imagine that it is very difficult to compute and handle the partition sum for big and highly interacting systems. Moreover, for many issues it is not necessary to know all the details of the system. Especially in liquid state theory the concept of reduced distribution

[3] Throughout this work, only two dimensional systems are considered. In the text, 'hard-disk' and 'hard-sphere' are used interchangeably, because they show a similar phenomenology in the considered scope.

[4] In the section about disorder, N refers to the number of disks of the background potential. In the rest of the work, it denotes the number of bonds of the polymers.

functions has proven to be very useful. To analyse the structure of a system consisting of N identical spherical particles in a volume V at temperature T, the function

$$P_N(\mathbf{r}^N) = \frac{e^{-\beta \mathrm{U}(\mathbf{r}^N)}}{Z_N(V,T)} \tag{2.24}$$

with configuration integral

$$Z_N(V,T) = \int d\mathbf{r}_1 \cdots d\mathbf{r}_N e^{-\beta \mathrm{U}(\mathbf{r}^N)} \tag{2.25}$$

is the probability density that the N particles are at the positions $\mathbf{r}_1, \cdots, \mathbf{r}_N$, with $U(\mathbf{r}^N)$ being the potential energy of a N-particle liquid. It is commonly assumed that the potential energy $U(\mathbf{r}^N)$ of such a liquid can be approximated as a sum of pair interactions

$$U(\mathbf{r}^N) \approx \sum_{i<j}^{N} u(|\mathbf{r}_i - \mathbf{r}_j|) = \sum_{i<j}^{N} u(r_{ij}) \tag{2.26}$$

for any configuration $\mathbf{r}^N = \{\mathbf{r}_1, \cdots, \mathbf{r}_N\}$. In Eq. (2.26) $u(r_{ij})$ denotes the interaction energy between two particles. For the structural information in the case of, e.g., liquids, one merely needs the reduced distribution functions of a small subset of $n << N$ particles irrespective of the remaining $N - n$ particles. To do so one introduces the n-particle distribution function

$$\rho_N^{(n)}(\mathbf{r}^n) = N(N-1)\cdots(N-n+1) \int d\mathbf{r}_{n+1} \cdots d\mathbf{r}_N P_N(\mathbf{r}^N) \tag{2.27}$$

to find a configuration of n identical particles with $\mathbf{r}^n = \{\mathbf{r}_1, \cdots, \mathbf{r}_n\}$. Of major interest for examining fluids are the reduced distribution functions of order $n = 2$. For a homogeneous system $\rho_N^{(1)} = \rho = N/V$ is the average particle number density. In the case of $n = 2$, $\rho_N^{(2)}(\mathbf{r}_1, \mathbf{r}_2) = \rho_N^{(2)}(\mathbf{r}_1 - \mathbf{r}_2)$ which follows from translational invariance. The central observable of fluids, gases, and solids that provides information about their structure is the pair distribution function

$$\mathrm{g}_N(\mathbf{r}_1, \mathbf{r}_2) := \frac{\rho_N^{(2)}(\mathbf{r}_1, \mathbf{r}_2)}{\rho_N^{(1)}(\mathbf{r}_1)\rho_N^{(1)}(\mathbf{r}_2)}. \tag{2.28}$$

It is defined in such a way that $\mathrm{g}_N(\mathbf{r}_1, \mathbf{r}_2) \to 1$ for $r_{12} \to \infty$. The pair distribution function measures to which extent the structure of a fluid deviates from the structure of an ideal gas. If the system is isotropic as well as homogeneous, the pair distribution function $\mathrm{g}_N^{(2)}(\mathbf{r}_1, \mathbf{r}_2)$ is a function only of the separation $r_{12} = |\mathbf{r}_2 - \mathbf{r}_1|$. It is then called *radial distribution function* (RDF). To be independent of the specific statistical ensemble used during the calculation of static properties, one takes the thermodynamic limit with $\rho = N/V$ kept fixed at the end of each calculation:

$$g(r) = \lim_{N,V\to\infty} g_N(r). \tag{2.29}$$

The practical meaning, especially for monoatomic fluids, can be seen in two respects. First, the radial distribution function is directly measurable by scattering experiments. This can easily be seen by considering the connection between $g(r)$ and the static structure factor $S(q)$, Eq. (2.30), which is the central quantity to be measured in scattering experiments

$$g(r) = \mathcal{F}^{-1}\left[\frac{S(q)-1}{\rho}\right]. \tag{2.30}$$

So $g(r)$ and $S(q)$ are connected via a Fourier transformation.

Secondly, provided that the atoms interact through pairwise additive forces [compare Eq. (2.26)], thermodynamic properties of a fluid can be written as integrals over $g(r)$ and $u(r)$, where $u(r)$ denotes again the pair interaction potential of two particles. The internal energy consists of two parts. A kinetic term which can be easily calculated by

$$\langle T_{\text{kin}}\rangle = \frac{3}{2}Nk_BT \tag{2.31}$$

in three dimensions. For the potential part, which we could better call interaction part, we use the following integral

$$\langle U(\mathbf{r}^N)\rangle = \frac{1}{2}\rho N \int_0^\infty dr 4\pi r^2 g(r)u(r). \tag{2.32}$$

Our system is homogeneous as well as isotropic so we calculate the interaction from the perspective of one particle multiplying by N. This has to be divided by two to compensate double counting of interactions. $4\pi r^2 g(r)dr$ is the property of finding a particle in a spherical shell of distance r and thickness dr. Multiplying this by ρ, which is constant in our system, gives the number of particles in this shell. Hence Eq. (2.32) is the potential part of E. So E can be calculated by

$$E = \langle T_{\text{kin}}\rangle + \langle U(\mathbf{r}^N) = \frac{3}{2}Nk_BT + \frac{1}{2}\rho N \int_0^\infty dr 4\pi r^2 g(r)u(r). \tag{2.33}$$

At the end of this section I want to mention two general properties of $g(r)$ for the case of fluids (no long-range correlations):

$$g(r) \geq 0,\ g(r\to\infty) = 1 \tag{2.34}$$

$$g(r) \approx 0,\ \text{for } \beta u(r) \gg 1. \tag{2.35}$$

The first property states that the correlations between spheres decay for increasing distance. For the second property imagine a hard-sphere system. If two spheres overlap we have $u(r) = \infty$. Therefore the probability of finding another particle a distance less than one diameter apart is zero.

In summary it can be said that the RDF $g(r)$ gives the average structure of a hard-disk fluid. It gives the relative probability to find a disk a distance r apart provided that there is a disk at the origin O ($r = 0$).

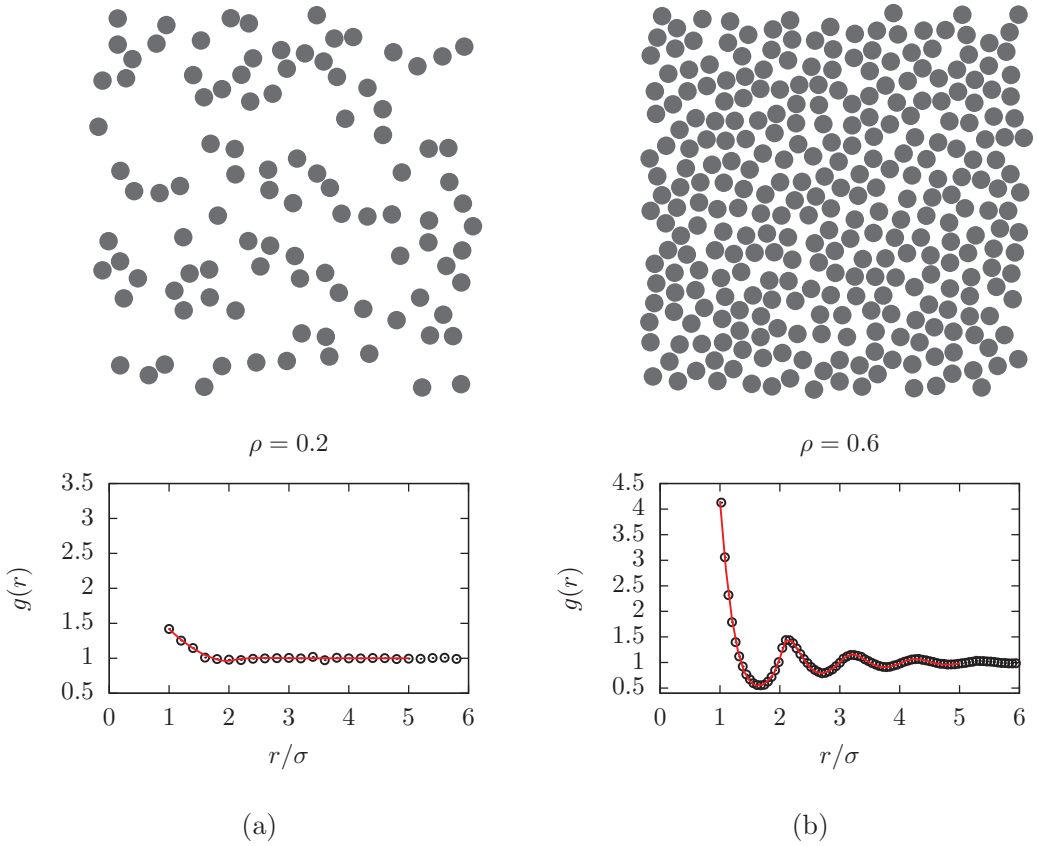

Figure 2.5.: Top: exemplary hard-disk fluid configurations at (a) $\rho = 0.2$ and (b) $\rho = 0.6$. Bottom: corresponding radial distribution functions. $\odot$ are data from my simulations, the solid (red) line is the numerical evaluation of the analytical solution of the Percus-Yevick approximation [78].

Figure 2.5 shows two hard-disk fluid configurations and their corresponding RDFs. Figure 2.5(a) is at $\rho = 0.2$ and Fig. 2.5(b) at $\rho = 0.6$. The range of the correlations of the fluid can nicely be seen in Fig. 2.5.

Void-space correlations

An important aspect of the fluid structure are the spatial correlations which allow for 'predictions' of free space a certain distance r apart from the current position. From this, one can infer that the distribution functions that directly reflect the spatial structure of the polymer, somehow comprise the structure of the spatial correlations of the fluid.

As the polymer is located in the space between the disks, we are interested in the correlations of the void space. I call the corresponding function "void-space distribu-

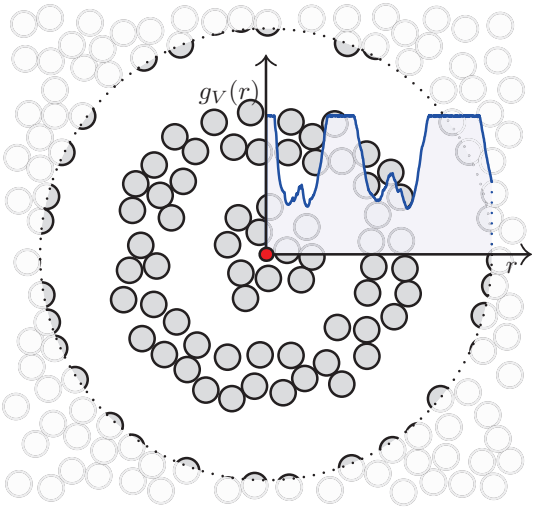

Figure 2.6.: Probability $g_V(r/L)$ to find a void-space at distance r/L from the center.

tion function" (VSDF) $g_V(r)$. In analogy to the RDF, it gives the probability to find two spots of void space a distance r apart (cp. Fig. 2.6). The VSDF $g_V(r)$ is effectively a transformation of the first minimum of $g(r)$ into a first maximum of $g_V(r)$. The RDF $g(r)$ and $g_V(r)$ for $\rho = 0.4, 0.5, 0.6, 0.7$ are shown in Fig. 2.7. More details on the statistics of void space can be found in [79, 80].

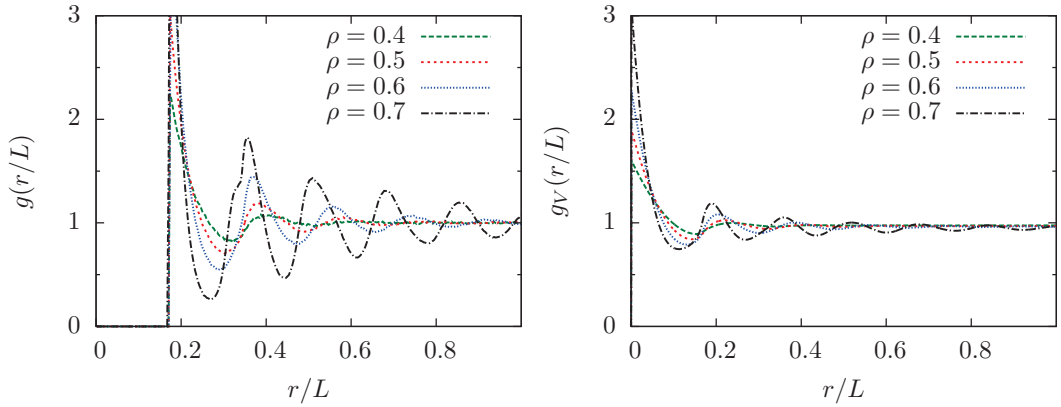

Figure 2.7.: Radial distribution function (a) and void-space distribution function $g_V(r)$ (b) (explanation given in the text). The occupation probabilities are: $p = 0.4$ (– –, green), 0.5 (– – –, red), 0.6 (……, blue), and 0.7 (– · –, black).

2.3. Average mean free distance between disks of the potential

For estimating the density regimes of the fluid with respect to the polymer extension, I compare the length scales of polymer and disorder. In order to do so, I use two approaches for estimating the average length between two disks of the background potential. For one thing I calculate the average distance between the centers of the disks $\widehat{r}_1$. That is the particles are assumed to be pointlike and their average distance is calculated from the number density $\widehat{\rho}$:

$$\widehat{r}_1 = \sqrt{A/N} = \sqrt{1/\widehat{\rho}}. \tag{2.36}$$

The diameter σ is now subtracted and one finds:

$$r_1 = \widehat{r}_1 - \sigma = \sqrt{1/\widehat{\rho}} - \sigma = \sqrt{\sigma^2\pi/(4\rho)} - \sigma. \tag{2.37}$$

Secondly, the average free area per disk is calculated. It is the mean area per disk (A/N) minus the area of one disk $(\sigma^2\pi/4)$,

$$A_{\text{free}} = (A - N\sigma^2\pi/4)/N = \pi\frac{\sigma^2}{4}(\rho^{-1} - 1). \tag{2.38}$$

The average distance between two disks r_2 gives then

$$r_2 = \sqrt{A_{\text{free}}} = \sqrt{\pi}\frac{\sigma}{2}\sqrt{\rho^{-1} - 1}. \tag{2.39}$$

The difference between r_1 and r_2 becomes clear by considering Figs. 2.8(a) and (c). While r_1 is zero for a special choice of disk diameter σ and area fraction ρ [Fig. 2.8(c)],

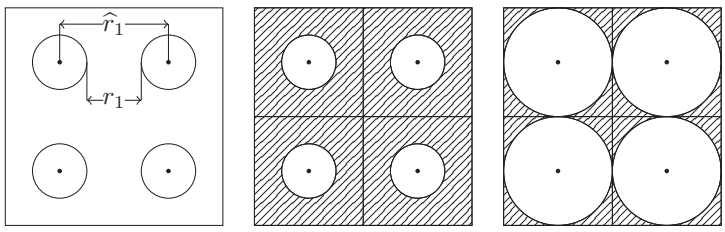

Figure 2.8.: (a) illustrates the meaning of $\widehat{r}_1$ and r_1, respectively. The shaded areas in (b) and (c) are the free areas per disk A_{free}. The meaning of A_{free} becomes clear if we look at (c). In this case, r_1 is zero but r_2 is not. While r_1 is the average distance between disks, r_2 is a measure of the free length that is left between neighboring disks even if they touch each other (in this case r_2 is a measure of the extension of a small cavity that is enclosed by disks).

r_2 is still finite. If we think of objects that reside between the disks, r_2 is a measure of the area accessible to objects even for high densities whereas r_1 characterizes a regime where the distance between neighboring disks constitute an upper limiting boundary. r_1 and r_2 are estimated by mean-field assumptions and thus must not be overrated for finding subtle difference between density regimes. The consequences of these length scales for the polymer will be discussed in Chapter 4.

3. Methods

This chapter is concerned with the methods I use for treating polymers in a disorder potential of hard disks and how those disorder potentials are set up. After a brief introduction to Monte Carlo simulations in Sec. 3.1, I describe how the disorder configurations are generated (Sec. 3.2). In Sec. 3.3, I go into the numerical treatment of polymers in disorder. Averaging and error estimation are explained in Sec. 3.4.

3.1. Monte Carlo simulations

In 1777, Georges-Louis Leclerc, Comte de Buffon, went into the question of the probability that a randomly dropped needle of length l crosses a line on the floor marked with stripes of equal distance $d \geq l$. This famous experiment is known as "Buffon's needle problem" [81] and can be thought of as an early example of Monte Carlo sampling. An application of Buffon's needle was the calculation of π. Generally spoken, Monte Carlo methods are stochastic techniques to investigate problems based on the use of random numbers and probability statistics. They are used to calculate numerical solutions of, e.g., integrals, by drawing random positions (samples) from carefully chosen distributions by a certain algorithm or rule. Nowadays, the Monte Carlo method is a fundamental element in many areas, such as natural sciences, economics, mathematics, sociology, etc. where it is hardly possible or even impossible to calculate exact analytical solutions due to the complexity of the problems. In physics it has become one of the most important tools, especially for statistical mechanics. Computer simulations couple analytical theory and experiment. The ability to both control important parameters and to shield side actions, as well as the reproducibility and perfect observability are strong points of numerical methods. One can set up model systems with special parameters without huge experimental effort and change parameters such as temperature, dimension, particle number, etc. independently of each other.

3.1.1. Basic concepts of Monte Carlo simulations

The most famous and in various mutations widely spread Monte Carlo algorithm is the Metropolis algorithm, a method to simulate the equilibrium properties of physical systems. It was proposed by Metropolis *et al.* [58] in 1953 for simulating hard-spheres. The sampling principle of this algorithm is called *importance sampling*. One starts from the information that the desired distribution of a canonical equilibrium system is the Boltzmann distribution. States of the system are created such that states that contribute strongly at a certain temperature $T = T_0$ occur more often than states that

are less relevant to the mean value. In order to do that, configurations are not created independently of each other—as is the case in simple sampling algorithms—but a new configuration β depends on its preceding configuration α (preceding here refers to the time series of configurations). A sequence of configurations created by following this principle is called a *Markov chain*[5]. A crucial requirement for an algorithm to simulate equilibrium is the *detailed balance* condition—also called micro reversibility—and to be ergodic. The first reads:

$$P_{\alpha\to\beta}\rho^*_\alpha = P_{\beta\to\alpha}\rho^*_\beta, \tag{3.1}$$

where $P_{\alpha\to\beta}$ is the transition probability to go from state α to state β and ρ^*_α is the equilibrium (Boltzmann) probability to be at state α, $\rho^*_\alpha \propto e^{-E_\alpha/k_BT}$. E_α is the energy of state α. The second requirement states that each state is visited in a finite number of steps. The transition probability $P_{\alpha\to\beta}$ again consists of two parts.

$$P_{\alpha\to\beta} = g(\alpha\to\beta)A(\alpha\to\beta), \tag{3.2}$$

where $g(\alpha\to\beta)$ is the probability to generate a target state β being at a state α and $A(\alpha\to\beta)$ is called the acceptance ratio for the new state β. All selection probabilities $g(\alpha\to\beta)$ that are different from zero are set equal in the Metropolis algorithm. The famous Metropolis criterion is the acceptance ratio of the Metropolis algorithm:

$$A(\alpha\to\beta) = \min\left[1, \frac{\rho^*_\beta}{\rho^*_\alpha}\right] = \begin{cases} 1 & : \text{ if } \Delta E \le 0 \\ e^{-\beta\Delta E} & : \text{ if } \Delta E > 0 \end{cases}. \tag{3.3}$$

For the proof that this algorithm leads to equilibrium and further developments of this algorithm I refer to the standard literature e.g. [75, 84].

In a foregoing work [85], I applied the Metropolis algorithm to the problem at hand. This practically means to create an initial polymer configuration defined by $N+1$ monomers at positions $\mathbf{r}_i$. The connecting lines between the monomers define tangent vectors $\mathbf{t}_i$ (recall Sec. 2.1.1). The intrinsic energy of the polymers is determined by the angles between neighboring tangent vectors. An additional energy term comes from the potential. An overlap of a monomer with a disk of the potential means infinite energy and thus the corresponding acceptance ratio is zero. Sampling according to the Metropolis algorithm means starting with an initial configuration and updating it. This is carried out by proposing new randomly drawn monomer positions. The new angles between the tangent vectors are accepted or rejected according to the Metropolis criterion, Eq. (3.3). For a highly dense background, however, this method results in a rejection rate that makes it impossible to create enough configurations to compute observables, yielding a diverging autocorrelation time, which is—roughly speaking—the time scale over which observations of the system look similar[6]. For this reason, I applied another method which is introduced in Sec. 3.3.

[5] For more details on the properties and characteristics of Markov chains, have a look at e.g. [82, 83, 84].

[6] Time here refers to Monte Carlo time, i.e. Monte Carlo steps. For more information about the autocorrelation time I refer to [86].

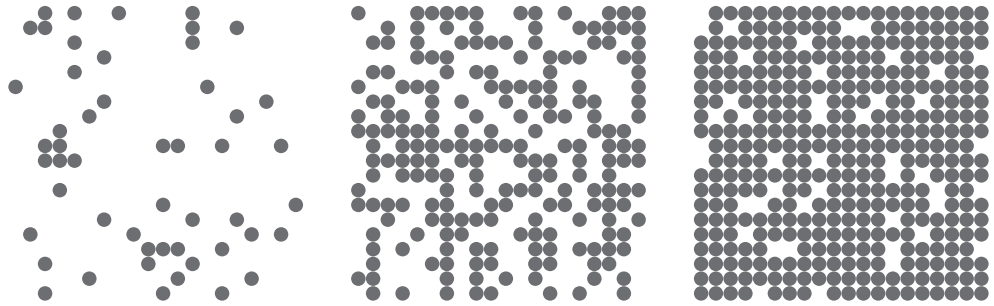

Figure 3.1.: Exemplary lattice disorder configuration with site occupation probability $p = 0.13$ (a), $p = 0.51$ (b), and $p = 0.89$ (c).

3.2. Hard-disk disorder

As stated in Sec. 2.2, I focus on two ways of arranging the disks. One is putting the them onto the sites of a square lattice. The other is arranging them as members of an ensemble of hard-disk fluid configurations. While the first is straightforward, the second way is more involved.

3.2.1. Lattice disorder

I generate random configurations by occupying a square lattice with 20×20 sites successively with the same probability, the lattice occupation p. The resulting structure resembles the structure of a diluted square lattice. I chose the values of p as[7]: $p = 0, 0.13, 0.25, 0.38, 0.51, 0.64, 0.76, 0.89, 1$ (Fig. 3.1 shows three examples of disorder configurations that are modeled as described above). As each site is occupied independently of the other sites, there are no correlations between occupied sites.

3.2.2. Hard-disk fluid

I set up hard-disk fluid configurations at area fraction ρ by first creating a configuration of hard disks using Random Sequential Addition (RSA) [87]: the disks are sequentially inserted into the simulation area at random positions, the disks may not overlap and an object that has been put to a position according to the first two rules is irreversibly fixed at its position. I create RSA configurations up to $\rho = 0.5$. For increasing the density even more (up to $\rho = 0.7$) the radii of the disks of an RSA configuration are increased until two disks that have the smallest distance touch. The positions of the disks are slightly shifted such that there is again a finite distance between any two disks. The procedure then starts again and proceeds step by step until the desired area

[7] For a disk diameter of $\sigma = 0.05$, the chosen occupation probabilities correspond to area fractions $\rho = 0, 0.1, 0.2, 0.3, 0.4, 0.5, 0.6, 0.7, 0.785$. Except for $\rho = 0.785$, these area fractions are utilized for the case of hard-disk fluid disorder later on.

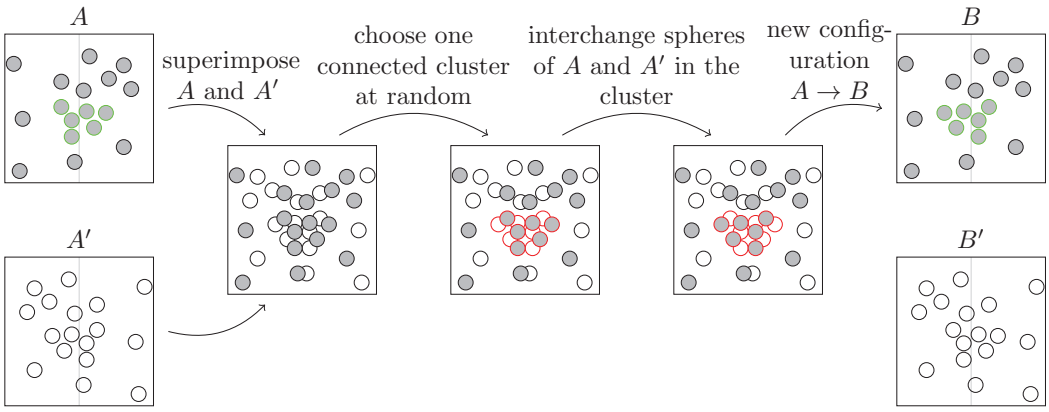

Figure 3.2.: Algorithm to equilibrate hard-disk configurations.

fraction is reached. The configurations set up by RSA are not yet in thermodynamic equilibrium contrasting the case of hard-disk fluid configurations [75, 88, 89]. An alternative to RSA would be to generate a distribution of disks at area fraction ρ by occupying the sites of a lattice (e.g. square lattice) randomly. It turns out, however, that equilibration (cp. next paragraph) becomes rather inefficient for lattice initial conditions, especially for high disorder densities.

In order to get hard-disk fluid configurations out of the previously created configurations, the configurations need to be equilibrated. Metropolis-like and Molecular Dynamics algorithms turn out to be of no big use for this purpose, especially for the case of high densities. The reason is the high or even diverging autocorrelation time needed to create independent snapshots of the system, as it gets extremely difficult to escape from jammed states by changing single particle positions. This can be overcome by applying a cluster algorithm, as the Pivot Cluster Algorithm (PCA) proposed by Dress and Krauth [88], where coordinated moves of several particles at one step are constructed. In the following, I will give a short sketch of the basic idea of the PCA.

Principle of the Pivot Cluster Algorithm [75, 85]

The coordinated move of several particles makes it possible to get from one realization A to a very different realization B. In order to get an "equilibrium" realization, the PCA has to fulfill detailed balance. It will become clear in a few moments that this condition is satisfied.

Consider a realization A of hard disks and a copy of this realization A' with all disks reflected about a symmetry axis. These two realizations are superimposed. Disks of the original realization and the reflected realization will overlap and form connected clusters. We take one of these clusters and replace the disks of the original cluster A with the disks of the reflected cluster A' (see Fig. 3.2). In the example of Fig. 3.2, the green marked disks of cluster A become the green marked disks of cluster B. The

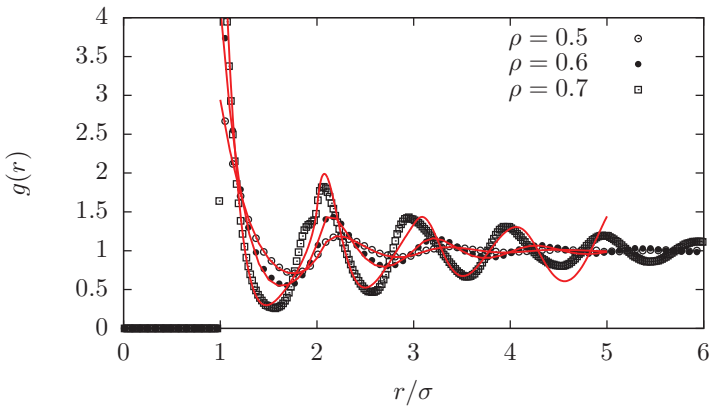

Figure 3.3.: The data indicated by the plot markers are from simulations, the solid (red) lines are the numerical evaluation of the analytical solution of the Percus-Yevick approximation [78] which is only valid in the low-density regime.

mirror plane is displayed as vertical gray line in Fig. 3.2.

In order to show that this method fulfills detailed balance, we have to look at the probability to move back from B to A. For this, imagine the superimposition of B and B'. The probability of choosing the cluster that was transformed in the transition from A to B is the same as to choose this cluster for the inverse move because they have equal size. Having chosen the same cluster that was transformed from A to B, the same symmetry transformation as before leads us back to configuration A. This is why this algorithm satisfies detailed balance. As any local transformation, which means moving only one disk for one update, can be attained by consecutive execution of horizontal and vertical reflections, ergodicity of the PCA holds for the same reason as for local algorithms. Horizontal and vertical symmetry axes can be chosen at arbitrary positions (the boundaries are periodic). Being rejection-free makes this algorithm very useful and efficient. For high densities (in my case this happened at $\rho = 0.7$, which is slightly below the freezing transition), however, the applicability of this algorithm is limited, because then a long range symmetry transformation will comprise nearly all particles in one large cluster. Flipping it just mirrors the whole configuration. This can only be avoided if symmetry transformations are restricted to very short ranges. In this case, the method exhibits no advantage over local algorithms.

I characterize the resulting disorder configurations by computing the radial distribution function (RDF) $g(r)$. I find perfect agreement of my simulation data with literature (cp. e.g. [89]). Besides, the data cover well the analytical solution of the Percus-Yevick approximation of the RDF $g(r)$ [78, 90] (cp. the red solid lines in Fig. 3.3), which is a good approximation in the low-density regime. Near the freezing transition it is no longer an accurate description of the structure of hard-disk fluids.

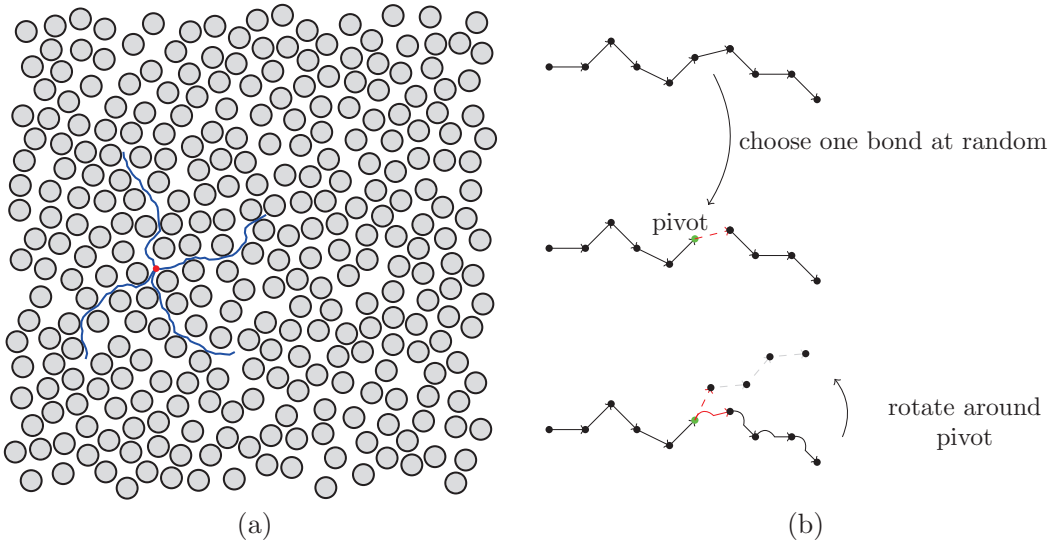

Figure 3.4.: (a) Disorder realization at area fraction $\rho = 0.6$ and four exemplary polymer configurations that have their starting point—marked red—in common.
(b) Principle of the pivot update.

3.3. Growth algorithms

As already stated above, a standard Markov chain Monte Carlo (MCMC) method does not work well for simulating a polymer in a high-density disorder landscape. For a better understanding of this, consider a disorder realization and four polymer configurations as can be seen in Fig. 3.4(a). An attempt to construct a new configuration out of one of the existing by an update routine as the pivot algorithm [see Fig. 3.4(b)] results either in a configuration which differs hardly from the initial configuration or overlaps most likely with the disks of the background potential.

An attempt to overcome this problem is to apply another class of algorithms—growth algorithms—which is done throughout this work. The principle of growth algorithms is setting up an ensemble of polymer configurations by growing each polymer monomer by monomer instead of changing an already existing configuration.

In the following I give a short introduction to the growth algorithm by Rosenbluth and Rosenbluth [91], which can be regarded as forefather of growth algorithms. After this I will in detail explain the growth method proposed by Garel and Orland [92] which I used for my simulations.

3.3.1. Rosenbluth growth algorithm

In 1954, Rosenbluth and Rosenbluth [91] examined the average extension of flexible molecular chains on a cubic lattice. In the absence of energy terms, each configuration

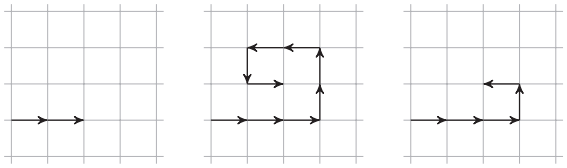

Figure 3.5.: In case (a) there are three lattice sites that can be occupied in the next step. Case (b) is called "terminating chain" because a continuation of the chain is not possible. A weight has to be introduced in (c) where only two lattice sites can be occupied in the next step.

with N monomers has the same probability. The idea was to occupy a sequence of lattice sites one after the other. Self-avoidance is implemented by the requirement that the chains are not allowed to cross themselves. Having built up a molecular chain as in Fig. 3.5(a) there are three lattice sites that can be occupied by the next monomer in two dimensions. Therefore one of these three possibilities is chosen at random with a probability of 1/3. A configuration as in Fig. 3.5(b) is called "terminating chain", because it is not possible to occupy another lattice site without violating the self-avoidance condition. Such a configuration is erased and a new chain is started. The crucial idea of the algorithm becomes clear if one considers a configuration as in Fig. 3.5(c). For such a configuration there are only two possibilities that can be chosen for the next monomer. Choosing one of them with probability 1/2 would make the emerging chain more probable than configurations where all sites were chosen with probability 1/3. Therefore the total chain is weighted with a special weighting function every time when a new monomer is added. The weighting function reads

$$W_{m+1} = \frac{n}{3} W_m(W_1 = 1), \tag{3.4}$$

where n denotes the number of possibilities for the next monomer. The number in the denominator of Eq. (3.4) depends on the dimension. It is $2d - 1$. The arising chain configurations have all the same probability.

Various algorithms were built upon the principle of the growth algorithm by Rosenbluth and Rosenbluth, see [92, 93, 94, 95, 96].

3.3.2. Off-lattice growth algorithm

The method proposed by Garel and Orland [92] is a growth algorithm for lattice and off-lattice polymers. Every polymer of the ensemble is grown monomer by monomer and is weighted according to its Boltzmann weight in each growth step as in the Rosenbluth algorithm. Contrasting the Rosenbluth method, the weighting is achieved by replicating or deleting chains and is thus coded in the number of chains with a certain energy.

In a Boltzmann distribution of polymer chains, the probability to find a chain with

energy E is proportional to its Boltzmann weight $e^{-\beta E}/Z$, where $\beta = 1/k_B T$ and Z the partition function of the ensemble. The idea is to replicate a chain with energy E proportional to $e^{-\beta E}$.

I demonstrate the basic principle of this method at the example of a free Heisenberg chain. The bending energy E_{bend} belonging to a bending angle θ is [recall Eq. (2.1) and Fig. 2.1]

$$E_{\text{bend}} = -J \cos\theta. \tag{3.5}$$

The procedure begins with a number of $\mathcal{M}_1$ (the initial number of chains)—in the example of Fig. 3.6, $\mathcal{M}_1 = 3$—monomers at the initial position $\mathbf{r}_1$ [Fig. 3.6(a)]. Every one of these is a seed for a polymer chain. The chains are independent of each other. In the next step a new monomer at position $\mathbf{r}_{2_i}$ is randomly drawn for every seed [Fig.3.6(b)]. Randomly refers to a position a bond length b apart with an angle taken out of a uniform distribution from the interval $[0, 2\pi)$. Up to this point there is still no energy contributing as at least two bonds are required to have bending. In the example of Fig. 3.6, there are three chains of length one up to now, $\{\{\mathbf{r}_1,\mathbf{r}_{2_1}\},\{\mathbf{r}_1,\mathbf{r}_{2_2}\},\{\mathbf{r}_1,\mathbf{r}_{2_3}\}\}$. The first contribution of energy comes into play in step three. Again a new monomer is added to each of the chains just the same as in step two. The chain configurations to this point are $\{\{\mathbf{r}_1,\mathbf{r}_{2_1},\mathbf{r}_{3_1}\},\{\mathbf{r}_1,\mathbf{r}_{2_2},\mathbf{r}_{3_2}\},\{\mathbf{r}_1,\mathbf{r}_{2_3},\mathbf{r}_{3_3}\}\}$. The bending angles between neighboring bonds are α between bond $\overrightarrow{\mathbf{r}_1,\mathbf{r}_{2_1}}$ and $\overrightarrow{\mathbf{r}_{2_1},\mathbf{r}_{3_1}}$, β between bond $\overrightarrow{\mathbf{r}_1,\mathbf{r}_{2_2}}$ and $\overrightarrow{\mathbf{r}_{2_2},\mathbf{r}_{3_2}}$, and γ between $\overrightarrow{\mathbf{r}_1,\mathbf{r}_{2_3}}$ and $\overrightarrow{\mathbf{r}_{2_3},\mathbf{r}_{3_3}}$.

The Boltzmann weight belonging to the bending angle α reads

$$w_3(\alpha) = w_3(\mathbf{r}_{3_1}|\mathbf{r}_1,\mathbf{r}_{2_1}) = e^{-\beta E_{\text{bend}}} = e^{\beta\cos\alpha}. \tag{3.6}$$

Equation (3.6) has to be read as follows. The index i at w_i marks the growth step that is currently worked on. The weight assigned to α, that is $w_3(\alpha)$, belongs to a configuration with a monomer at position r_{3_1} under the condition that the previous monomers are at position r_1 and r_{2_1}. This is why $w_3(\alpha)$ must be understood as $w_3(\mathbf{r}_{3_1}|\mathbf{r}_1,\mathbf{r}_{2_1})$. The corresponding weights are assigned to the configurations belonging to β and γ. The assignment of the weight to a configuration is implemented by replicating it after w_i. $i_i = \text{Int}(w_i)$ is defined as the integer part of w_i and $r_i = w_i - i_i$ as the rest. Replicating the new chain w_i times statistically means replicating it i_i times plus one additional time with probability r_i. Therefore a random number r with $0 \le r \le 1$ is drawn. If $r \ge r_i$, the chain is replicated i_i times. Otherwise it is replicated $(i_i + 1)$ times. Since w_i can be smaller than 1, the replication can in fact amount to a deletion. This is why the method is called replication-deletion-procedure (RDP). The growth procedure has to be applied to each monomer. In growth step three this leads to a Boltzmann distribution of trimers. In the example of Fig. 3.6, the coupling J and the temperature T where chosen such that the weights result in the numbers given in Fig. 3.6(d). The chain belonging to α is replicated once, the one belonging to β three times, and the polymer configuration belonging to γ is deleted. The configuration belonging to β is now counted as three different configurations that are continued independently of the others as is indicated in Fig. 3.6(e). This method is iterated by applying it to each of the trimer chains, and so on. Going ahead with this

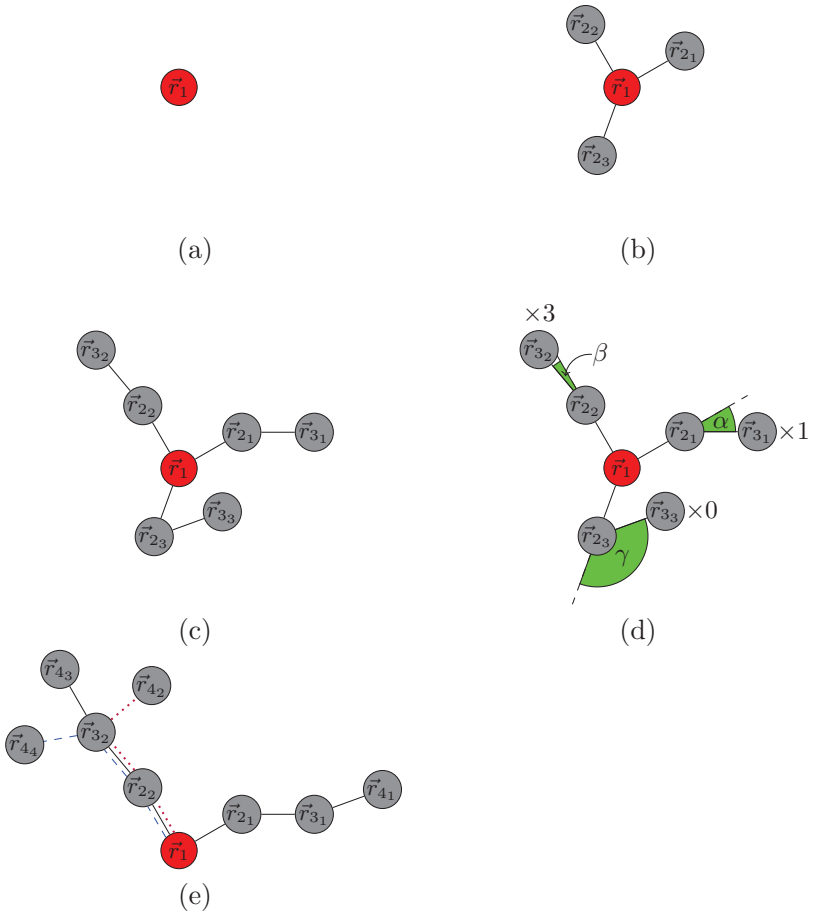

Figure 3.6.: (a) $\mathcal{M}_1$ monomers at position $\mathbf{r}_1$. The first monomer—here marked by ●—thus stands for $\mathcal{M}_1$ (three in this example) different chains of zero length.
(b) Each of the $\mathcal{M}_1$ chains is extended by one monomer. There are now $M_2 = 3$ independent chains of length one. Up to now, there is no energy term as there is no bending angle between neighboring bonds.
(c) Each of the M_2 chains is extended by one monomer. There are now $M_3 = 3$ independent chains of length two.
(d) Now, energy comes into play as there is a bending angle between the first and second bond of the polymers. Temperature and coupling constant J are chosen such that they give the weights that are given in the sketch $(\times 3, \times 1, \times 0)$. Each of the chains is replicated according to its weight. Accordingly $M_{3_{\text{new}}} = 4$. There are now four independent chains of length two.
(e) Each of these chains is extended independently by one monomer and bond. This procedure is iterated until the desired degree of polymerization is reached.

procedure until the desired segment number N is reached, one obtains a population of Boltzmann distributed chains of length N, as shown in [92].

I will go into this proof in the next section. As one can imagine, the efficiency of this algorithm depends strongly on the energy landscape. Furthermore, for some choice of the coupling constant J and the temperature T, the weights in Eq. (3.6) can quickly diverge or converge to zero, as they depend exponentially on J, T, and $\cos\theta$. To overcome the problem of exponential replication or deletion, a *population control parameter* is introduced (see p. 44). It controls the overall number of configurations. Additionally there is a way to increase the efficiency of the algorithm by preferring certain angle intervals over others depending on the energy landscape of the system. This is done by a *guiding field* (see p. 46). The bias of overvaluing certain angles has to be cured again in order to keep the ensemble Boltzmann distributed.

Proof of correct sampling

For the proof consider the Hamiltonian of the free Heisenberg chain, Eq. (2.1), which contains only energetic contributions from bending between neighboring bonds. The bending energy is described by Eq. (3.5). The proof for general potentials and interactions can be found in [92]. The number of chains belonging to one configuration in growth step i is M_i and the overall number of chains is $\mathcal{M}_i$. At stage one and two there are $\mathcal{M}_1$ chains of length zero and one, respectively. For $i > 2$, the newly added monomers bring along new bonds that enclose bending angles with their predecessors thus contributing bending energy. Each configuration is now weighted according to its Boltzmann factor. The number of chains belonging to a certain configuration in this step is

$$M_3(\mathbf{r}_1, \mathbf{r}_2, \mathbf{r}_3) = w_3(\mathbf{r}_3|\mathbf{r}_1, \mathbf{r}_2) \times M_2 = w_3(\mathbf{r}_3|\mathbf{r}_1, \mathbf{r}_2) \times M_1. \tag{3.7}$$

The last identity comes from the fact that in our case $M_1 = M_2$. In Eq. (3.6) we addressed the weight for a configuration in growth step three. Generalized to $i+1$ and using the relation between monomer position $\mathbf{r}_i$ and tangent vector $\mathbf{t}_i$, $\mathbf{t}_i = (\mathbf{r}_{i+1} - \mathbf{r}_i)/b$, w_{i+1} reads:

$$w_{i+1}(\mathbf{r}_{i+1}|\mathbf{r}_1, \ldots, \mathbf{r}_i) = \exp[\beta J \cos(\theta_{\mathbf{t}_i, \mathbf{t}_{i-1}})] = \exp[\beta J(\mathbf{t}_i \cdot \mathbf{t}_{i-1})], i > 1. \tag{3.8}$$

Accordingly M_{i+1} yields:

$$M_{i+1}(\mathbf{r}_1, \ldots, \mathbf{r}_i, \mathbf{r}_{i+1}) = w_{i+1}(\mathbf{r}_{i+1}|\mathbf{r}_1, \ldots, \mathbf{r}_i) \times M_i(\mathbf{r}_1, \ldots, \mathbf{r}_i). \tag{3.9}$$

Going ahead until the desired degree of polymerization $N+1$ (remember that N indicates the number of bonds and thus $N+1$ is the number of monomers, see Sec. 2.1.1) is reached, the overall number of polymer chains having $N+1$ monomers is $\mathcal{M}_{N+1}$. From Eq. (3.9) we find

$$M_{N+1} = w_{N+1}(\mathbf{r}_{N+1}|\mathbf{r}_1, \ldots, \mathbf{r}_N) \times w_N(\mathbf{r}_N|\mathbf{r}_1, \ldots, \mathbf{r}_{N-1}) \times \ldots \times w_3(\mathbf{r}_3|\mathbf{r}_1, \mathbf{r}_1) \times M_1. \tag{3.10}$$

Inserting the weights from Eq. (3.8) into Eq. (3.10), we finally find

$$\begin{aligned} M_{N+1} &= \exp(\beta J(\mathbf{t}_N \mathbf{t}_{N-1})) \times \exp(\beta J(\mathbf{t}_{N-1} \mathbf{t}_{N-2})) \times \ldots \times \exp(\beta J(\mathbf{t}_2 \mathbf{t}_1)) \times M_1 \\ &= \exp(\beta J \sum_{i=2}^{N} \mathbf{t}_i \cdot \mathbf{t}_{i-1}) \times M_1 \overset{\text{Eq. (2.1)}}{=} \exp(-\beta \mathcal{H}) \times M_1. \end{aligned} \tag{3.11}$$

Consequently, the probability to find a chain of a given energy is given by its Boltzmann weight. At the beginning of this section I mentioned that the proof is limited to the case of a free polymer. The extension to the kind of interaction potential I am considering throughout this work—a potential consisting of hard disks—is straightforward. The Hamiltonian for an additional monomer and hence an additional bond has to be extended by the potential term described in Eq. (2.20). The weight for the (i+1)th step then reads:

$$w_{i+1}(\mathbf{r}_{i+1} | \mathbf{r}_1, \ldots, \mathbf{r}_i) = \exp[\beta J(\mathbf{t}_i \cdot \mathbf{t}_{i-1}) - \beta V_\sigma(r)], i > 1. \tag{3.12}$$

Practically, this just means that the weight is set to zero if the new monomer overlaps with a disk of the background potential and thus every chain that overlaps with a disk immediately vanishes from the distribution.

Figure 3.7 shows six exemplary situations from a simulation. The coupling J [recall Sec. 2.1.1 in particular Eq. (2.1)] is chosen such that $K := J/k_BT = 7.25$. For 30

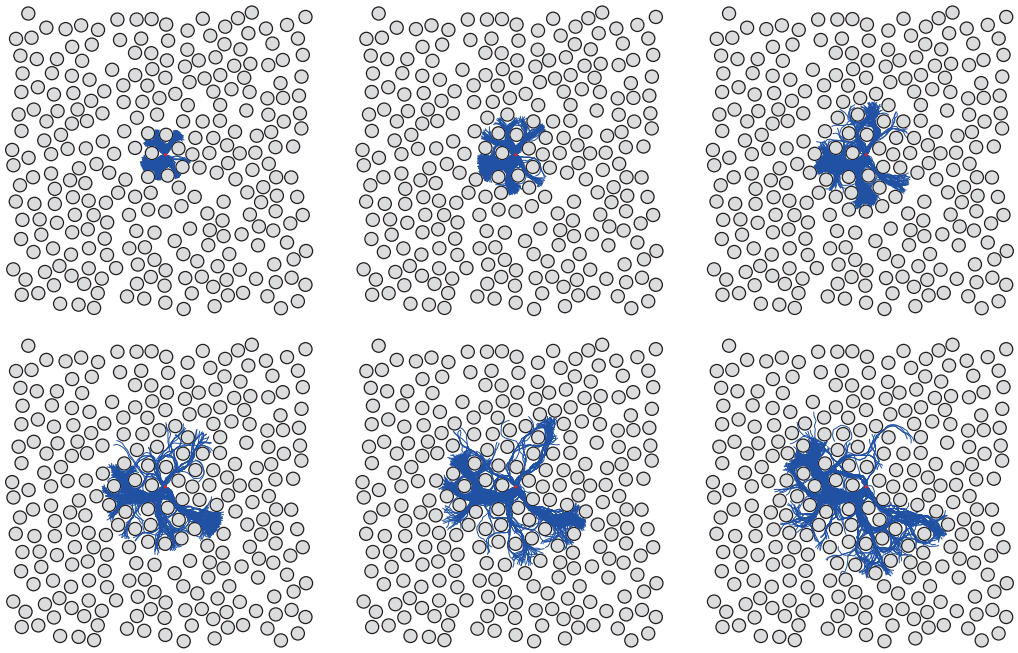

Figure 3.7.: Six stages of the off-lattice growth method (extract from the corresponding ensembles).

monomers, this corresponds to a persistence length of half the total polymer length if the polymer is not exposed to a potential [$\xi = 0.5$, Eq. (2.11)].

Population control parameter

From the previous section we see that the off-lattice growth algorithm in the form of a replication-deletion procedure (RDP) leads in principle to a Boltzmann distribution of chains. In practice, however, some technical considerations have to be taken into account. For getting an impression of the necessity of the population control parameter for the case we are considering, have a look at Fig. 3.8. The sketch shows a strongly magnified situation taken from a simulation. A polymer with no bending energy ($J = 0$) is simulated in a background of hard disks at a volume fraction $\rho = 0.6$. The disk diameter is $\sigma = 0.05$ and the polymers have a bond length of $b = 0.01$. For reasons of visibility, the number of chains is limited to 50. The check for overlaps is left out. Figure 3.8(a) is at growth step one, which means two monomers. One is the initial and one at a random position a bond length b apart. Zero coupling means that the weight can either be zero, in case a monomer overlaps with a disk, or one otherwise. Already in step one, Fig. 3.8(a), many of the chains overlap with a disk of the background. As the mean extension of a free chain with the given parameters is much larger than the mean free length between the disks, one will hardly find any configuration that does not have at least one overlap with a disk of the background, as can be guessed from Figure 3.8(b). Consequently, for computationally tractable ensemble sizes, the whole population will die out and no chains will be left. The other extreme is a potential that strongly increases the weight of some configurations. The exponential weight factor will lead to a population that quickly exceeds the capacity of the computer.

The population control parameter (PCP) takes advantage of the fact that it is very

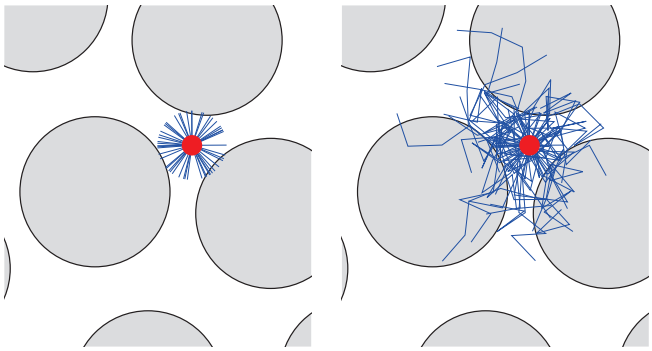

(a) (b)

Figure 3.8.: The sketch illustrates the necessity of the population control parameter. The check for overlaps is left in this example. The explanation is given in the text.

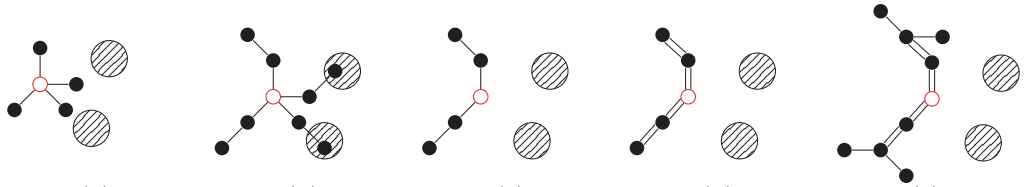

Figure 3.9.: (a) Initial growth in four different directions corresponds to four different polymer chains of length 1 starting from the seed marked by the red open circle (○). (b) Each of the chains is grown by one monomer. Two of the chains overlap with a disk of the background potential. The weight of these chains is 0. (c) The chains with weight 0 are removed from the population. (d) The population control parameter keeps the overall number of chains approximately constant. On average each of the remaining chains is thus replicated and now exists twice in the population. (e) Each of the chains is grown independently by one more monomer.

improbable that all chains disappear within a single growth step. It keeps the overall number of chains about constant, thus preventing the population from either dying out or growing overwhelmingly. I illustrate the concept of the PCP at the example of a confining potential [see Fig. 3.4]. From the description of the RDP we know that the Boltzmann distribution is coded in the number of chains M_{N+1} belonging to certain configurations. The key to the Boltzmann distribution thus lies in the ratio of the different configurations that have certain energies, not in the overall number of chains $\mathcal{M}_{N+1}$. Multiplying the weight of all chains by the same numerical value hence does not alter the structure of the distribution. The overall number of chains in each growth step is determined by the weights of all of the newly added bonds. In order to keep the overall number of chains at about the size of the initial number of chains $\mathcal{M}_1$, the PCP is defined as follows:

$$g_i = \frac{\mathrm{INC}}{\mathrm{ENC}_i} = \frac{\mathcal{M}_1}{\mathrm{ENC}_i}, \tag{3.13}$$

where g_i is the population control parameter in growth step i, INC is the initial number of chains, that is $\mathcal{M}_1$, and ENC_i stands for the estimated number of chains in growth step i. ENC_i is determined as the sum of the replication weights w_i. After g_i is calculated, each of the weights is multiplied by g_i. $w_{i+1}(\mathbf{r}_{i+1}|\mathbf{r}_1,\ldots,\mathbf{r}_i)$ [Eq. (3.8)] hence results in:

$$w_{i+1}(\mathbf{r}_{i+1}|\mathbf{r}_1,\ldots,\mathbf{r}_i) = g_{i+1}\exp(\beta J \mathbf{t}_i\cdot\mathbf{t}_{i-1}). \tag{3.14}$$

This is done in each step such that at the end, step $N+1$, the number of chains $M_{N+1}(\mathbf{r}_0,\ldots,\mathbf{r}_{N+1})$ reads:

$$M_{N+1} = g_1\ldots g_{N+1}\times\exp(\beta J\sum_{i=2}^{N}\mathbf{t}_i\cdot\mathbf{t}_{i-1})\times M_1, \tag{3.15}$$

which again represents a Boltzmann distribution. The numerical implementation will be addressed in the next section, Sec. 3.3.2.

We have seen, that the RDP generates a population of chains that is Boltzmann distributed. To be more precise, we have seen that this procedure provides such a distribution in each growth step. A strong advantage thereof is to be able to do a scaling analysis within one simulation. Having a distribution of chains of length N automatically provides all the distributions of length $\tilde{N} = 1, \ldots, N$. I found by comparison with the multicanonical method that correlations due to the growth process which would pass a possible bias from ensembles of short chains to those of longer chains can largely be excluded. More on the correlations of chains will be discussed in Sec. 3.4.

Guiding field

Though getting distributions of all length up to the desired degree of polymerization within one simulation is an advantage for scaling analyses, it is a drawback concerning the question of ergodicity. Depending on the choice of the potential, the polymer chain might, e.g., get stuck in a local energy minimum which hinders the chain from sampling phase space evenly enough to provide a Boltzmann distributed population of chains that satisfies the ergodicity condition. This drawback can be cured by introducing a guiding field that locally makes the distribution of chains non Boltzmann distributed thus facilitating to sample phase space more uniformly by forcing the chain to circumvent or get out of local energy minima. A second aspect of the guiding field is to make the algorithm much more efficient. The way I use the guiding field differs slightly from the original paper by Garel and Orland [92]. For the case of an arbitrary continuous potential I refer to the given paper. For my case I basically biased the distribution by drawing angles not uniformly but from another distribution which is inspired by the nature of the problem. Afterwards, the weights are adapted such that the resulting distribution is unbiased. This procedure is done in two steps which I will explain one thing at a time. The guiding field is made up of two parts one of whom accounts for the bending energy of the polymer and one for the disks of the background potential. I first show the principle for the bending energy. Instead of drawing a random angle from a uniform distribution, the bending energy is taken account of by drawing a certain angle θ from the distribution

$$P(\theta) \propto \exp[\beta J \cos(\theta)]. \tag{3.16}$$

The cosine in Eq. (3.16) can be replaced by the quadratic term of its taylor expansion for small angles:

$$P(\theta) \propto \exp[\beta J \cos(\theta)] \approx \exp[\beta J(1 - \tfrac{1}{2}\theta^2)]. \tag{3.17}$$

We rewrite βJ in Eq. (3.17) in terms of the persistence length measured in units of bonds, $\tilde{\ell_p} = \ell_p/b = 2\beta J$. Substituting this into Eq. (3.17) and normalizing yields:

$$P(\theta) = \frac{1}{\sqrt{2\pi(0.5\tilde{\ell_p})^{-1}}} \exp(-\tfrac{\theta^2}{2(0.5\tilde{\ell_p})^{-1}}), \tag{3.18}$$

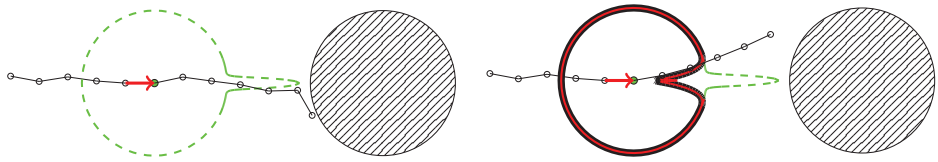

(a) (b)

Figure 3.10.: Background-aware guiding field.

which is a Gaussian distribution with variance $\sigma_{\mathrm{gf}}^2 = (0.5\tilde{\ell_p})^{-1}$. For a persistence length[8] of $\xi = 0.5$ and 30 monomers, the variance amounts to $\sigma_{\mathrm{gf}}^2 \approx 0.14$, which approximates Eq. (3.16) fairly well. The approximation improves with increasing persistence. The exact approximation of the Gaussian is, however, not necessary, as the bias that enters the distribution through the guiding field is amended later on. Hence I draw angles out of a Gaussian distribution with variance $\sigma_{\mathrm{gf}}^2 = (0.5\tilde{\ell_p})^{-1}$ instead of from a uniform distribution. This bias is cured by dividing the weight of the corresponding configuration by the probability for choosing this angle. The weight $w_{i+1}(\mathbf{r}_{i+1}|\mathbf{r}_1,\ldots,\mathbf{r}_i)$ with $\theta_{\mathbf{t}_i,\mathbf{t}_{i-1}}$ being the angle between $\mathbf{t}_i$ and $\mathbf{t}_{i-1}$ consequently reads

$$w_{i+1}(\mathbf{r}_{i+1}|\mathbf{r}_1,\ldots,\mathbf{r}_i) = \frac{1}{P(\theta_i)} g_i \exp[\beta J \cos(\theta_{\mathbf{t}_i,\mathbf{t}_{i-1}})]. \tag{3.19}$$

As an illustration of the gain in efficiency consider a polymer with $N+1 = 30$ monomers with a persistence length of $\xi = 0.5$. This corresponds to a variance of $\sigma_{\mathrm{gf}}^2 \approx 0.14$ and accordingly a standard deviation of $\sigma_{\mathrm{gf}} \approx 0.37$. As about two-thirds of the angles come from the interval between $[-\sigma_{\mathrm{gf}}, \sigma_{\mathrm{gf}}]$, the gain in efficiency for each monomer amounts in a factor of 3–4 compared to drawing angles from a uniform distribution and increases with increasing persistence length.

In the next step, the influence of the disks is included into the guiding field. Assume a situation as sketched in Fig. 3.10(a), where a polymer with a certain bending stiffness grows in the direction that is indicated by the arrow. The hatched disk is an obstacle located in the growth direction. The dashed (green) line indicates the guiding field based solely upon the bending stiffness. Both the guiding field and the Boltzmann weight favor a growth in the direction of the bond indicated by the arrow (red) and thereby in the direction of the obstacle. The polymer does not sense the obstacle until it is one bond length away of it. It is obvious that only a large bending angle can prevent the polymer from overlapping with the obstacle. Depending on the bending stiffness, the resulting weight will be rather small and the configuration does not contribute a lot or might even die out. This problem is based upon the update routine that only takes into account its directly surrounding area.

A way to overcome this problem is to introduce a guiding field that involves a certain amount of foresight in navigating around obstructed areas. Such a guiding field

[8] Remember that ξ gives the persistence length in units of total polymer length whereas ℓ_p gives its real numerical length.

is depicted in Fig. 3.10(b). The probability of choosing an angle that leads in the direction of an obstacle is reduced [framed (black) curve]. The corresponding probability density considers only disks within a certain distance and adds for each disk a Gaussian dip with a certain amplitude and variance. The form of the probability density and the parameters are determined empirically and by intuition. Both, amplitude and variance, are a function of the distance between obstacle and monomer of current growth and the persistence length. The emerging growth direction is a superposition of the contributions from the persistence of the polymer and from the surrounding potential. It is evident that a polymer with a larger persistence length has to sense the obstacles more in advance than one with a smaller, because the probabilistic suppression of certain angles depends exponentially on the bending stiffness. The numerical implementation of the guiding field and the accordant parameters are given in the next section.

Remark on the numerical implementation of the replication deletion procedure

The last sections covered the methods used throughout this work. In this section I want to discuss briefly some crucial points of the implementation of these methods. I do not want to go into the details of programming but just mention schematically some of the principles. I begin by commenting on the process of measuring distances. Both, the routine that generates hard-disk fluid disorder (see Sec. 3.2.2) and the growth routine for simulating a polymer in a hard-disk potential (Sec. 3.3) spend much of their computing time in calculating distances. Adding a new disk within the routine for setting up the hard-disk fluid as well as adding a monomer in the polymer simulation requires checks for overlaps with disks. For, e.g., the random sequential addition process, the number of checks for adding a new disk is of order $\mathcal{O}(N^2)$ if we want a configuration of N disks. The number of checks can be reduced to $\mathcal{O}(N)$ by applying a so-called grid scheme. The idea of such an approach is to assign each disk to a cell of an appropriate grid. The parameters of the grid have to be chosen in a way that a disk added to one cell of the grid can only overlap with disks of the same cell or disks of adjacent cells (see Fig. 3.11).

The second thing I want to expand on is the numerical implementation of the population control parameter. In order to retain control over the population, each step of growth is processed in two parts. The first is estimating the number of new chain configurations. The second is storing and passing the new configurations and weights to the following step of the routine—the replication-deletion mechanism. In the first step only the new configurations and their corresponding weights are determined. The weights are now used to calculate the population control parameter, Eq. (3.13). In the next step, the replication-deletion step, the weights of each of the configurations is recalculated involving the population control parameter. Then the chains are replicated or deleted according to their weights and are treated as independent new configurations. The RDP leads to chain configurations which are often identical in a large part. The coincident part is stored only once for reasons of storage efficiency.

The last thing that I am commenting on is the guiding field. In the previous section

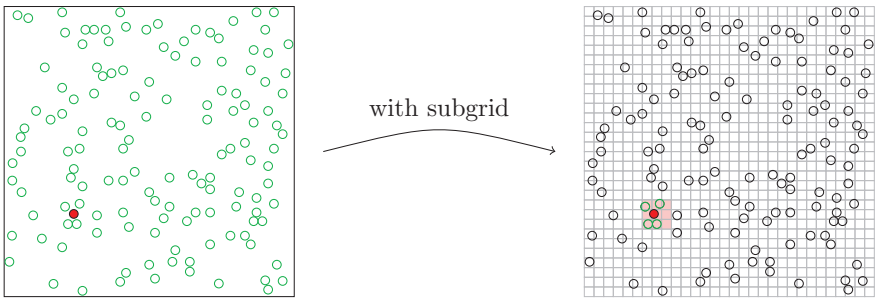

Figure 3.11.: The figure shows schematically the principle of the subgrid structure. It shows the disks (green) that have to be checked for overlaps when the solid (red) disk is added for the case with and without subgrid. The cell size of the subgrid is of the order of the disk diameter.

I already stated that the guiding field is composed of two parts. One covers the persistence of the polymer, the other the disks of the background potential. The first could be implemented by just drawing an angle from a Gaussian distribution [Eq. (3.18)]. With foresight to the second part of the guiding field, the bending is taken care of in a different way. I discretized the interval $[0, 2\pi)$ with a resolution of $2\pi/720$. This discretization is used to initialize a histogram of the interval $[0, 2\pi)$. For setting up histograms I use the histogram library of the GNU Scientific Library. It provides functions for transforming the histogram into a probability density function and drawing random numbers from it.

The second part of the guiding field is treated similarly. At each position of current growth, the disks within a certain radius are considered. Again a histogram on the interval $[0, 2\pi)$ with resolution $2\pi/720$ is generated. Depending on the distance from the current position of growth and the bending stiffness, histograms with Gaussian dips of corresponding variance and amplitude are created. In order to save computing time, the procedure of setting up the histogram is not done in every step but once at the beginning of the simulation. This is possible as the positions of the disks of the background potential stay fixed within the whole simulation. Again the simulation area is subdivided into cells of a certain size—I use the bond length which is 0.01 which leads to 10000 cells as the side length of the simulation area is 1. For each of these cells a histogram with 720 entries is set up according to the above described procedure. Being at a certain growth position, the probability density function of the corresponding cell is multiplied with that of the bending energy.

Other approaches: breadth-first versus depth-first

The method I use is a so-called breadth-first method. With respect to linear growth of polymers, this is building up the desired distribution of polymers in parallel. The information about the distribution (the weights) is coded in the number of different configurations which are grown in parallel. Therefore it is a population based method.

The major drawback of breadth-first is the large memory footprint that is necessary to keep track of all configurations at a time. This is cured by the population control parameter which keeps the population at about constant. Though preventing excess of the memory, it also limits the maximum chain length N which is connected to the size of the population. The longer the chains the more chains are needed in order to calculate averages with sufficient accuracy. This will be discussed in the next section (Sec. 3.4). One possibility (to date the only I know) to keep the population constant and increase the number of monomers is to set up a well-chosen guiding field.

Depth-first builds up one complete polymer chain after the other recursively. The big virtue of this method is its low memory footprint which is due to the fact that only one polymer configuration has to be kept in memory at a time. An attempt to implement the population based method of this work as depth-first would be to grow the branches of the distribution independently and successively. In each step the polymer is replicated after its Boltzmann weight and one of the configurations is continued. This is done until the first has reached the desired degree of polymerization. In this way all chains are built consecutively. Doing so defies the application of a population control parameter, because it depends on the population en bloc. Since discarding the population control parameter strongly limits the applicability of the method, it should primarily be understood as breadth-first.

An off-lattice depth-first growth-algorithm was proposed by Grassberger and Hegger [94]. In order to grasp the idea of depth-first and of what Grassberger and Hegger were doing, we go back to the Rosenbluth-Rosenbluth method of Sec. 3.3.1. A major drawback of the method is the exponential decrease [97, 98] of samples due to ring closures [Fig. 3.5(b)] or intersections of the polymer with itself [Fig. 3.5(c) if the walk is continued downwards] or any other obstacle. Wall and Erpenbeck [97] introduced a procedure to overcome this by enrichment of the samples. They proposed to replicate configurations to prevent from too strong attrition. In order to avoid a bias, the number of replicas of a configuration has to be independent of the configuration that is replicated. Grassberger and Hegger extended this idea, which led to the *pruned-enriched Rosenbluth method* called PERM. The idea of PERM is to grow polymers monomer by monomer and weight each chain according to the Rosenbluth-Rosenbluth procedure. If the weight of a chain exceeds a certain threshold $W_>$, the chain is multiplied by a constant factor (usually it is duplicated) and its weight is divided by this factor (halved). If, on the other hand, the weight of a chain falls below a certain threshold $W_<$, the chain is removed from the population with a certain probability $P_<$ (usually $P_< = 0.5$). If the chain survives, its weight is multiplied by $1/P_<$ (doubled). Both the difficulty and the subtlety in this method is to find the upper and lower threshold $W_>$ and $W_<$. These thresholds are adapted several times during a simulation. The aim is to find roughly the average weight of a chain and to adjust $W_>$ and $W_<$ to this average weight. Finding the average weight or a good alternative for $W_>$ and $W_<$, respectively, can indeed be complicated and might be a drawback of this method for certain situations. The idea of PERM is based upon the Rosenbluth weights. For calculating these weights, the exact knowledge of all possibilities to continue the chain in each step is an essential criterion which for the most part reduces PERM to lattice

polymers. A direct mapping of the Rosenbluth-Rosenbluth idea to off-lattice polymers was done by Smith and Fleming [99]. They calculated the space that is accessible for the next monomer and weighted the chain accordingly. This can only be done for very simplistic models. Here I want to touch in short the "stochastic PERM" which is the approach by Grassberger to adapt PERM to the off-lattice case. Before the actual position of the next monomer is sampled, s sites are drawn from a chosen distribution (subtle choice of the distribution can strongly increase the efficiency of the method). The actual site of the next monomer is chosen among these sites and the weight is computed such that the total sample is unbiased. Pruning and enrichment are done exactly as in the lattice case.

The main reason for applying the breadth-first method throughout this work is the ability of this algorithm to "sense" subtle structures with high resolution. Depending on the weight function, a configuration may be replicated several hundred times and sample its neighborhood in detail. Especially for the case of steric interaction, breadth-first leads to high accuracy results in a complicated high-density disorder structure. A direct comparison to a depth-first method has not been done yet.

3.4. Averaging and error estimation

I consider the background to be static on the timescale of polymer fluctuations. This is taken account of by performing the quenched disorder average for calculating observables. Therefore two averages have to be carried out for calculating mean values. The first is an average over polymer configurations belonging to a single disorder configuration. It is written in angular brackets $\langle \ldots \rangle$. This is done for all disorder realizations and the quenched average is calculated thereof by averaging over the measured values of the single disorder realizations. The quenched average is written as $[\langle ... \rangle]$.

Consequently, two kinds of variances have to be considered, one from the average of polymer configurations within a single disorder realization, and the other from the average over different disorder realizations. These two contributions amount in an effective variance σ^2_{eff} which is estimated by (see e.g. [86]):

$$\sigma^2_{\text{eff}} = \frac{\sigma^2_{\mathcal{O}}}{\sharp\text{realizations}}, \tag{3.20}$$

where $\sigma^2_{\mathcal{O}}$ is the variance of the Monte Carlo mean values over a finite sample of $\sharp$realizations different (independent) disorder realizations. For the error bar we take the standard deviation $\sqrt{\sigma^2_{\text{eff}}}$. The quenched average is carried out over 1500 independent disorder configurations. As an example, Fig. 3.12 shows the error of the mean square end-to-end distance of a polymer chain exposed to a hard-disk disorder landscape. The chain has $N + 1 = 30$ monomers with bond length $b = 0.01$. The disks of the potential have a diameter of $\sigma = 0.05$. The area fraction of the disorder ranges from $\rho = 0, \ldots, 0.7$ and the persistence lengths are $\xi = 0.5$, $\xi = 0.7$, and $\xi = 1$. The structure of the disorder is fluid like. The relative error is on the order of 1%, which is far smaller than the effect of the disorder. These effects will be discussed in detail

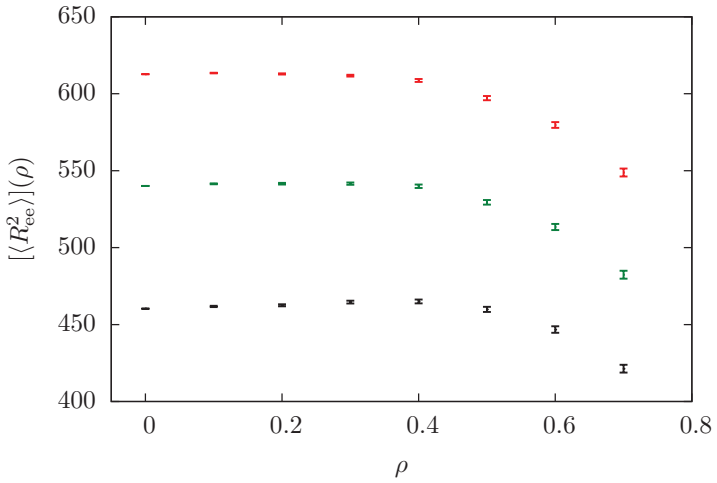

Figure 3.12.: The plot shows the mean square end-to-end distance of a semiflexible polymer exposed to a disorder landscape consisting of hard disks. The error bars for the quenched average over 1500 disorder configurations are shown. The area fraction ranges from $\rho = 0 \ldots 0.7$ which covers the density scope of this work (except for the case of the fully occupied lattice). For better visibility I omitted the plot markers and just plotted the error bars. The different colors distinguish different persistence lengths. Black is $\xi = 0.5$, green 0.7, and red 1 (bottom to top). The latter is the largest persistence length considered throughout this work.

in Sec. 4. For the scale considered here (see Fig. 3.12), the error bars are covered by the plot markers. Therefore I usually omit them.

Things are more complicated for the estimation of the error for the average over polymer configurations that belong to a single disorder realization. In that case the different polymer configurations cannot be assumed independent. If we recall Sec. 3.3.2, we realize that many polymers share a certain part of their configuration which leads to correlations in the final ensemble. Once having found the number of independent configurations, the error can be estimated after Eq. (3.20). For the free polymer, we follow the approach of Higgs and Orland in [93]. They estimated the error for the method used here by assuming that interactions are only between nearest neighbors. As the free polymer model (no disorder) within this work only includes bending energy between neighboring bonds, it fulfills the preconditions of the error estimation by Higgs and Orland. Under this assumption they found the number of independent chains c_{ind} to be proportional to $\mathcal{M}_1/N$, where $\mathcal{M}_1$ is the initial number of chains and N the number of bonds. The variance of the simulation of a free single chain is calculated by applying Eq. (3.20) with σ_{eff}^2 substituted by the variance of the mean value of a single simulation $\tilde{\sigma}_{\overline{\mathcal{O}}}^2$ and $\sigma_{\mathcal{O}}^2$ substituted by the fluctuations of the chains belonging to a single simulation $\tilde{\sigma}_{\mathcal{O}_j}^2$. $\sharp$realizations is substituted by the independent

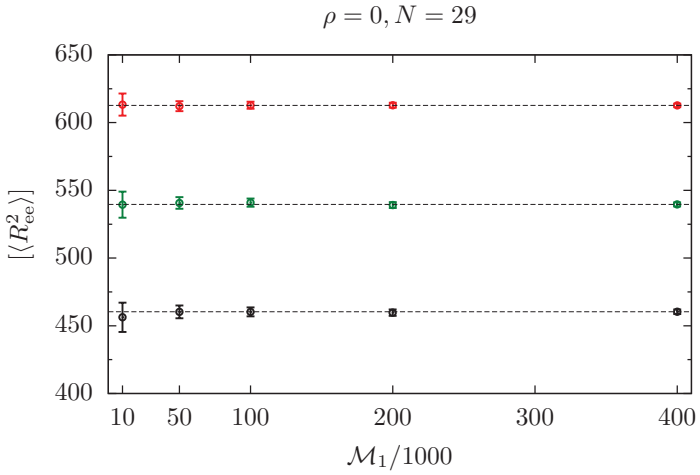

Figure 3.13.: Plot of the mean square end-to-end distances of free semiflexible polymers in dependence on the initial number of chains in units of 1000. The color coding tags different persistence lengths: $\xi = 0.5$ (black), $\xi = 0.7$ (green), and $\xi = 1$ (red), from bottom to top. The error bars are calculated after Eq. (3.21). The horizontal lines are drawn for better visibility.

number of chains which—according to [93]—yields:

$$\tilde{\sigma}^2_{\overline{\mathcal{O}}} \sim \frac{\tilde{\sigma}^2_{\mathcal{O}_j}}{\mathcal{M}_1/N}, \tag{3.21}$$

where $\tilde{\sigma}$ indicates the case of a single simulation without disorder and without quenched average. The error bars are again taken to be the standard deviation calculated from Eq. (3.21). Figure 3.13 shows the mean square end-to-end distance in dependence on $\mathcal{M}_1$ which is the initial number of chains and therefore a measure of the overall number of chains in each growth step (recall Sec. 3.3.2). The relative error for, e.g., 100000 chains is on the order of 1%. If we add disorder, the estimation of the number of uncorrelated configurations becomes more difficult as the narrow channels between neighboring disks, especially for high area fractions, brings about additional correlations. I assessed the necessary number of polymer chains for producing averages in appropriate accuracy by considering the mean values for increasing number of chain configurations. Figure 3.14 shows the mean square end-to-end distance for a polymer exposed to hard-disk disorder for $\rho = 0.5$ and $\rho = 0.7$ as well as different stiffnesses. I examined $\xi = 0.5$, 0.7, and 1. For estimating a good population size, consider, e.g., the long-dashed (green) curve in Fig. 3.14(b) indicated by □. The relative deviations of the mean values for $\mathcal{M}_1 = 50000$ and $\mathcal{M}_1 = 100000$ for this case are about 5% while the relative deviations for $\mathcal{M}_1 = 100000$ and $\mathcal{M}_1 = 400000$ are only about 1%. As the deviations between the latter two are much below the effect of the influence

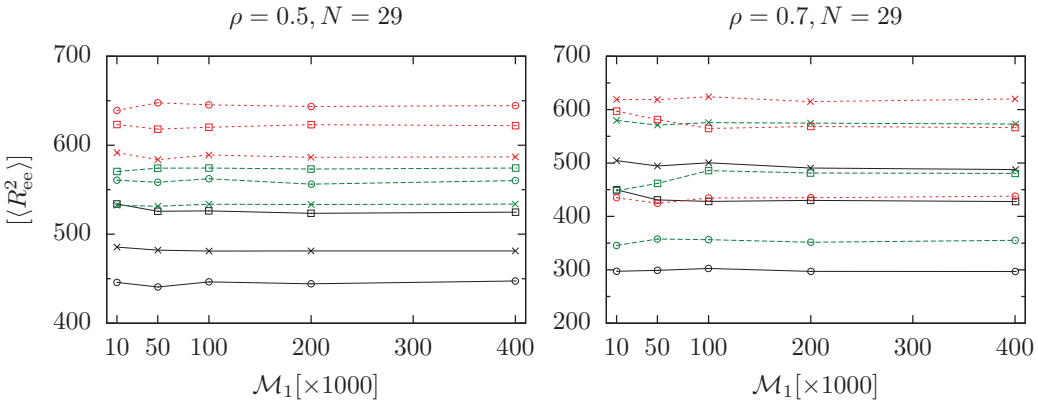

Figure 3.14.: Mean square end-to-end distance of a polymer exposed to a single hard-disk disorder realization with area fraction $\rho = 0.5$ (a) and 0.7 (b) in dependence on the initial number of chains $\mathcal{M}_1$ in units of 1000. The persistence lengths in these examples are $\xi = 0.5$ (—, black), 0.7 (- - -, green), and 1 (- - -, red). The mean values are shown for different disorder configurations indicated by the plot markers.

of the disorder, the accuracy obtained by simulating with $\mathcal{M}_1 = 100000$ is completely satisfactory for the scope of this work.

The above estimation is reassured by a crosscheck with a completely different method—the multicanonical Monte Carlo method. I will comment on this in Sec. 4.

4. Numerical results

The following sections are concerned with the outcome of my numerical simulations of a pinned semiflexible polymer exposed to a disorder landscape of hard disks.

In Sec. 4.1, the considered observables are introduced. The parameters of the numerical simulations are given in Sec. 4.2, which also includes a discussion about the length scales of the system. Section 4.3 shows the results for the free polymer. I compare my findings to literature and discuss the issue of discretization. Section 4.4 is concerned with a polymer exposed to a hard-disk potential with lattice structure, Sec. 4.5 is an examination for the case of hard-disk fluid disorder. Leaving the constraint of pinning the polymers is discussed in Sec. 4.6.

4.1. Observables

Throughout this work I focus on three observables: the end-to-end distribution $P(r)$, the tangent-tangent correlations $\langle \mathbf{t}_i \mathbf{t}_{i+k} \rangle$, and the mean square end-to-end distance $\langle R_{\mathrm{ee}}^2 \rangle(N)$. The end-to-end distribution gives the probability to find a certain end-to-end distance $r = b|\sum_{i=1}^{N} \mathbf{t}_i|$. For a free flexible polymer, the end-to-end distribution function is of the form[9] $P(\widehat{r}) \propto \widehat{r} \times e^{-\widehat{r}^2/2\sigma^2}$, where $\widehat{r} = r/L$ with $L = bN$. The tangent-tangent correlation function $\langle \mathbf{t}_i \mathbf{t}_{i+k} \rangle$ is estimated by averaging

$$\overline{\mathbf{t}_i \mathbf{t}_{i+k}} = \frac{1}{N-k} \sum_{i=1}^{N-k} \mathbf{t}_i \mathbf{t}_{i+k} \tag{4.1}$$

over the population of polymer configurations. The tangent-tangent correlation function is a measure of the stiffness of a polymer. For a completely flexible free polymer there is no energetic preference to any angle and hence there are no correlations between tangent vectors for $k \neq 0$. The case with bending was discussed in Sec. 2.1. The surrounding disorder can lead to both correlations and anti-correlations, as can be seen in Fig. 4.10.

The last observable that I consider is the mean square end-to-end distance in dependence on the polymer length counted in numbers of bonds $\langle R_{\mathrm{ee}}^2 \rangle(N)$. In order to compare to the literature, I consider the mean square end-to-end distance without normalization. For free flexible polymers it grows obviously linearly in N, as the freely jointed chain is nothing but a random walk.

Of course there are more observables that can be considered including the radius of gyration, the gyration tensor, the curvature distribution, etc. The special choice of

[9] $\widehat{r}$ comes from the integration over all directions and $e^{-\widehat{r}^2/2\sigma^2}$ is a Gaussian as the flexible polymer is just a random walk; for the case with bending recall Sec. 2.1.

measured values has to be adapted to the system one wants to compare with. The end-to-end distribution function mirrors the influence of the potential on the spatial extension of the polymer. It gives especially insight into the amount of configurations that are in a certain state, e.g., crumpled or stretched. The tangent-tangent correlation function reflects the mean internal structure of the polymer by measuring the relative orientation of the tangents. It thus provides informations also on short scales of the polymers. The mean square end-to-end distance finally synthesizes the information from a quenched average in one number. Therefore it is well suited for scaling considerations such as the examination of the scaling exponent of the mean square end-to-end distance in dependence on the area fraction ρ.

4.2. Simulation parameters and length scales

4.2.1. Polymer

The polymer determines three length scales of the system. The total length L, the persistence length ℓ_p, and the bond length b. The bond length b is kept fixed throughout this work except for the discussion of the discretization in Sec. 4.3. The discrete polymer model has up to $N+1=50$ monomers. Most of the results are obtained for $N+1=30$ monomers. As stated in Sec. 2.1, the polymer is a phantom chain, i.e., there is no steric self-interaction of the chain (the monomers are considered pointlike).

The total length L and the persistence length ℓ_p are reduced to the ratio $\xi=\ell_p/L$, which is the persistence length measured in units of polymer length L. The persistence lengths considered here include $\xi=0$, representing the flexible case, and $0.1, 0.2, 0.3, 0.5, 0.7, 1$. Specifying the persistence length ξ in units of the total polymer length is the canonical notion for a connection to biophysical problems. From Sec. 2.1, we know that ξ is connected to the coupling constant J via [Eq. (2.11)]:

$$\xi=\frac{\ell_p}{L}=2\frac{J}{Nk_BT}, \tag{4.2}$$

in two dimensions. Equation (4.2) poses a trivial connection between the coupling constant J and the monomer number N via ξ. The stiffness of the polymer is determined by the ratio $K=J/k_BT$. K is thus the natural parameter for the simulations as it sets the scale of the Boltzmann factor. In the analysis of the scaling of the mean square end-to-end distance in dependence on the monomer number N, K is kept fixed.

4.2.2. Disorder

The simulations are done in a square box with periodic boundary conditions. For the case of putting the disks on the sites of a square lattice (cp. Sec. 2.2.1), which will be discussed in Sec. 4.4, the square box is filled with a 20×20 lattice with lattice constant a. The considered site occupation probabilities are $p=0, 0.13, 0.25, 0.38, 0.51, 0.64, 0.76, 0.89, 1.00$. For $\sigma=a$, these densities correspond on average to the area fractions $\rho=0, 0.1, 0.2, 0.3, 0.4, 0.5, 0.6, 0.7, 0.785$, which we will look at for the case of disorder

Table 4.1.: The table shows the connection between the occupation p and the area fraction ρ (two significant digits) in dependence on the disk diameter σ.

p	ρ		
	σ_1	σ_2	σ_3
0	0	0	0
0.13	0.08	0.10	0.11
0.25	0.16	0.20	0.20
0.38	0.24	0.30	0.31
0.51	0.32	0.40	0.42
0.64	0.41	0.50	0.52
0.76	0.48	0.60	0.62
0.89	0.57	0.70	0.73
1	0.64	0.785	0.82

modeled as hard-disk fluid. For lattice disorder, three disk diameters are considered, $\sigma_1 = 0.9a$, $\sigma_2 = a$, and $\sigma_3 = 1.02a$. The reason for the special choice is discussed in Sec. 4.4. Table 4.1 shows the connection between occupation p and area fraction ρ for the different disk diameters σ_i.

The disorder brings another two length scales into play. One it the disk diameter σ, another is the average free distance between the centers of the disks l_0. l_0 is connected to the occupation probability p or the area fraction ρ, respectively, via:

$$l_0 = \frac{a}{\sqrt{p}} = \frac{\sigma}{2}\sqrt{\frac{\pi}{\rho}} \tag{4.3}$$

4.2.3. Putting the two systems together

The length scales of the polymer and those of the disorder are connected via the choice of $a = 5b$ for the case of disorder on the lattice and $\sigma = 5b$ for hard-disk fluid disorder.

An overview over the length scales of polymer and disorder is given in Table 4.2. The top gives the persistence length ℓ_p and the root mean square end-to-end distance $\sqrt{\langle R_{\mathrm{ee}}^2 \rangle}$ in units of σ. The bottom shows the average distance between the centers of the disks l_0 in units of σ. Note that σ for the case of hard-disk fluid disorder corresponds to σ_2 for lattice disorder.

The above choice of parameters allows for a good sample resolution of small size void-space regions bound by the disks of the potential, because the bond length of the polymers is much smaller than the average distance between neighbouring disks. Additionally, stretched polymer configurations reach over the extension of about 6σ. Thus both the behavior of the polymers in small cavities and the behavior of stretched polymer configurations on the scale of several disk diameters can be investigated.

Table 4.2.: Top: Persistence length and root mean square end-to-end distance of a free polymer in units of $\sigma = 5b$ in dependence on ξ. Bottom: Average distance between the centers of the disks for $\sigma = 5b$ in dependence on the area fraction ρ or the occupation probability p, respectively, in units of $\sigma = 5b$.

ξ	0	0.1	0.2	0.3	0.5	0.7	1.0
ℓ_p/σ	0	0.64	1.3	1.9	3.2	4.5	6.4
$\sqrt{\langle R_{ee}^2 \rangle}/\sigma$	1.1	2.7	3.6	4.2	4.9	5.2	5.5

ρ	0.1	0.2	0.3	0.4	0.5	0.6	0.7	(0.785)
p	0.13	0.25	0.38	0.51	0.64	0.76	0.89	1.00
l_0/σ	2.80	1.98	1.62	1.40	1.25	1.14	1.06	1

4.3. The free polymer

The free semiflexible polymer in the form of a discretized or continuous worm-like chain is already widely discussed throughout literature [14, 15, 67, 100, 101, 102]. Here I will just mention some characteristics as the free case will always serve as reference for the case with disorder. Figures 4.1, 4.2, and 4.3 show the three observables

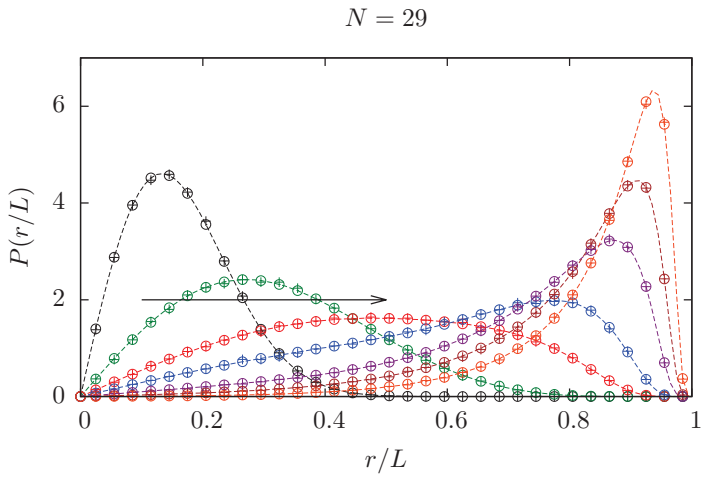

Figure 4.1.: End-to-end distribution functions of free semiflexible polymers. The persistence lengths include $\xi = 0, 0.1, 0.2, 0.3, 0.5.0.7, 1$. The arrow indicates the direction of increasing persistence length. The connecting lines are drawn for better visibility. $\circ$ are data from the growth method; $+$ are Metropolis data.

from Sec. 4.1—the radial distribution function $P(r)$ (Fig. 4.1) the tangent-tangent correlations $\langle \mathbf{t}_i \mathbf{t}_{i+k} \rangle$ (Fig. 4.2) and the mean square end-to-end distance in dependence

on the number of segments N, $\langle R_{\mathrm{ee}}^2 \rangle(N)$ (Fig. 4.3). The distributions are made for $N + 1 = 30$ monomers. The persistence lengths include $\xi = 0, 0.1, 0.2, 0.3, 0.5, 0.7, 1$. The functional form of the end-to-end distribution function $P(r)$ of the free polymer in Fig. 4.1 is characterized by a single peak whose position depends on the stiffness of the polymer. The probability of extended chain configurations increases with increasing stiffness. Hence the peak is shifted to the right for increasing bending energy. A comparison of the data from the growth algorithm with standard Metropolis data yields perfect agreement. The tangent-tangent correlations are shown in Fig. 4.2. They cover the solid lines from Eq. (2.2) perfectly. For the case of no persistence,

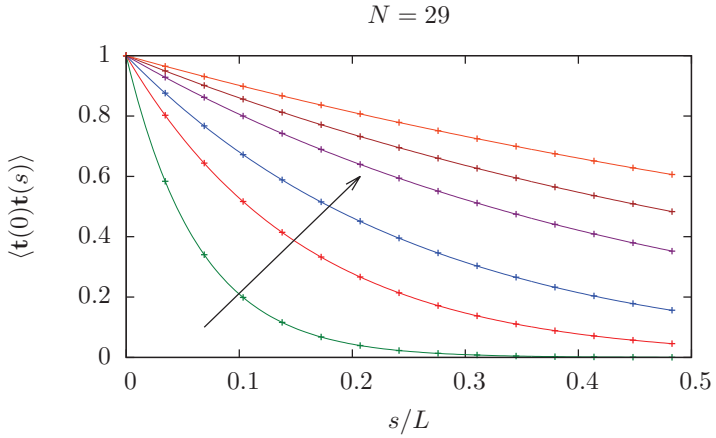

Figure 4.2.: Tangent-tangent correlations of free polymers (ξ as in Fig. 4.1). The solid lines are the analytical solution of the tangent-tangent correlations [Eq. (2.2)]. The trivial case of $\xi = 0$—immediate decorrelation—is not shown.

the tangent-tangent correlation function drops immediately to zero as there is no correlation between the bonds besides the trivial self-correlation at $s = 0$. The scaling of the mean square end-to-end distance [Fig. 4.3; taken from one simulation (recall Sec. 3.3.2)] has two limiting cases. For one thing there is the random walk behavior which I already mentioned above (Sec. 4.1). It is indicated by the lower (green) shading. For another thing, there is a ballistic regime [upper (red) shading] for $N \ll \widetilde{\xi}$, where $\widetilde{\xi}$ indicates the persistence length in units of segments. As long as the number of segments is much smaller than the persistence length, the tangent vectors, and hence the bonds, are almost completely correlated which leads to ballistic [$\langle R_{ee}^2 \rangle(N) \propto N^2$] scaling behavior of the mean square end-to-end distance. While the ballistic limit constitutes a general upper bound for the scaling of the mean square end-to-end distance, the random walk limit is only a lower limit for the free chain. The disorder can reduce the scaling to a constant or even to a decrease of the mean end-to-end distance for increasing number of segments N (see Fig. 4.34).

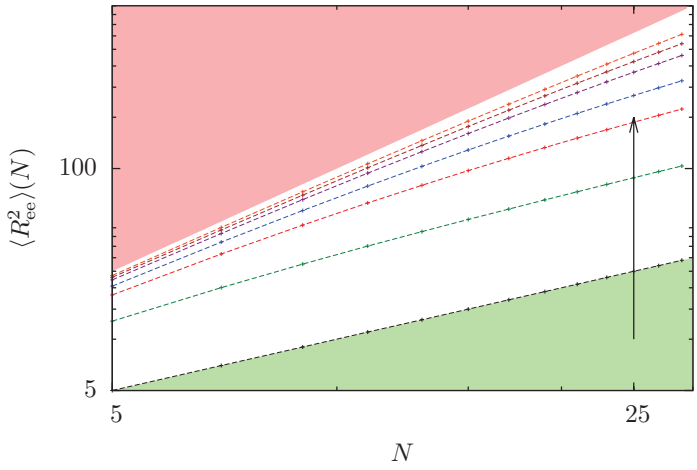

Figure 4.3.: Scaling of the mean square end-to-end distance (no potential, ξ as in Fig. 4.1). The scaling of the axes is log-log. The limiting cases of random walk behavior $\langle R^2_{\mathrm{ee}}\rangle(N) \propto N$ is indicated by the green shading, the ballistic limit $\langle R^2_{\mathrm{ee}}\rangle(N) \propto N^2$ is indicated by the red shading. The arrow indicates the direction of increasing persistence.

Remark on discretization

Figure 4.4 shows the end-to-end distribution function of a free semiflexible polymer. For the case of no persistence $\xi = 0$, the end-to-end distribution is of the form $P(\widehat{r}) \propto \widehat{r}e^{-\widehat{r}^2/2\sigma^2}$, as described above. The number of segments used in this work is enough to approximate the Gaussian sufficiently. For the case of intermediate stiffness $\xi \approx 0.2$, the discretization leads to deviations from the continuous case. $\xi = 0.2$ corresponds to about 6–10 bonds for a total chain length of 30–50 monomers (29–49 bonds). The number of bonds per persistence segment is not sufficient to sample it well enough. 100 monomers (99 bonds) correspond to about 20 bonds per persistence segment. Therefore, the tangent correlations of the discrete model deviate only slightly from the continuous case as can be seen in Figs. 4.4(a) and 4.5. As the maximum number of monomers used throughout this work is 50, we are in a regime where discretization effects for small to intermediate persistence lengths (e.g. $\xi = 0.2$) play a role. The corresponding data for the end-to-end distribution function for 30 monomers are verified by standard Metropolis data. The tangent-tangent correlation function corroborates the above findings. Figure 4.5 shows the tangent-tangent correlation function for a free semiflexible polymer with $\xi = 0.2$. The deviations from the continuous case are shown. In the limit of small b or large βJ, and therefore large N, the continuous case—exponential decay of the tangent-tangent correlations Eqs. (2.8) and (2.10)—is recovered.

If we go to stiffer polymers, e.g. $\xi = 1$, there are about 30–50 bonds per persistence

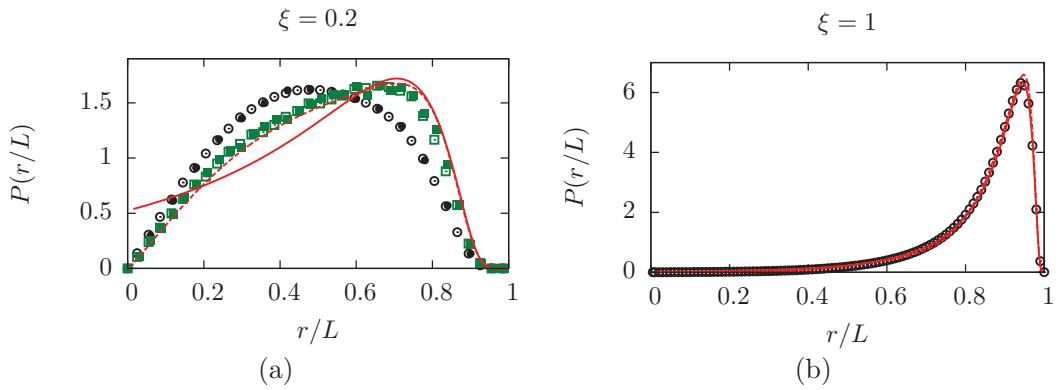

Figure 4.4.: End-to-end distribution function of a free semiflexible polymer. ⊙ (growth algorithm) and • (Metropolis algorithm) for the case of 30 monomers. ⊡ (growth algorithm) and ■ (Metropolis algorithm) for the case of 100 monomers. The dashed line shows the analytical path integral solution by Kleinert *et al.* [67] and the solid line the asymptotic solution in the weakly-bending rod limit by Wilhelm and Frey [15].

segment which is enough to leave discretization effects negligible (see Fig. 4.4(b)).

An increase of the number of bonds N increases the computational effort heavily, especially for a combination of large area fractions ρ along with large persistence lengths ξ. The main effects, however, stay mostly the same.

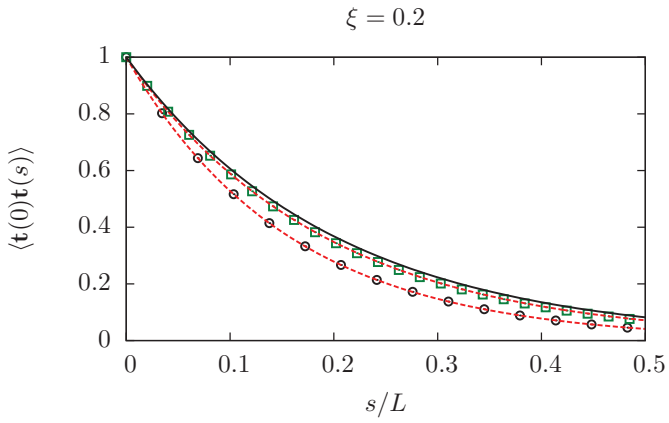

Figure 4.5.: Tangent-tangent correlation function of a free semiflexible polymer. ⊙ for the case of 30 monomers and ⊡ for the case of 100 monomers. The dashed lines show the analytical solution Eq. (2.2) of the tangent-tangent correlations for the discrete case. The solid line shows the analytical solution Eq. (2.8) resp. Eq. (2.10) for the continuous case.

4.4. Lattice disorder

I start off by discussing a polymer exposed to a potential of hard disks distributed on the sites of a square lattice. Such an arrangement allows for good control over the distance between neighboring disks. The parameters can be set up in a way that neighboring disks leave small channels or cavities. We thus can both investigate the influence of subtle structures on the behavior of the polymer and test the algorithm's applicability to potentials that cannot easily be controlled. The channels and cavities of the disorder with lattice structure serve as extreme case for other potentials.

The parameters for the polymer and for the disorder are given in Sec. 4.2. Most of the results of this section are compared to data from a multicanonical Monte Carlo[10] simulation as the growth method has rarely (as far as I know not at all) been applied to the kind of problem investigated here. In the description of the disorder, Sec. 4.2.2, I mentioned that I use three different disk diameters, $\sigma_1 = 0.9a$, $\sigma_2 = a$, and $\sigma_3 = 1.02a$. The lattice constant is $a = 5b$. Looking closely at the parameters, one realizes that for σ_1 there is a channel of half the bond length between neighboring disks [see Fig. 4.6(a)]. For σ_2 [Fig. 4.6(b)], neighboring disks touch each other at one point. As there is no monomer volume and only the monomers may not sit on the disks but not their connecting line, there is a small probability of the polymer to get through the touching point of two neighboring disks. For σ_3 [Fig. 4.6(c)] this is no longer possible as the overlap width of neighboring disks is larger than the bond length of the polymer. The three different cases ($\sigma_{1,2,3}$) constitute a good testbed for putting the growth algorithm to the proof in a high-density disorder landscape. The quenched average smears out the

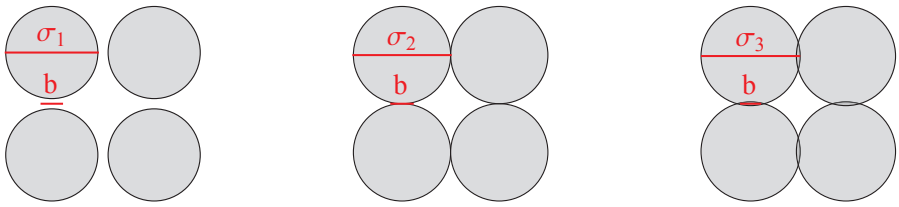

Figure 4.6.: Sketch of the different disk sizes σ_i of the background potential. b is the bond length.

different contributions of the single disorder realizations. Therefore we first focus on a single disorder realization in order to get an idea what principally happens. Both, for the analysis of a single disorder realization and the quenched average, we first explore the flexible case and later on add persistence which brings into play another length scale.

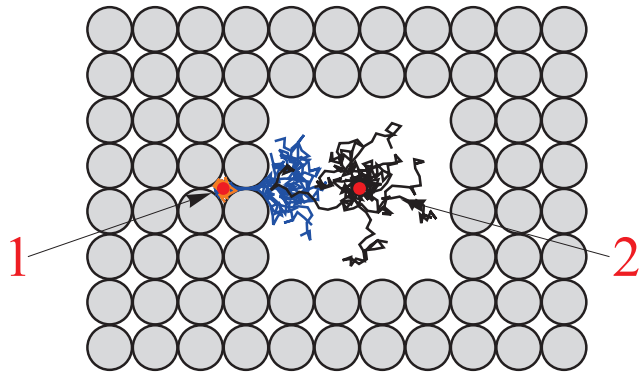

Figure 4.7.: The figure shows a distribution of disks with two exemplary pinpoints for flexible polymers. All sides are continued with disks. The boundary conditions are periodic. Besides, it shows some typical polymer configurations. The orange and blue configurations belong to pinpoint 1 and σ_2. The black ones belong to pinpoint 2 and are representative for configurations that start at pinpoint 2 independent of σ_i.

4.4.1. Single disorder configuration analysis

Figure 4.7 is a showcase of different scenarios that can occur during the disorder averaging. Figure 4.9 and 4.10 show the corresponding end-to-end distribution functions and tangent-tangent correlations. Pinpoint 1 is in a small cavity that is entropically unfavorable for the polymer compared to a larger space such as can be seen around pinpoint 2. As long as the polymer has the chance to explore a larger area by es-

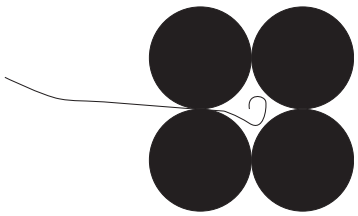

Figure 4.8.: Sketch of a polymer that finds its way through a narrow channel to explore the large space behind it.

caping from a small cavity through a channel, this will happen even if the channel is extremely narrow (Fig. 4.8). The end-to-end distribution $P(r)$ for σ_1 and σ_2 shows this behavior, which is the same for both algorithms—the growth algorithm and the multicanonical Monte Carlo method. It is reflected by the double-peak structure of $P(r)$ in Fig. 4.9. The corresponding curves are the dotted (blue) and the short-dashed (red) and belong to pinpoint 1. The small peak comes from the cavity where the

[10]The multicanonical Monte Carlo data have been generated by Johannes Zierenberg and have been

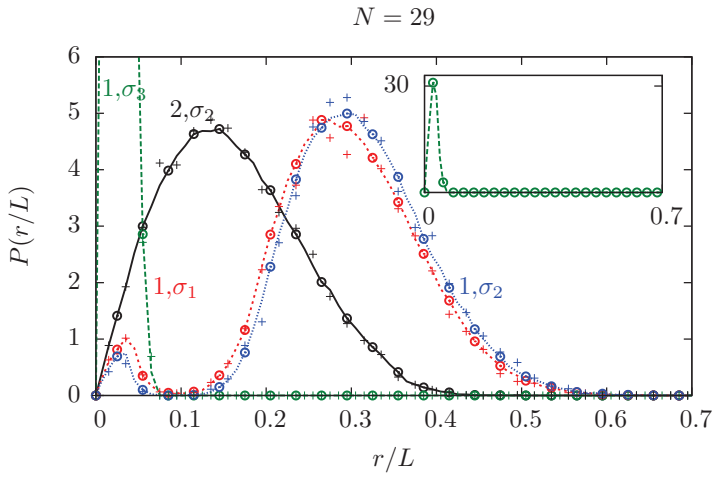

Figure 4.9.: The plot shows the end-to-end distribution functions that correspond to the pinpoints of Fig. 4.7. ∘ shows the data from the growth algorithm; + from the multicanonical simulation. The labeling of the curves is given in the plot (pinpoint, disk diameter). The first number labels the pinpoint, σ_i the disk diameter. The reference case of the free chain is not shown, as it virtually matches the case of pinpoint 2. The connecting lines are drawn for better visibility. The inset shows the full y-range.

polymer is pinned and the big one from the nearby free space region, which is entropically much more favorable. A selection of configurations starting from pinpoint 1 for the case of σ_2 is shown in Fig. 4.7. The orange lines show configurations that stay within the small cavity, the blue ones explore the space behind. For the case of σ_3—no channel left between neighboring disks—the distribution is characterized by a single peak, which corresponds to the exploration of the tiny hole containing pinpoint 1 [this case is marked by the dashed (green) curve which is shown in full y-range in the inset of Fig. 4.9]. The broad single-peaked curve [solid (black)] in Fig. 4.9 belongs to pinpoint 2 and is shown only for σ_2 as the behavior is qualitatively the same for all three disk diameters. The large area around the pinpoint is completely sampled by polymer configurations, leading to a broad end-to-end distribution. Figure 4.10 shows the tangent-tangent correlations for the different pinpoints (the color coding is the same as for Fig. 4.9). While pinpoint 2 leads to quick decorrelation of the tangents, which is characteristic for a free polymer, things are completely different for pinpoint 1. σ_1 and σ_2 show a correlation that is due to the fact that the polymer stretches to the entropically favorable region next to pinpoint 1 through the channel between the disks. This leads to a correlation on short to intermediate lengths along the polymer. For σ_3, where no channels are left, the polymer coils up in the cavity where it is pinned.

published in [51].

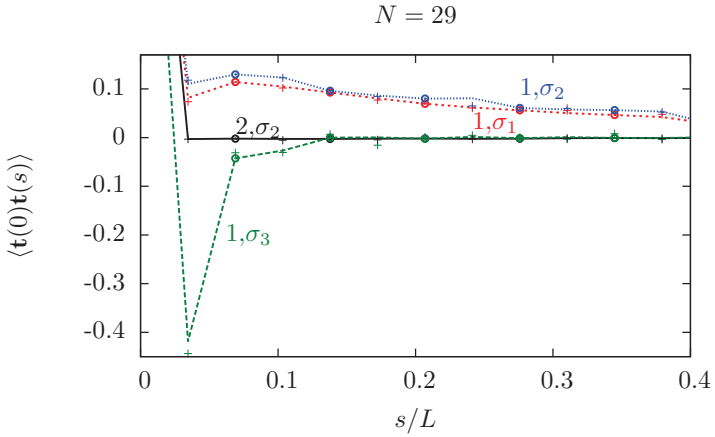

Figure 4.10.: Tangent-tangent correlation functions that correspond to the pinpoints of Fig. 4.7. The line coding is the same as for the end-to-end distributions (Fig. 4.9). The reference case of the free chain is also not shown as it matches the case of pinpoint 2.

This leads to strong anticorrelations on short length scales. For both pinpoints, the two employed simulation algorithms yield consistent results.

Figure 4.11 and the corresponding distributions, Fig. 4.12 and Fig. 4.13, illustrate the case with persistence paradigmatically for $\xi = 0.5$. The case of σ_3 is left out of consideration within the single configuration analysis when persistence is involved because a crumpled configuration that fits in a cavity that belongs to, e.g., pinpoint 1 [see Fig. 4.11(b)] has a vanishingly low probability due to its high bending energy. For now I did not put much effort in investigating this special case. If the monomers of the polymer are no longer considered pointlike, the case of σ_3 can be mapped to a case where the mean distance between neighboring disks of the potential is smaller than the monomer diameter. Therefore the investigation of σ_3 could gain importance. I shortly discuss some results for the case of σ_3 at the end of Sec. 4.4.3 and show data for the quenched disorder average.

The other cases ($\sigma_{1,2}$), on the contrary, exhibit an interesting and rich phenomenology. I start by discussing the issue of pinpoint 1. While the only determining factor for the case without bending energy was entropy, energy gains more and more importance as soon as we start to increase the persistence length. Configurations pinned to pinpoint 1 behave similarly for both σ_1 and σ_2. The gain in entropy by exploring the large free area around pinpoint 2 favors configurations that reach to that space. Going straight through the channel from pinpoint 1 to the free area is even forwarded by the energetic preference for small bending angles. Figures 4.12 and 4.13 point out that both end-to-end distribution function and tangent-tangent correlation function for the case of pinpoint 1 are similar to the free polymer [blue dashed (σ_1) and blue solid (σ_2) lines]. This is reasonable, as the space available for the polymer to spread,

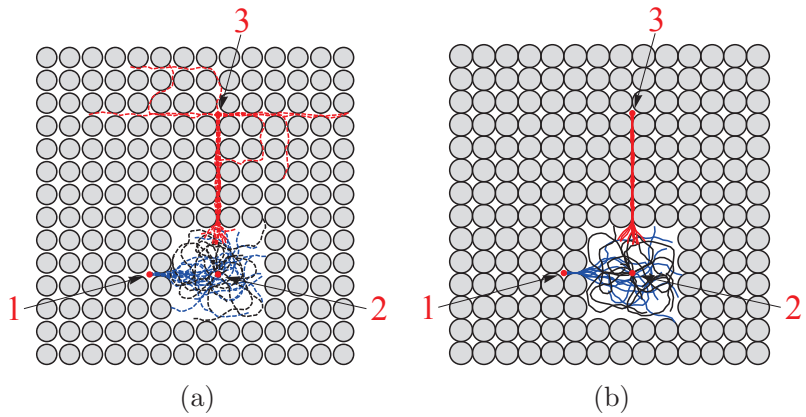

Figure 4.11.: Distributions of disks with three exemplary pinpoints for polymers with $\xi = 0.5$. Additionally, a selection of strongly contributing polymer configurations is shown. All sides are continued with disks. The boundary conditions are periodic. (a) shows the case for σ_1 and (b) for σ_2.

once having passed the narrow channel from pinpoint 1 to the adjacent region, provides entropically similar space as that for a free polymer. Space for bending back is strongly limited by the potential, but as this is energetically not opportune anyway, it does barely affect the equilibrium ensemble. This behavior changes if we move on to configurations starting from pinpoint 2. While this pinpoint provided good preconditions for a flexible polymer to behave as its free counterpart, a polymer with $\xi = 0.5$ and 30 monomers has a mean extension of about $4.4\sigma_2$ [cp. Eq. (2.14)] if not exposed to disorder. The free space in each direction for the case with potential is about $2\sigma_2$ which truncates a large part of configuration space. The difference between σ_1 and σ_2 is small compared to the free volume provided for polymer extension, which suggests a similar behavior for σ_1 and σ_2 and is approved when looking at Figs. 4.12 and 4.13 [black dashed (σ_1) and black solid (σ_2) lines]. While the confinement forces the polymer to crumple up, the energetic cost for bending stretches the polymer out. The interplay of these effects leads to the formation of loops with strong anticorrelations on the length scale of the persistence length, which is half the polymer length (see Fig. 4.13). While configurations starting from pinpoint 1 are similar to the free case, configurations starting from pinpoint 2 are "flexibilized". In contrast, configurations starting from pinpoint 3 show the very reverse—stiffening by disorder. Within the examination of the flexible polymer, I omitted pinpoint 3 as the mean extension of the polymer is too small for a strong gain in entropy in finding the large free area 5σ away. Even for a cavity being only 2σ apart from the large free area, no significant contribution was made by configurations that reached there. The energetic drive to stretch the polymer, however, allows for finding favorable spots even if they are far away. The case σ_1 and σ_2 differ noticeably. σ_2 features only pointlike channels for finding the way from one cavity to another. The large area around pinpoint 2 facili-

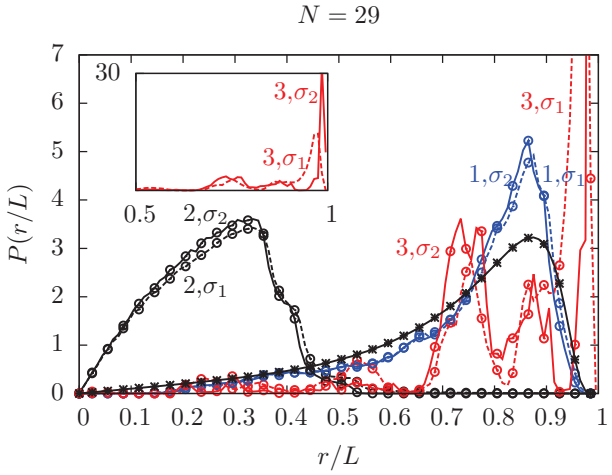

Figure 4.12.: End-to-end distributions that belong to the pinpoints shown in Fig. 4.11 (single simulation; no disorder average). ∘ shows the data from the growth algorithm. The labeling of the curves is given in the plot (pinpoint, disk diameter). The curve marked by × shows the free case with $\xi = 0.5$. The connecting lines are drawn for better visibility. The inset shows the full y-range.

tates a spread of the chain which leads to an entropy gain. Therefore, the equilibrium ensemble is strongly dominated by configurations that end in the large free space. Accordingly, the end-to-end distribution is peaked around almost completely stretched configurations and the bonds are strongly correlated on all lengths, which can be seen in Figs. 4.12 and 4.13 [3, σ_2 (red solid line)]. For the case of σ_1 there is a finite channel between neighboring disks. The additional configuration space provided by the wider channels makes configurations that do not end in the large space around pinpoint 2 contribute stronger than for the case of σ_2. This effect can be seen in the end-to-end distribution function, Fig. 4.12. The corresponding peak at extended configurations is much smaller than that for σ_2 . Also the correlations between bonds decrease faster as can be seen in Fig. 4.13, indicating configurations that are not completely stretched [3, σ_1, (red dashed line)].

Now that we have investigated different scenarios that can occur during the quenched average and thus gained insight into some dominating elements of the quenched average, we move on to averaging over many disorder realizations.

4.4.2. Quenched average for flexible polymers

In analogy to the above case of a single disorder realization, this section discusses results for a polymer without persistence. We take about 1500 disorder realizations for the quenched average. We define the equality of the mean free distance between

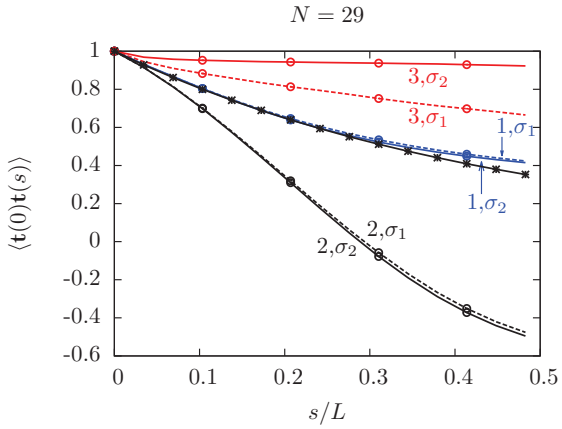

Figure 4.13.: Tangent-tangent correlation functions that belong to the pinpoints shown in Fig. 4.11 (single simulation; no disorder average). ∘ shows the data from the growth algorithm. The free case with $\xi = 0.5$ is labeled by ×. The connecting lines are drawn for better visibility.

neighboring disks and the mean end-to-end distance of the free chain to mark the crossover between a low-density and a high-density regime[11]. The mean free distance was discussed in Sec. 2.3. We described two length scales named r_1 and r_2. r_1 is based upon the distance between neighboring disks with their area being omitted. The area is taken account of by subtracting the disk diameter from the average distance of the centers of the disks. r_2, however, is a measure of the mean free area per disk. At high packing fractions, it gives the area that is left even if r_1 is already zero. For clearness recall Sec. 2.3, in particular Fig. 2.8. We thus take the equality of r_2 and the mean end-to-end distance of the free chain to mark the crossover between low- and high-density regime. Rewriting the average number of disks N in terms of the occupation p and the number of lattice sites M, $N = pM$, r_2 reads:

$$r_2(p) = \sqrt{\frac{A - pM\sigma^2\pi/4}{pM}}. \tag{4.4}$$

with A, p, and σ as described in Secs. 2.2.1 and 4.2.2 and M the number of lattice sites—this is strictly valid only for $\sigma \leq a$, where neighboring disks do not overlap. The occupation p_0 where $r_2(p)$ equals the mean end-to-end distance of the polymer, which is $\sqrt{\langle R_{\mathrm{ee}}^2\rangle} = \sqrt{N}b$ for the free flexible case, marks the crossover

$$p_0 = (a/b)^2 \frac{1}{1 + \frac{\pi}{4}(\sigma/b)^2/N} \frac{1}{N}. \tag{4.5}$$

[11] Further down, I will propose another indicator to mark the crossover between different density regimes. It is based upon the change of the functional form of the characterizing distributions when the area fraction of the potential is increased. This will gain special importance for the case with bending.

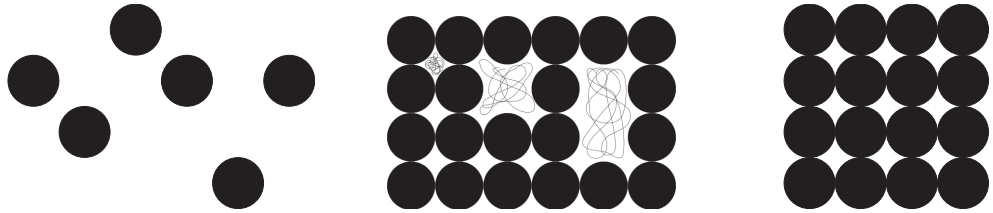

Figure 4.14.: Disorder realizations for increasing density of the background potential from left to right.

For the case considered here ($a = 0.05, b = 0.01, N = 29$), this gives $p_0 \approx 0.56$ for $\sigma = 0.045$ and $p_0 \approx 0.51$ for $\sigma = 0.05$ and $\sigma = 0.051$. Figure 4.15 shows the observables for a freely jointed chain for low densities of the background potential. In this regime ($p \leq p_0$), where the disorder landscape consists of free space and some randomly distributed obstacles [Fig. 4.14(a)], the cases of different disk diameters $\sigma_{1,2,3}$ are similar. The end-to-end distribution [Fig. 4.15(a)] is characterized by a single peak that is shifted to the left and becomes more pronounced for increasing density of the background, which can be interpreted as compression of the polymer by the background potential. The tangent-tangent correlations [Fig. 4.15(b)] show an anti-correlation for increasing density of the background potential, which goes quickly to zero correlation. This is characteristic for the free polymer. The strength of the anti-correlation is one order of magnitude weaker than for the high-density regime. The deviation of the mean square end-to-end distance from the behavior of the free case [dashed line in Fig. 4.15(c)] shows the influence of the potential on the polymer in reducing the space to spread out. The magnitude of the deviation from the free case is again insignificant compared to the high-density case. Computationally, we observe in the low-density regime perfect agreement of the two simulation methods at the level of the line-thickness in Fig. 4.15. If we increase the density, the lattice structure dominates more and more, which leads to a structure consisting of holes of different sizes [Fig. 4.14(b)] that finally ends in a fully occupied lattice where only tiny holes of space are left [Fig. 4.14(c)]. The case of intermediate and high densities ($p > p_0$) is shown in Figs. 4.16, 4.17, and 4.18 for the three observables. The effect of cavities and channels dominates this regime and leads to deviations depending on the choice of the diameter of the disks σ_i.

All three cases ($\sigma_{1,2,3}$) are determined by contributions from configurations where the pinpoint is inside a small cavity and configurations whose pinpoint is in a larger area. For $p = 1$ there finally are only small cavities left. The case of σ_3, where the disks can overlap, is somewhat special. For one thing, the occupation $p = 0.59$ could play an important role, as this is the site percolation threshold of the square lattice. At this point, there is a percolating cluster in one direction which limits the space for chain elongation. Furthermore, a polymer whose pinpoint is inside a cavity cannot escape from it while this is possible for σ_1 and σ_2. This effect can be well observed

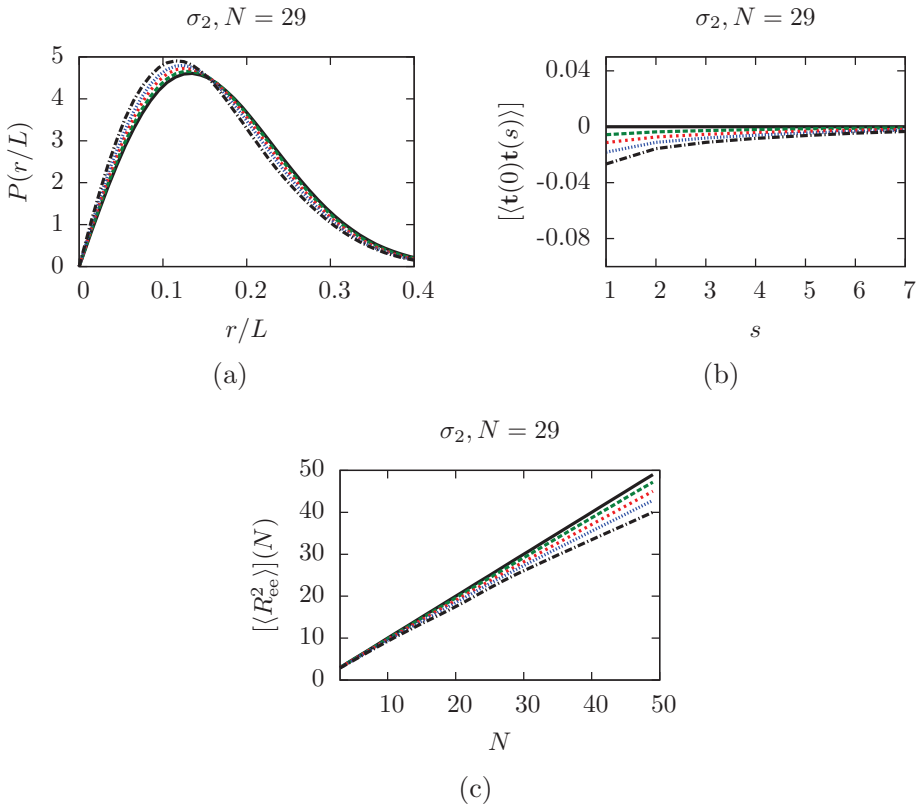

Figure 4.15.: (a) End-to-end distribution function for site occupation $p = 0$ (—, black), 0.13 (– – –, green), 0.25 (····, red), 0.38 (·····, blue), and 0.51 (– · –, black) for increasing peak height. The curves are interpolating lines through the data (whose markers have been omitted for better visibility). The influence of the disk diameter σ_i is negligible in this density regime and chosen here to be σ_2. (b) and (c) are the corresponding plots for the tangent-tangent correlations and the mean square end-to-end distance (in units of squared bond length b^2).

in the distribution of end-to-end distances. For $p = 0.64$ (long-dashed green curve in the plots of Fig. 4.16), σ_1 and σ_2 still show the low-density behavior, which is a single peak shifted to shorter lengths compared to the free polymer. For σ_3, a small bulge next to the main peak can be seen. The position of the bulge in the end-to-end distribution corresponds to an extension of the chain of the order of 1–2 bond lengths, which is the extent of the tiny holes [Fig. 4.14(c)]. For intermediate densities it is very probable that there is a larger free area next to a small cavity. A polymer pinned inside a small cavity thus tries to escape from that region in order to reach the entropically much more favorable space. Consequently, there is no strong contribution

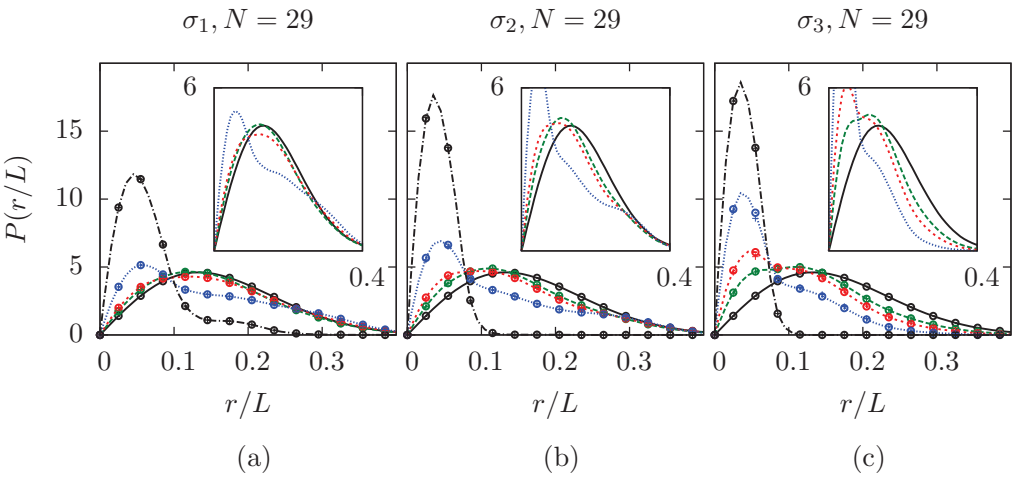

Figure 4.16.: End-to-end distribution function for site occupation $p = 0.64$ (- - -, green), 0.76 (- - -, red), 0.89 (·····, blue), and 1 (— · —, black). The black solid curve is the end-to-end distribution of the free polymer as reference. The data marked by ∘ are from the growth algorithm and + are from the multicanonical algorithm. The different plots are made for $\sigma_{1,2,3}$. The inset shows in each case the regime $p = 0.64, 0.76, 0.89$ (the black solid curve is again the case $p = 0$ as reference), where both the influence of the low-density regime and the influence of the small cavities play a role.

from polymer configurations in small cavities. This is of course different for σ_3. In Footnote 11 I mentioned that the change in the functional form of the distributions will be taken as indicator for the crossover between density regimes. The emerging bulge is such an indicator. I will comment on this further down for the case with persistence. For $p = 0.76$ [short-dashed (red) curves], this effect enters also the case for σ_1 and σ_2 as there is less large space next to cavities. This reduces the gain in entropy when leaving a cavity which is more pronounced for σ_2 as there the channels for escape are much smaller. For $p = 1$, all three cases yield qualitatively the same results again. In this case there is no more benefit in escaping a small cavity, as there are only small cavities left. For the cases of σ_1 and σ_2 the polymer thus mainly stays in the cavities whereas for σ_3 it cannot leave the cavity at all. The tangent-tangent correlations, Fig. 4.17, confirm the findings for the end-to-end distribution. For high densities, the polymer is coiled up in a small region and is therefore in a strongly folded state. This leads to anticorrelations of the tangents on very short length scales which, however, averages out quickly on longer length scales. This effect gains importance with increasing density. A further effect, which is hardly seen in the distributions of Fig. 4.17 as the quenched disorder average combines and thus smears different effects, is a stiffening of the polymer—that is, a positive correlation of bonds—on short length scales for intermediate densities with σ_1 and σ_2. It can well

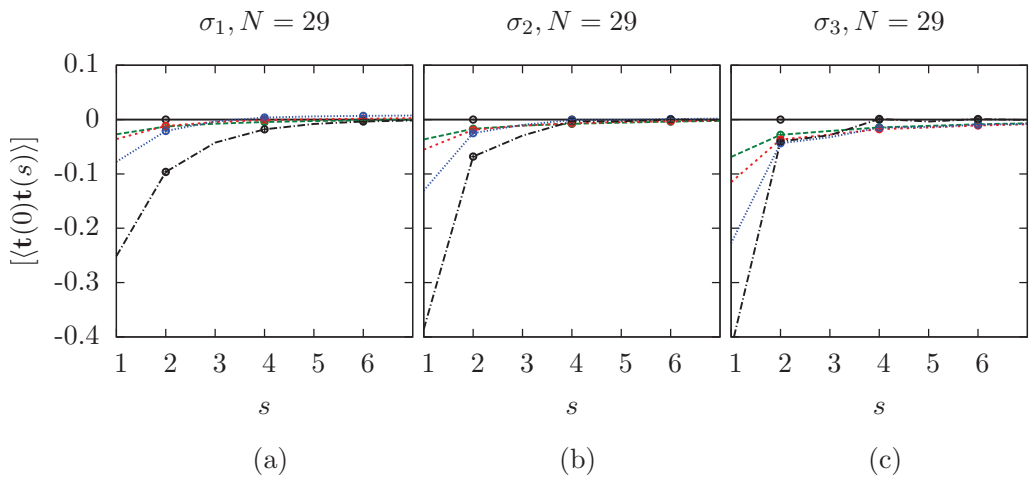

Figure 4.17.: Tangent-tangent correlations for $p = 0.64$ (- - -, green), 0.76 (····, red), 0.89 (·····, blue), and 1 (– · –, black). The black solid curve is for $p = 0$ as reference. The data marked by ∘ are from the growth algorithm and + from the multicanonical algorithm. (a), (b), and (c) differ in the disk diameter. The larger the disk diameter the stronger the anti-correlations on short length scales.

be seen for the single disorder configuration analysis in Fig. 4.10 [short-dashed (red) and dotted (blue) curve] and is already explained there. A polymer that is pinned to a small hole that is next to larger space stretches out to reach the entropically beneficial region leading to the above described positive correlations of tangents. Cates and Ball [26] find similar effects due to energy instead of entropy (tadpole configurations) with pinned polymers.

The last thing to be discussed here is the mean square end-to-end distance in dependence on the number of bonds N, which is shown in Fig. 4.18. The chain-growth algorithm produces results in each step of growth which reduces the computational effort for estimating the scaling of the mean square end-to-end distance. By comparison with the multicanonical method, we found that the potential risk of systematic errors due to correlations of shorter and longer chains can be neglected within our parameter range. For the multicanonical method, the data for each polymer length have to be generated separately. This leads to a higher computational effort in estimating the scaling of the mean square end-to-end distance. For this reason we generated fewer data points for the multicanonical method in Fig. 4.18.

For the intermediate densities in Fig. 4.18, both algorithms again show the same behavior as described above. The surrounding obstacles limit the extension of the polymer. This effect increases for increasing disorder density, which leads to a plateau in the mean square end-to-end distance. This has also been found by Baumgärtner and Muthukumar [33]. This effect dominates for the case of σ_3 where neighboring

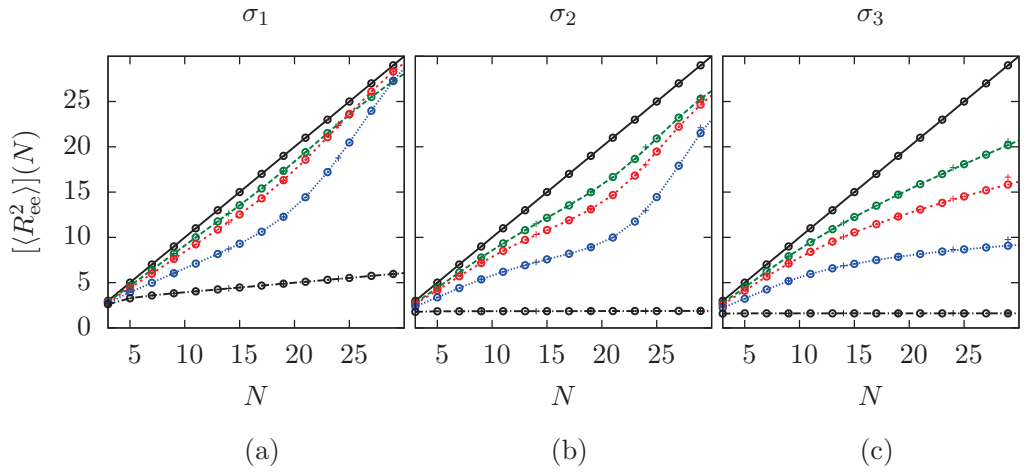

Figure 4.18.: Mean square end-to-end distance (in units of squared bond length b^2) for $p = 0.64$ (- - -, green), 0.76 (· · · ·, red), 0.89 (·····, blue), and 1 (— · —, black) from top to bottom. The data marked by ∘ are from the growth algorithm; + come from the multicanonical algorithm. The black solid curve shows the free polymer case which scales as $[\langle R^2_{ee}\rangle] \propto N$.

disks leave no space for the polymer to escape [Fig. 4.18(c)]. Things are different for the cases of σ_1 and σ_2 [Figs. 4.18(a) and 4.18(b)]. While the first part of the curves shows the same behavior, an increase of the mean square end-to-end distance for increasing number of bonds with a slope $m < 1$, this suddenly changes to a steep slope with $m > 1$. The slope m larger than 1 is due to the reduced angular interval that is available after the polymer has left a small cavity through a narrow channel. Accordingly the polymer is forced in a certain direction, which increases its extension.

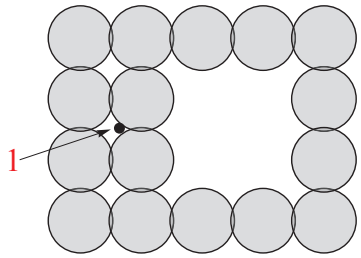

Figure 4.19.: Hard-disk configuration and pinpoint 1 for σ_3. For those cases the multicanonical method hardly converges as it mainly explores the area outside the cavity.

After having described the phenomenology of the problem, I want to comment briefly on the algorithms for the above described problem. For the cases of σ_1 and σ_2 the two algorithms produce fully consistent results. While for shorter chain lengths the two algorithms also agree for σ_3 for high density, they start showing small deviations from each other for $N = 29$, which is barely visible only in Fig. 4.18(c). In analyzing the deviations, we found that this effect increases for increasing chain length. The deviations occur if a pinpoint is in a corner of a small cavity next to a larger free area. The growth algorithm explores the nearby region, building up a dense network of polymers by growing them in parallel. The multicanonical routine, however, explores space by updating an existing configuration, thereby taking into account overlaps with the surrounding disks. Afterwards, these overlapping configurations are calculated out by the reweighting process. In a case as depicted in Fig. 4.19 there are some difficulties with this process. The space for configurations that are allowed is relatively small. As the multicanonical routine is not restricted to the allowed region, the sampling in the allowed region is very rare, which leads to convergence problems for the case of small cavities. The sampling problem of the multicanonical routine becomes even worse as soon as persistence is involved.

The results of the quenched average shown so far are for purely flexible polymers. I compared my findings to the literature and reassured the numerics by comparing with a completely different method. Based upon these findings, I am now going one step further and include an energetic term into the polymer model—the bending term. We will see that the energetic preference for stretched configurations will modify the phenomenology of the problem completely. As already mentioned in Sec. 4.4.1, the special case of overlapping disks (σ_3) is briefly discussed at the end of the next section.

4.4.3. Quenched average for persistent polymers

An estimation of the crossover between a low- and a high-density regime according to the approach for flexible polymers [cp. Eq. (4.5)] turned out to be very imprecise. The reason is, that persistent polymers are more extended in linear shapes, especially for large persistence lengths [see Fig. 4.25(b)].

We will see that the high-density regime is characterized by a multiple peak structure in the end-to-end distribution function. The beginning of this effect shows up as a small bulge in the end-to-end distribution function. Figure 4.20 shows again the end-to-end distribution function of a flexible polymer in hard disk disorder. The solid and dotted (black) curves are in the low density regime. The low-density distributions all have the same functional form which is characterized by a single peak. The dashed (green) one differs from this structure—it has a bulge. The shape of the bulge that emerges as soon as a certain occupation p_0 is crossed can be used as indicator to mark the crossover from a low-density to a high-density regime. Similar effects can be observed for the tangent-tangent correlations. I take the qualitative change of the functional form of the end-to-end distribution—formation of double/multiple peak structure—as a qualitative signal for the crossover from a low- to a high-density regime.

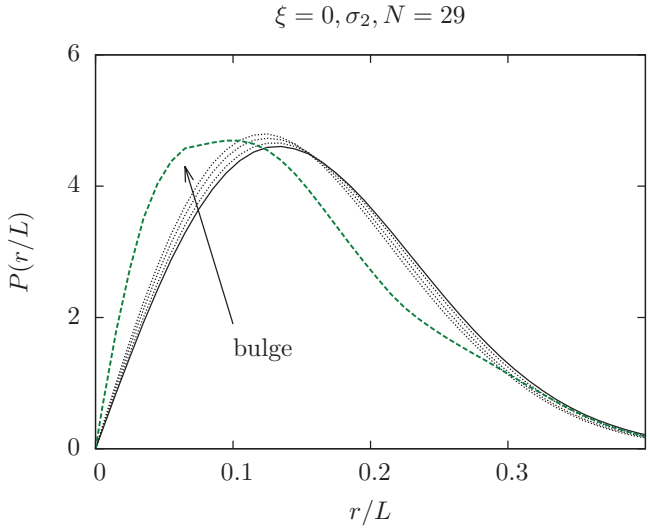

Figure 4.20.: End-to-end distribution function for the case of no persistence. The black (solid and dotted) curves are in the low density regime. The high-density regime, labeled by the long-dashed (green) curve, is indicated by a deviation of the functional form from the $p = 0$ (black solid) case.

Low-density regime

In the following, we examine the low-density regime for different persistence lengths. Figure 4.21 shows the end-to-end distribution function for increasing persistence (growing ξ indicated by the arrow). The occupation probabilities in the plot are $p = 0, 0.13, 0.25, 0.38, 0.51$ and the disk diameter is chosen to be σ_1. Therefore the occupation probabilities correspond to an average distance between the disks of $l_0 \geq 1.5\sigma_1$ [cp. Eq. (4.3)]. The low-density regime is identical for σ_1 and σ_2 except for the case of $p = 0.51$ which shows low-density characteristics for σ_1 whereas σ_2 starts to exhibit deviations from the low-density regime. We find two kinds of response to the disorder depending on the stiffness of the polymer—compression and extension. The probability for shorter end-to-end distances is growing for increasing occupation p at low persistence length $\xi \leq 0.2$ corresponding to $\ell_p \leq 1.3\sigma_1$ which is less than the smallest average mean distance $l_0 = 1.5\sigma_1$ within this density regime. The reverse is observed for $\xi \geq 0.5$ which corresponds to $\ell_p \geq 3.2\sigma_1$ which is more than the largest average distance $l_0 = 3.1\sigma_1$ (except for $p = 0$) in the low-density regime (the effect of stiffening is hardly seen in Fig. 4.21). If we look at the zoomed regions of Fig. 4.21, we find that the stiffening declines with higher persistence lengths. The findings are approved by the tangent-tangent correlations, Fig. 4.22, and the scaling of the mean square end-to-end distance, Fig. 4.23. The variation in the stiffness can be seen in a faster decay (softening) or slower decay (stiffening), respectively, of the tangent-tangent correlations. In Sec. 2.1.1, I described the properties of the discrete worm-like chain model.

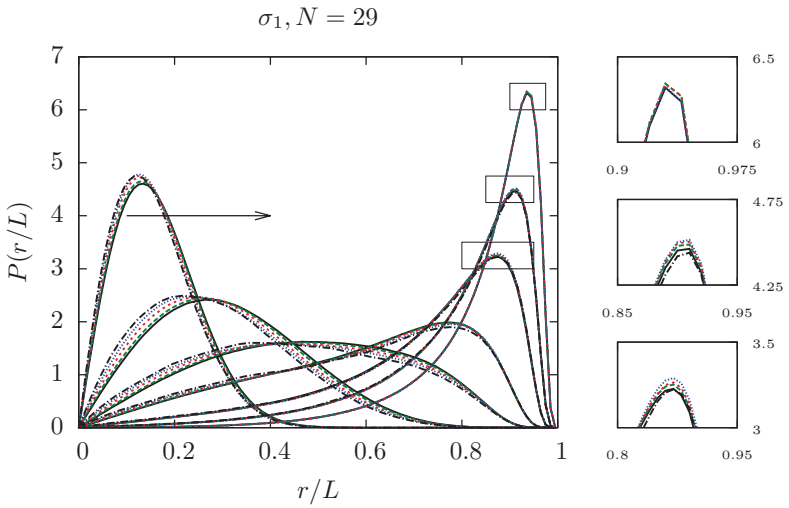

Figure 4.21.: The end-to-end distribution of a polymer exhibits different response to an increasing occupation probability p depending on the persistence length. The persistence lengths include $\xi = 0, 0.1, 0.2, 0.3, 0.5, 0.7, 1$ (from left to right indicated by the arrow). The occupation probabilities are $p = 0$ (—, black), 0.13 (- -, green), 0.25 (···, red), 0.38 (·····, blue), and 0.51 (-·-, black). The extra plots are enlargements of the corresponding boxes in the main plot.

A crucial property is the functional form of the tangent-tangent correlations, Eq. (2.2). The solid lines in Fig. 4.24 (semi-log scaling) are fits of Eq. (2.2) to the data which confirm that the WLC characteristics remains in the low-density regime. The mean square extension in dependence on the segment number N is depicted in Fig. 4.23. The compression of the polymers can be well observed for small persistence lengths. For larger persistence length, the stiffening can hardly be seen.

For an explanation of the softening and stiffening at different persistence lengths consider Fig. 4.25. The case of small persistence lengths is shown on the left, Fig. 4.25(a). The energetic cost for bending is in a range where it is more favorable for the polymer to crumple up in order to gain entropy than to stretch. This is different for stiffer polymers. The probability for bending decreases exponentially with increasing persistence. That is why configurations are favored that find tube-like free regions. The width of thermal fluctuations of those configurations is limited by the distance between neighboring disks [Fig 4.25(b)]. The squared width of the fluctuations is related to the persistence length via (refer to, e.g., [103]):

$$\frac{\delta r_\perp^2}{L^2} \propto \frac{1}{\xi}, \tag{4.6}$$

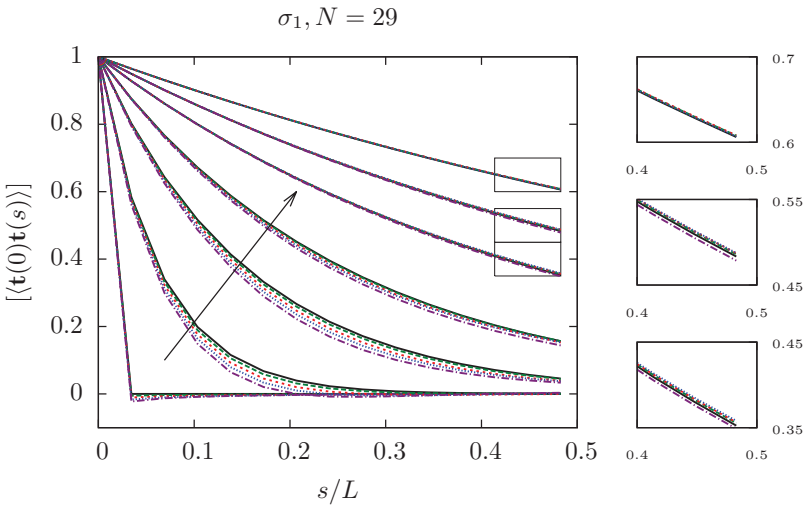

Figure 4.22.: Tangent-tangent correlations for the same parameters as in Fig. 4.21: $\xi = 0, 0.1, 0.2, 0.3, 0.5, 0.7, 1$ (growing persistence indicated by the arrow), $p = 0$ (—, black), 0.13 (- - -, green), 0.25 (- - -, red), 0.38 (·····, blue), and 0.51 (– · –, black). The extra plots are enlargements of the corresponding boxes in the main plot.

i.e., it decreases for increasing persistence length. Therefore the effect of stiffening lessens and finally vanishes for stiff polymers in the low-density regime.

The difference between different disk diameters σ becomes negligible in the low-density regime. The important describing quantity is the area fraction ρ and not the occupation probability p. The low-density regime is mainly determined by the area that is available for the polymer that differs for equal p but different disk diameters σ (compare Table 4.1). We will see later on in Sec. 4.5 that the low-density behavior is the same also for other structures of the background potential—in the subsequent case of a hard-disk fluid.

High-density regime

We now turn over to the high-density regime with $p \geq 0.64$ (which is above the percolation threshold $p_c = 0.5927$) where the shape of the distributions starts to exhibit characteristics of the potential up to the point where the potential completely dominates the distributions. This means that the confinement increases in such a way that the polymer either has to crumple up even though this is connected to high cost in energy or has to stretch at the expense of entropy.

I consider the effect of high-density disorder for three exemplary persistence lengths, $\xi = 0.1$, $\xi = 0.3$, and 1. $\xi = 0.1$ represents a quite flexible polymer that can well adapt

to the surrounding disorder by crumpling up. $\xi = 1$ is rather stiff with respect to the disorder and adapting to confinement by crumpling is only feasible at high energetic cost. In this case, adapting is mostly done by stretching. $\xi = 0.3$ is in between and exhibits both, crumpling and stretching. The discussion is made in parallel for σ_1 and σ_2. The latter has to be understood as limiting case. Especially for the combination of high occupation p and large persistence ξ, it was hard—for some cases impossible—to sample space to an extent that would allow for high accuracy statements. In contrast to the low-density region, the distributions in the high-density regime feature a variety of peaks. The periodic structure of the lattice is mirrored in the observables that characterize the polymers.

Small persistence length The end-to-end distribution for $\xi = 0.1$ in the high-density regime is shown in Fig. 4.26. A good impression of what is going on can be grasped from Fig. 4.35 (shown at the end of this section). As long as the persistence length is of the order of the extension of the available space, the polymer crumples up close to its pinpoint. The persistence length $\xi = 0.1$ corresponds to three bonds. This is of the order of the extension of the smallest cavities (like those around pinpoint 1 in Fig. 4.19; I call them $\diamond$-cavities as they are shaped like a diamond $\diamond$). Figure 4.27(a) illustrates this situation. Crumpled configurations are reflected in the contributions to small extensions in the end-to-end distribution function [Figs. 4.26(a) and (b) second row]. The peaks in the end-to-end distribution become more pronounced with increasing occupation probability p. Some configurations (the fraction of those increases with increasing p) will extend to neighboring regions once the energetic penalty for bending

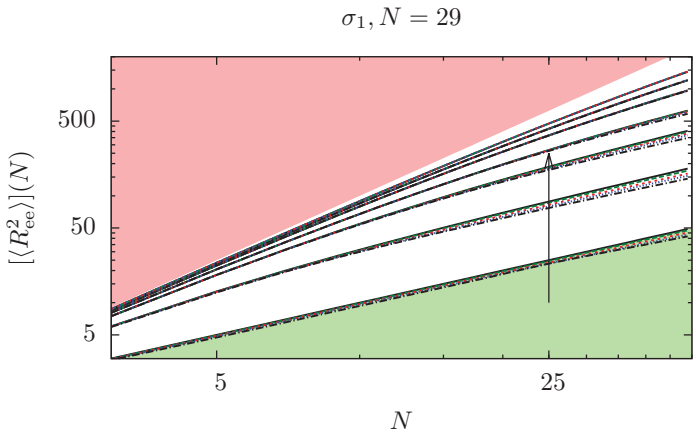

Figure 4.23.: Log-log plot of the mean square end-to-end distance in the low-density regime: $\xi = 0, 0.1, 0.2, 0.3, 0.5, 0.7, 1$ (growing persistence is indicated by the arrow), $p = 0$ (—, black), 0.13 (- - -, green), 0.25 (- - -, red), 0.38 (·····, blue), and 0.51 (– · –, black). The limiting cases, random walk (green) and ballistic regime (red), are shown at the bottom and top, respectively.

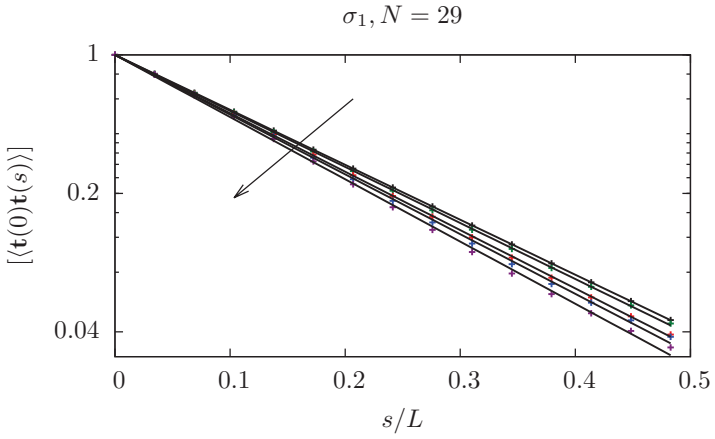

Figure 4.24.: Tangent-tangent correlations in semi-log scale. $\xi = 0.2$. The arrow indicates increasing occupation probability $p = 0, \ldots, 0.51$. The solid lines are fits of Eq. (2.2) to the data.

becomes too large. For the case of a pointlike channel (σ_2), the crossing point acts like a new starting point. This can be seen in the periodic structure of the end-to-end distribution.

As soon as the $\diamond$-cavities contribute the dominant part to the starting points, especially for the case of $p = 1$, the peaks in the end-to-end distribution function can directly be ascribed to the periodic structure of the lattice. Figure 4.28 shows the different length scales that mainly determine the extension of the polymer in this case. Large clusters do not play a role in this regime (cp. Sec. 2.2.1). The polymer, starting at one point, will either stay near the region where it started or extend through a channel to a neighboring or next-nearest neighboring, etc., free region. The first

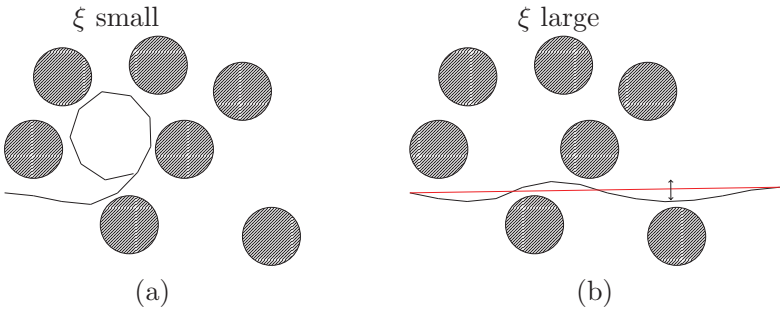

Figure 4.25.: Sketch to elucidate the idea of softening and stiffening for persistent polymers in a low-density background potential. The double-headed arrow indicates the width of the thermal fluctuations of the polymer.

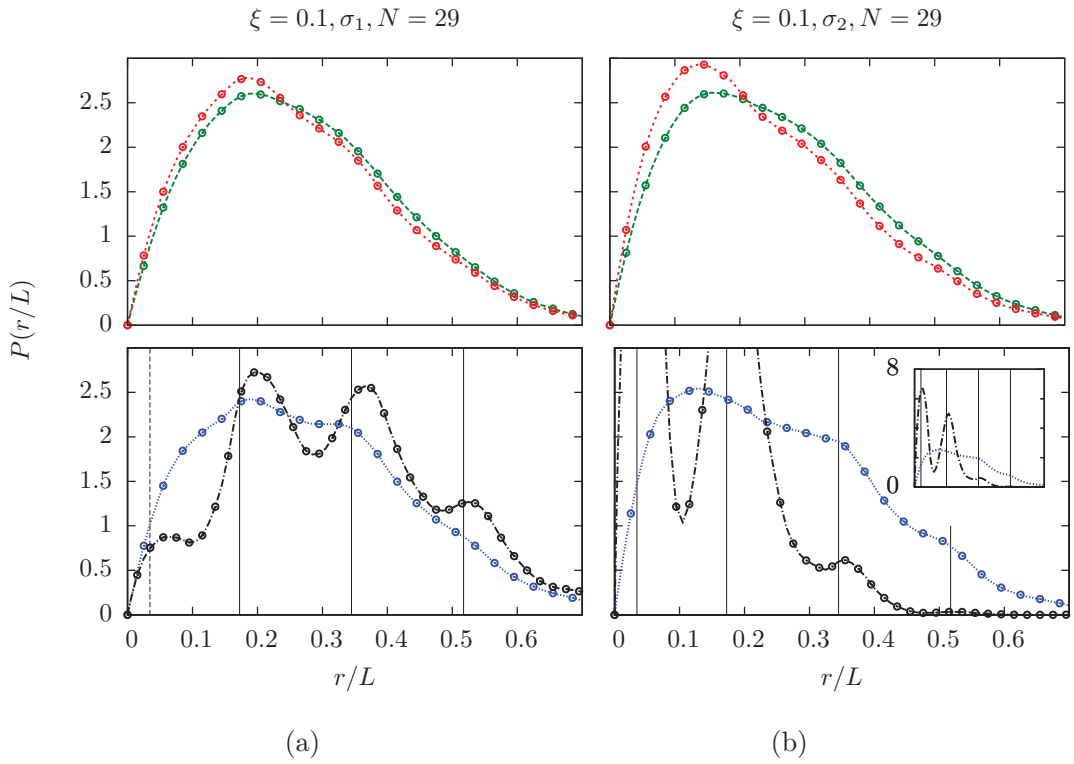

Figure 4.26.: End-to-end distribution function for $\xi = 0.1$. The occupation probabilities are: $p = 0.64$ (- - -, green), 0.76 (- - -, red), 0.89 (·····, blue), and 1 (— — —, black). The vertical lines correspond to the distances shown in Fig. 4.28. The different densities are split up into two plots (upper and lower row) for better visibility.

distance, indicated by the short-dashed vertical line in Fig. 4.28, plays a role for very high occupation probabilities ($p = 0.89, 1$), as most of the chains will start in a small cavity. The lines of Fig. 4.28 are sketched in Fig. 4.26. The dotted lines (arrows) play a subordinate role and are therefore omitted in the plots. The reason is that a polymer that moves on to a neighboring cavity instead of staying in the current one has lower energy if it goes straight, which is not the case for the cavities indicated by the arrows. Their role becomes even less important with increasing bending stiffness. The difference between σ_1 (finite channel) and σ_2 (pointlike channel) can clearly be seen in Figs 4.26(a) and (b). While moving on to cavities that are further apart is easily possible in the case of σ_1, this is only feasible at very high cost in entropy for σ_2. Therefore most configurations will be in the cavity where the polymer is pinned to and in the neighboring ones. Besides, the finite channels in the case of σ_1 blurs the curves (due to larger configuration space) such that the distances of Fig. 4.28 do not perfectly match.

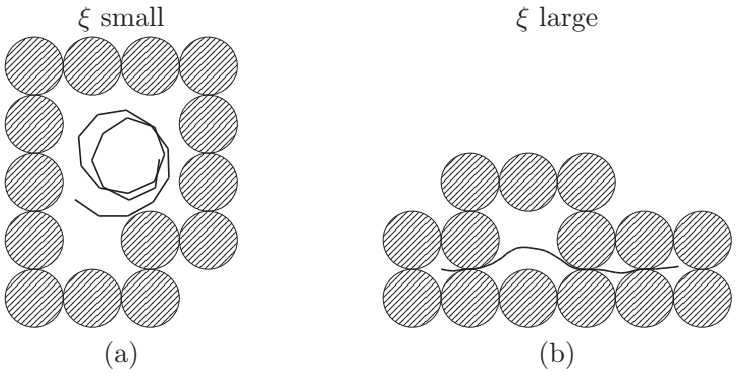

Figure 4.27.: The sketch on the left shows the situation of a rather flexible polymer confined by disks. The width of the confinement is larger than the persistence length of the polymer. On the right hand side, the polymer is much stiffer. In both situations, the length scale of the polymer is 'compatible' with the length scale of the potential.

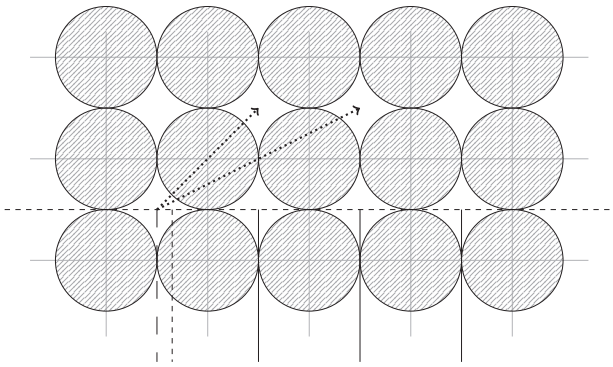

Figure 4.28.: Section of a lattice. The part shown here is fully occupied, which is just exemplary. The long-dashed vertical line (left most) is a reference line. The other lines and arrows show different distances on the lattice. The short-dashed vertical line stands for the mean extension in a small cavity. The next vertical line depicts the distance a lattice constant a apart, the next $2a$, and so on.

Large persistence length Next we are looking at the stiff counterpart. Figure 4.30 shows the case for $\xi = 1$, which is a typical representative of semiflexible polymers [cp. Eq. (2.13)], where bending on the length scale of a few bonds is punished by high energetic cost. The end-to-end distribution function for $\xi = 1$ also exhibits the periodic structure which is preset by the structure of the potential. It is, however, much less pronounced and most of the contributions stem from extended chains. Figure 4.27(b) is an illustration of a polymer with a persistence length that is larger

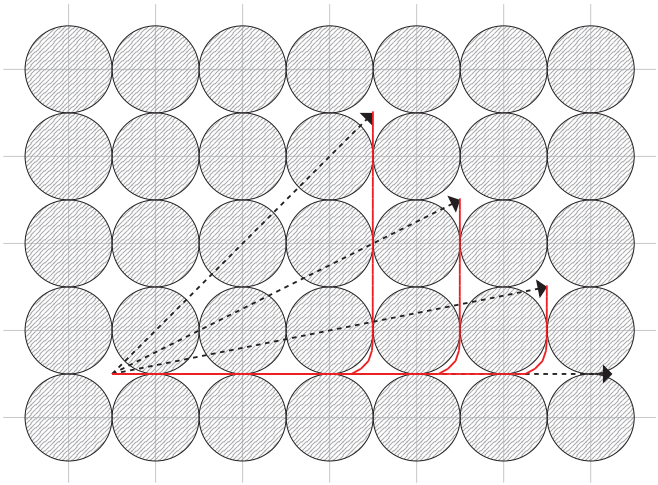

Figure 4.29.: Section of a fully occupied lattice (exemplary). The horizontal arrow indicates the end-to-end distance of fully stretched polymers which are prevailing for large p and ξ. The other arrows are end-to-end distances to cavities that are reached by polymers with one 90° turn. Three of them are indicated by the dashed (red) lines.

than the average void-space cluster size. Some configurations will still crumple up in small clusters, which, however, make only a vanishingly small contribution. Extended chains contribute the most part. Figure 4.27(b) shows a rather extended configuration. Some end-to-end length is stored in a cluster of size one in an undulation. As soon as the lattice is fully occupied, the width of the transverse fluctuations are strongly suppressed. Additionally, the polymer behaves like a stiff rod on the length scale of the $\diamond$-cavities. Accordingly, extended configurations prevail in this regime and the end-to-end distribution function is dominated by a single peak near one. The only additional significant contributions stem from configurations with one 90° turn. The end-to-end distances belonging to those configurations are sketched in Fig. 4.29. They can also well be observed in Fig. 4.35(b) for $\xi = 1$. The distances belonging to these configurations are indicated in Fig. 4.30. The cases for σ_1 and σ_2 look very similar. For the fully occupied lattice, changing the direction is easier for the case of σ_1, as the broader channel leaves more space for different configurations. Additionally, the data belonging to σ_2, especially for the case of high p and ξ have to be taken with care. For this limiting case, both algorithms, the growth algorithm and the multicanonical Monte Carlo method had difficulties in sampling. This problem is exemplarily illustrated in the appendix, Sec. A. Figure A.4 shows the data from the growth method on the left and data from the multicanonical method on the right. A close look reveals the problem. Even though the starting point is in the middle of a small cavity, sampling is not symmetrical. Some channels have even not been sampled by a single configuration in the case on the right even though the statistical accuracy has been extremely raised

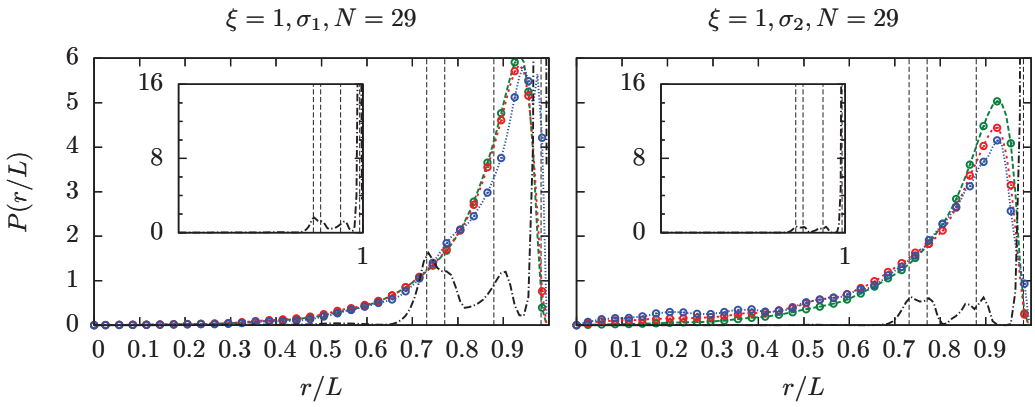

Figure 4.30.: End-to-end distribution function for $\xi = 1$, σ_1 (a), σ_2 (b). The occupation probabilities are: $p = 0.64$ (- - -, green), 0.76 (· · · ·, red), 0.89 (·····, blue), and 1 (— · —, black). The vertical lines correspond to the distances shown in Fig. 4.29.

for these pictures.

Crossover The end-to-end distribution function for the intermediate stiffness with $\xi = 0.3$ is shown in Fig. 4.31. The free polymer, indicated by the black solid line in Fig. 4.31 (first row), has a peak at quite extended configurations. While the basic structure of the end-to-end distribution stays the same for σ_1 for increasing p [Fig. 4.31(a)] (except for $p = 1$), the curves for σ_2 deviate strongly from the free chain distribution. The curve for $p = 0.64$ and σ_2 still has the main peak on the right. This changes for $p = 0.76$. At $p = 0.89$, the main peak is clearly on the left. Hence, $\xi = 0.3$ features a transition from extended to crumpled configurations, additionally exhibiting the periodic structure which is preset by the lattice. The persistence length is on the order of the average extension of the clusters of void space. Therefore the polymers tend to be extended and leave the clusters. This is easily possible for the case of finite channels (σ_1), Fig. 4.31(a). For pointlike channels, the entropic penalty for going through a channel is larger then the energetic benefit in stretching. This is different for $\xi = 1$. As soon as the cluster size becomes too small ($p = 1$), this suddenly changes as crumpling is punished by high energetic cost. The persistence length counted in numbers of bonds is about 9, which is larger than the extension of the $\diamond$-cavities. Stretching is promoted by energy and by the channel structure of the potential. On the other hand, the confinement, especially the channel structure at $p = 1$, reduces configuration space thus being unfavorable with respect to entropy.

The transition from $\xi = 0.1$, which is rather flexible, to the quite stiff case of $\xi = 1$ via the intermediate stiffness of $\xi = 0.3$ is well seen for $p = 1$. While $\xi = 0.1$ has no

contributions to extended chains and $\xi = 1$ has none to coiled configurations, $\xi = 0.3$ has both (cp. Fig. 4.26, Fig. 4.30, and Fig. 4.31). The distances of Fig. 4.28 and Fig. 4.29 are sketched for $\xi = 0.3$ (bottom of Fig. 4.31). The lines do not match as nicely as in the case of $\xi = 1$ because a smaller persistence length allows larger amplitudes of undulations and hence smaller end-to-end distances.

The end-to-end distribution functions for other persistence lengths are presented and summarized in Fig. 4.32. σ_1 is marked by the black solid lines, σ_2 by the red dashed lines. I will not go into the details of the various cases shown in Fig. 4.32 as they are a composition of the effects that contribute to the rather flexible case of $\xi = 0.1$ and the much stiffer case of $\xi = 1$ as we have seen for $\xi = 0.3$. An example is the situation in the third row and fourth column of Fig. 4.32 which belongs to

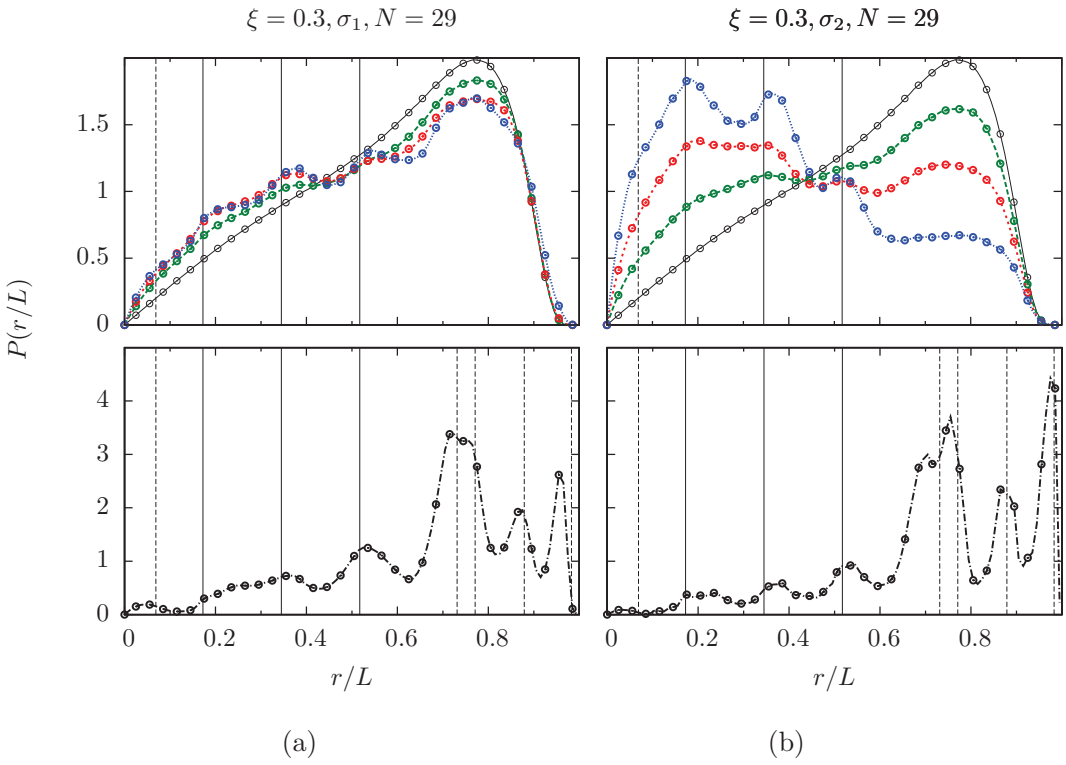

Figure 4.31.: End-to-end distribution function for $\xi = 0.3$. The left column (a) is for σ_1, the right (b), for σ_2. The occupation probabilities are: $p = 0$ (—, black), $p = 0.64$ (– –, green), 0.76 (···, red), 0.89 (·····, blue), and 1 (– ·–, black). The vertical lines left of $r/L = 0.6$ correspond to the distances shown in Fig. 4.28, the lines on the right to Fig. 4.29. The different densities are split up into two plots (upper and lower row) for better visibility.

$\xi = 0.5$ and $p = 0.89$ for σ_2 [dashed (red) line]. While the fairly flexible case on the left of it gathers most of the probability at short end-to-end distances where bending is possible at a lower energetic penalty, the case to the right congregates it at more extended configurations where bending is strongly punished. The case in between (third row and fourth column, $\xi = 0.5$) is on an intermediate energy scale which is reflected in a more undulating distribution with peaks of similar height.

In the above discussion we considered fixed persistence ξ for increasing occupation p. Another approach would be to take fixed occupation p and increase the persistence length ξ. This resembles the approach of Cifra [45] and is done in Fig. 4.35 for σ_1 from top to bottom. The left and right column are sections from disorder realizations belonging to different occupation probabilities. The left (a) belongs to $p = 0.89$ and the right (b) belongs to $p = 1$. It is nicely seen that as soon as the persistence length exceeds the extension of the free space, the polymers propagate to neighboring void space. This can also nicely be seen by considering Fig. 4.32 from left to right (at constant p).

The analogue to Fig. 4.32 for the tangent-tangent correlations is given in Fig. 4.33. A small persistence length in combination with a high occupation p leads to quick decorrelation or even anticorrelations of the tangent vectors (e.g. fourth row second column, $\xi = 0.1$ and $p = 1$). Large persistence and strong confinement, however, leads to the opposite, that is strong correlations even for large distance of the tangent vectors (compare $\xi = 1$ and $p = 1$). This is of course only true for the cases considered so far, i.e., where the disorder includes channels between neighboring disks. The scaling of the mean square end-to-end distance is given in Fig. 4.34 in log-log scaling. The effect of the disorder is more pronounced for the case of σ_2, Fig. 4.34(b), as the channels are much narrower than for the case of σ_1. Especially for the case of $\xi = 0.1$, the differences between σ_1 and σ_2 can be seen by considering the mean square end-to-end distance for the fully occupied lattice, $p = 1$. The finite channels (σ_1) lead to stronger extension of the polymer in comparison with the free chain (black solid line), whereas the pointlike channels (σ_2) lead to compression when compared to the free polymer. The structural details of the mean square end-to-end distance are better seen in Fig. A.3 given in the appendix, Sec. A, where the data are plotted in linear scaling. The data range there is extended to $N + 1 = 50$ monomers.

Data for $N + 1 = 50$ monomers are presented in the appendix, Sec. A. Figure A.1 is an overview over the end-to-end distributions for $N + 1 = 50$ monomers and Fig. A.2 is the corresponding overview over the tangent-tangent correlations.

Leaving the channels Before I conclude this section, I want to mention the case of σ_3. In the overview over the end-to-end distributions (Fig. 4.32) and the tangent-tangent correlations (Fig. 4.33), the data for σ_3 are included (green large-dashed curves). The disorder average comprises contributions from different starting points. For σ_1 and σ_2, polymers that start in a certain cluster can extend to nearby clusters (the starting point is fixed, but the rest of the polymer can enter neighboring regions) through the channels between neighboring disks. This is no longer possible for σ_3. The different contributions from, e.g., $\diamond$-clusters and larger clusters can clearly be differen-

tiated in the distribution functions as soon as the persistence length is larger than the extension of the void space. Here, this is the case as soon as the $\diamond$-cavities play a role. They are identified by the sharp peak around 0.1. The fully occupied lattice exhibits no difference between σ_2 and σ_3 for $\xi = 0$. The lack of an energetic preference for extended configurations and the entropic decrease for entering a neighboring region by going into a nearby $\diamond$-cavity, makes the polymer stay in the void space where it is pinned to even though it could traverse a pointlike channel.

As soon as bent configurations are energetically punished, the distributions for σ_2 and σ_3 deviate significantly from one another. While the distributions of σ_1 and σ_2 converge for the fully occupied lattice and increasing persistence, they depart more and more from σ_3. The reason is the disagreement of the confinement and the constraints of the polymer to favor extended configurations for the case of σ_3. The caged polymer has to crumple up in the region where it is pinned to. The urge to be extended for large persistence is reflected in the periodic structure of the tangent-tangent correlations [e.g. 4th row 5th column in Fig. 4.33 (green long-dashed curve)]. The polymer is extended on the length scale of the void space. Thus it has the structure of a chain of links that are completely folded up. Several bonds constitute a link. On the length scale of the links, the polymer shows periodic correlations and anticorrelations. Figure 4.34(c) confirms the folded structure of the polymer for $\xi = 1$ and $p = 1$. The mean square extension of the polymer grows as long as it reaches the extension of the $\diamond$-cavity for increasing number of segments N. Then the chain has to bend in order to grow more for increasing number of segments N. The mean end-to-end length now decreases until the chain has to turn around a second time to grow more, etc.

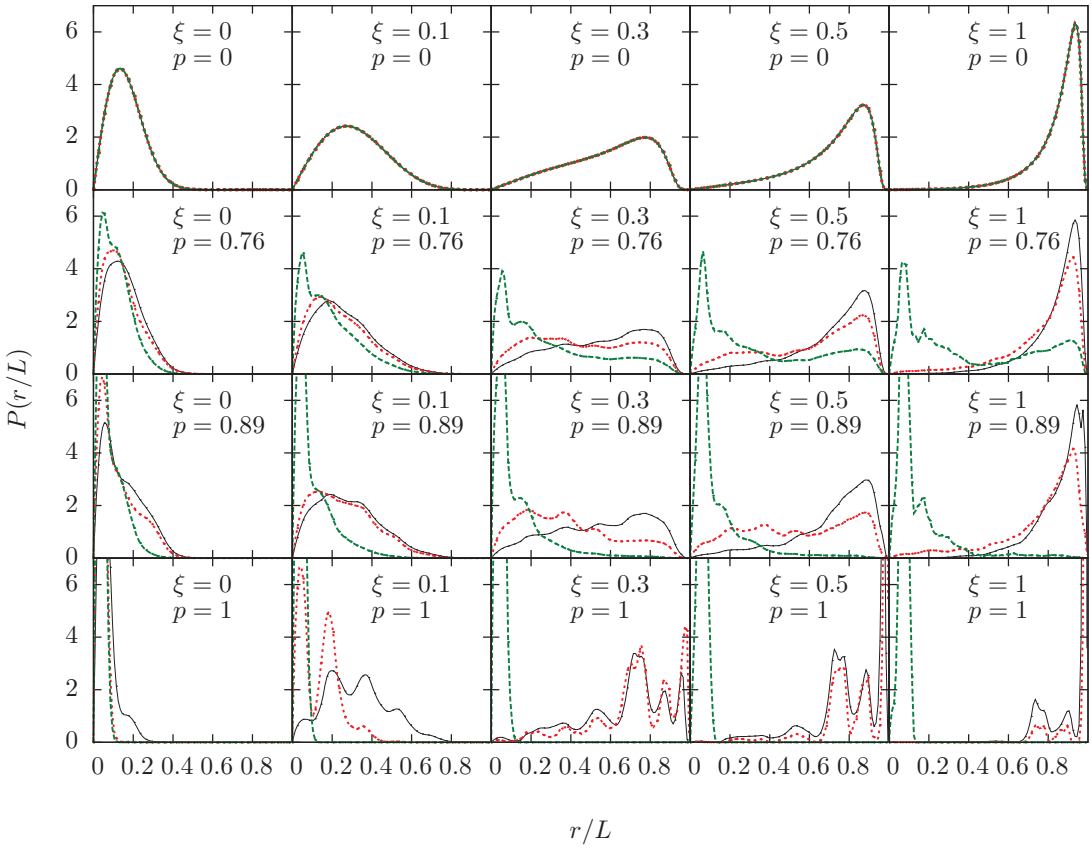

Figure 4.32.: Overview of the end-to-end distributions functions of a semiflexible polymer in lattice disorder. The parameters are given in the plot. The black curves (——) are for σ_1 (finite channel) and the red dashed curves (- - -) for σ_2 (pointlike channel), and (- - -) for σ_3 (no channel between neighboring disks).

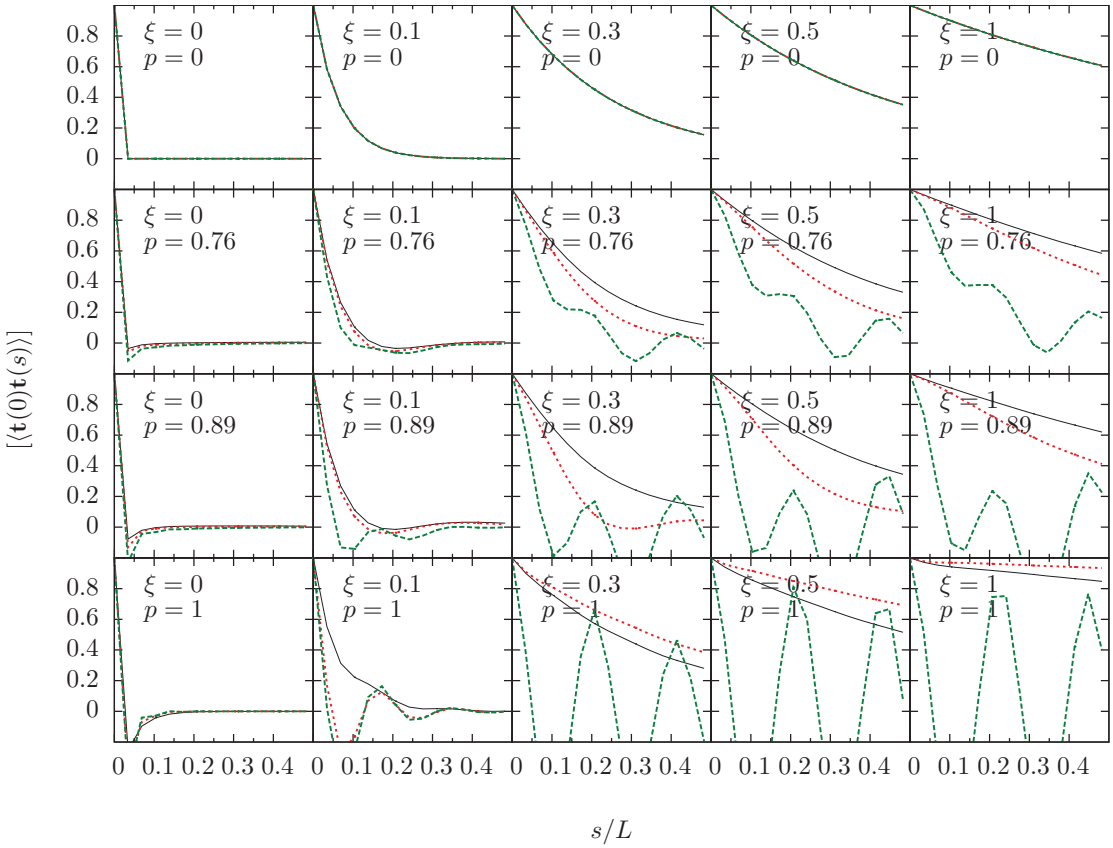

Figure 4.33.: Overview of the tangent correlation functions for the case of a semiflexible polymer ($N+1 = 30$ monomers) in lattice disorder. The parameters are given in the plot. The black curves (—) are for σ_1 (finite channel) and the red dashed curves (···) for σ_2 (pointlike channel), and (- - -) for σ_3 (no channel between neighboring disks).

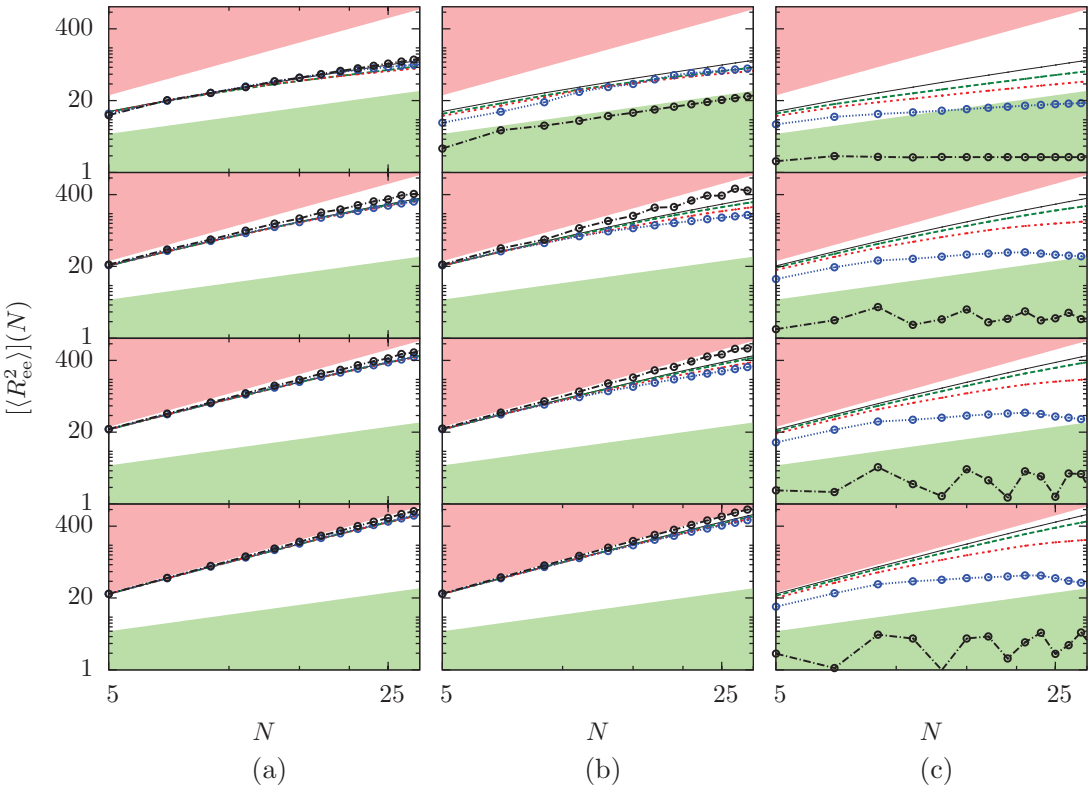

Figure 4.34.: Log-log plot of the mean square end-to-end distance of a semiflexible polymer. (a), (b), and (c) show the situations for the different disk diameters σ_1, σ_2, and σ_3. The occupation probabilities are: $p = 0$ (—, black), $p = 0.64$ (– –, green), 0.76 (···, red), 0.89 (·····, blue), and 1 (–·–, black).
The limiting case of random walk behavior $[\langle R_{ee}^2 \rangle](N) \propto N$ is indicated by the green shading, the ballistic limit $[\langle R_{ee}^2 \rangle](N) \propto N^2$ is indicated by the red shading.

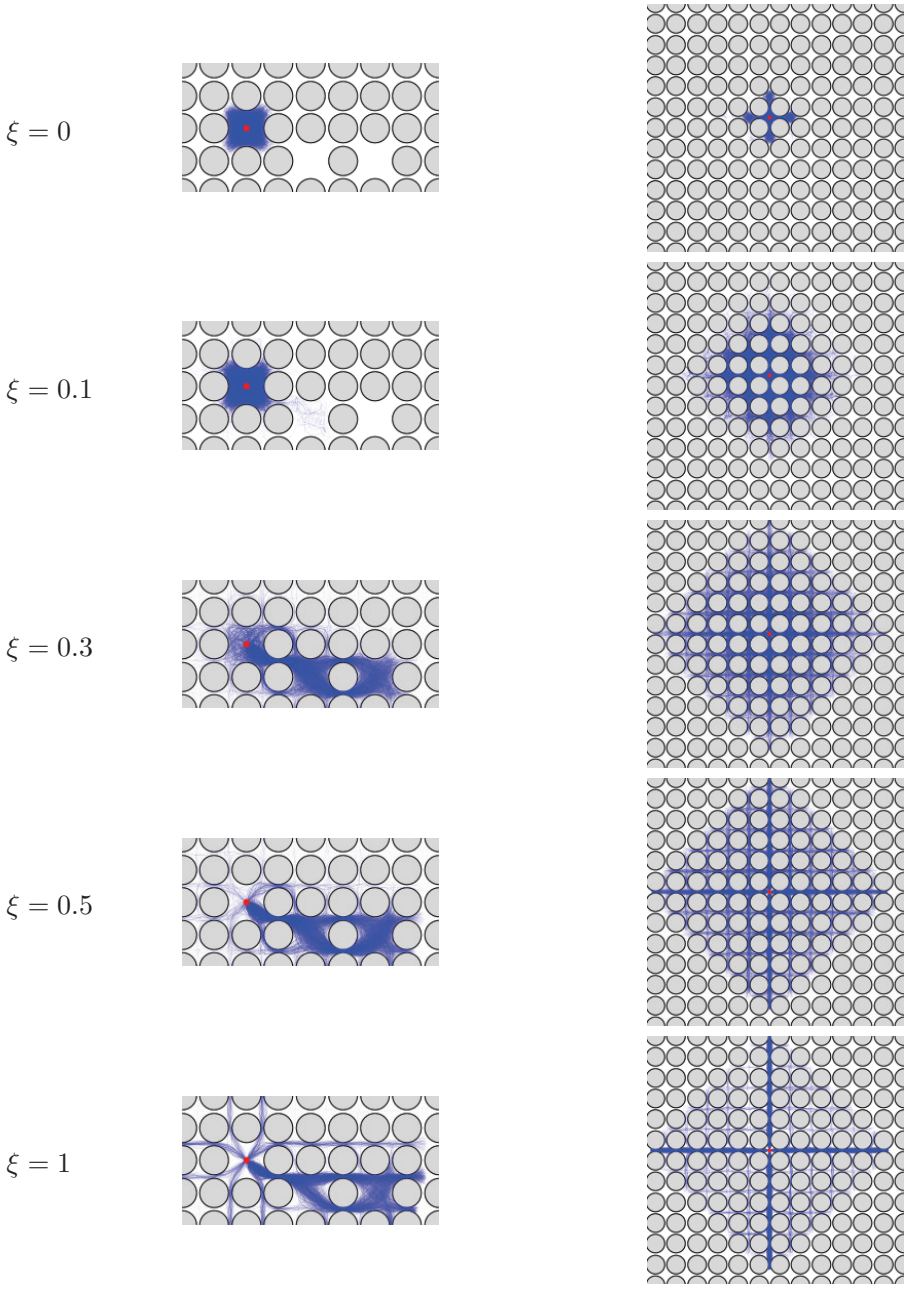

Figure 4.35.: Exemplary polymer distributions from simulations of a polymer ($N = 29$) exposed to disorder on the lattice. The disk diameter is σ_1 (finite channel between neighboring disks). (a) is a typical situation for $p = 0.89$, (b) for $p = 1$. The persistence length of the polymers is increased from top to bottom.

4.4.4. Concluding remarks

The above sections present a detailed analysis of the behavior of a polymer in a potential consisting of hard disks distributed on the sites of a square lattice. Depending on the ratio of persistence length and void space extension, the polymer either crumples up (small ξ) or straightens (large ξ) for increasing density of the potential. This is consistent with the results that, e.g., Cifra [45] found. Besides, the periodic structure of the lattice is reflected in the distribution functions of the polymer. Furthermore, I found that the distributions strongly reflect the local void-space cluster structure of the disorder due to the pinning of one end. Leaving the constraint of pinning is briefly touched in Sec. 4.6.

4.5. Semiflexible polymers in hard-disk fluid

We now switch from disorder on the lattice to off-lattice disorder. For fluid disorder, the structure inducing quantity will no longer be the occupation probability p but the area fraction ρ. For the connection of these quantities recall Table 4.1. For the case of fluid disorder I only look at one disk diameter, $\sigma = 5b$. The area fractions considered for the case of hard-disk fluid are $\rho = 0.1, 0.2, \ldots, 0.7$ corresponding to $M = 50, 101, \ldots, 360$ disks. The highest area fraction considered here is slightly below the melting point [73]. We begin by looking at the low density regime. The analysis of single disorder configurations is omitted because the extreme cases that can occur are covered by those of the previous sections. Since the densities I examined are beneath the melting point, pointlike channels do not play a dominant role which is in contrast to what we have looked at so far. Figure 4.43 can be considered for an illustration. The radial distribution function $g(r)$ of the hard-disk fluid for increasing area fraction ρ is shown in Fig. 4.36. The data are taken from a simulation. For the meaning and structure of $g(r)$ I refer to Sec. 2.2.2. The solid (black) curves in Fig. 4.36 exhibit weak correlations on the length scale of one disk diameter ($\sigma = 0.05$) and then immediately drop to no correlations. The dashed (red) curve, by contrast, which is at $\rho = 0.4$, exhibits a second peak. The low-density regime is determined by the characteristics of the free chain just like for the case of lattice disorder. Within the parameter range and resolution here we find deviations from the free-chain characteristics starting at about $\rho = 0.4$. A plot of the end-to-end distribution functions up to $\rho = 0.4$ can be seen in Fig. 4.37. In analogy to the analysis in Sec. 4.4.3, the persistence lengths include

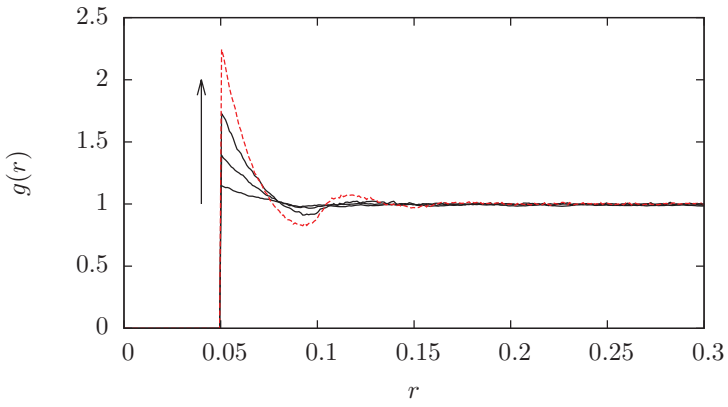

Figure 4.36.: Crossover from weak to strong correlations in the radial distribution function of a hard-disk fluid. The area fraction ranges from $\rho = 0.1, 0.2, 0.3, 0.4$ (increasing area fraction indicated by the arrow). The length is not normalized to one. Therefore the initial peak is at $r = 0.05$ which is the disk diameter σ.

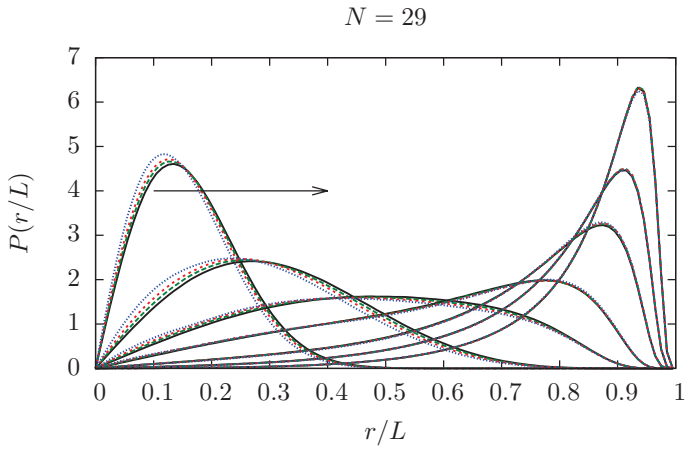

Figure 4.37.: End-to-end distribution function for $\xi = 0, 0.1, 0.2, 0.3, 0.5, 0.7, 1$ (increasing ξ indicated by the arrow). The area fractions are: $\rho = 0$ (—, black), 0.1 (- - -, green), 0.2 (- - -, red), and 0.3 (·····, blue).

$\xi = 0, 0.1, 0.2, 0.3, 0.5, 0.7, 1$. I will not go into the details of the low-density regime. The low-density behavior is more or less the same as for the case of disorder on the lattice, Sec. 4.4. The structural differences of the disorder and hence the differences in the distributions emerge for high densities. Below, the average distance between the disks is in a regime where polymers with small persistence lengths have enough space to evolve and adapting to the potential by contraction is on low energetic penalty, stiffer chains are just confined in their fluctuation width, as described in Sec. 4.4.3.

The examination of high densities is split into two parts. The first is addressed to the leading effects—compression and extension. The second part is concerned with the question of how the spatial correlations of the disorder are transferred to the spatial distributions of the polymer—here the end-to-end distribution function.

Figure 4.38 is an excerpt from a disorder realization including a pinpoint. The area surrounding the pinpoint is connected to the neighboring void space by passages between the disks. The width of these passages is strongly heterogeneous which again leads to different entropic contributions of the passages. The irregular structure of the fluid also prevents the formation of long channels. Most of the transitions between neighboring disks are blocked by other disks of the background potential. Especially the last issue strongly influences the impact of the disorder on the polymers. Similar to the situation of disorder on the lattice, the polymers are compressed as long as the persistence length is shorter than the mean extension (mean free length between neighboring disks) of the potential [45]. The phenomenology for larger persistence, however, differs considerably from the situation on the lattice. For investigating the leading impact of the disorder on the polymers we look at the tangent-tangent correlations [Fig. 4.39(a)] and at the mean square end-to-end distance [Fig. 4.39(b)].

For zero persistence, the potential leads to anticorrelations on short length scales and

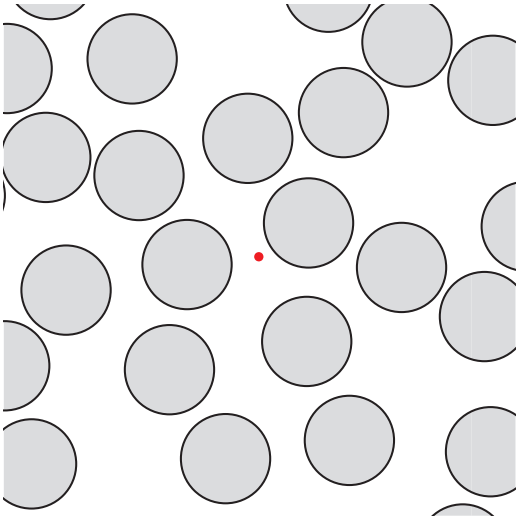

Figure 4.38.: Section of a fluid disorder realization with pinpoint.

decorrelation on longer length scales. For $\xi = 0.1$, increasing area fraction leads quickly to decorrelation [Fig. 4.39(a)]. This is corroborated by the mean square end-to-end distance, Fig. 4.39(b). For $\xi = 0.1$, an increasing area fraction leads to a slight decrease in the mean square end-to-end distance. For these two parameters ($\xi = 0, 0.1$), the persistence length is smaller than the mean free length of the potential (cp. Table 4.2) and adapting to it by compression is on low energetic cost [compare Fig. 4.25(a)]. If we increase the persistence more ($\xi = 0.2$), the chain is first compressed by the potential for increasing area fraction ($\rho = 0.4$) and then slightly stiffened ($\rho = 0.5, 0.6, 0.7$), which is indicated by an increase of the tangent correlations [Fig. 4.39(a)] and by a growth of the mean square end-to-end distance [Fig. 4.39(b)].

For $\xi = 0.3$, softening and stiffening seem to balance and there is hardly any effect seen due to an increase of the area fraction for the resolution and parameter range here. $\xi = 0.3$ represents a crossover where the persistence length reaches the mean distance of neighboring disks. The only way for the polymer to extend more is to cross the passages between neighboring disks. As the passages force a certain direction, crossing them leads to an increase of the end-to-end length and stronger correlations of the tangents. A further increase of the persistence, which in our case is $\xi = 0.5, 0.7$, and 1 inverts this effect again. Once the persistence length has exceeded the mean free length of the potential and the polymers start to cross the passages between neighboring disks, the bending term favors to extend even more in the direction of the passages. The fluid structure, however, has no long range channels. A look at Fig. 4.38 reveals this circumstance. A passage or channel built up by disks is only of short range before it is again blocked by another disk. Therefore, rather stiff polymers do often have to change their direction in order to adapt to the potential. This leads to a compression of the polymer which can be seen in Figs. 4.39(a) and (b). The decorrelation of the

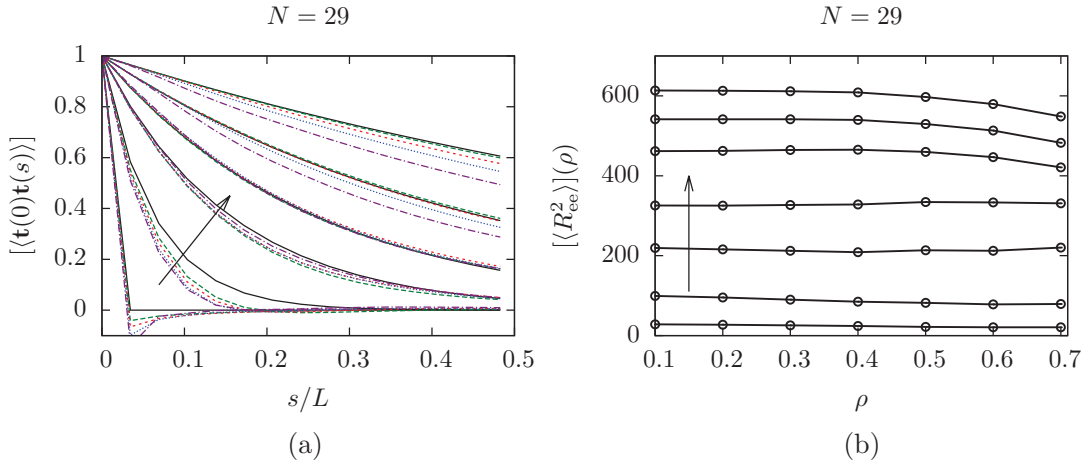

Figure 4.39.: Leading impact of a hard-disk fluid on a polymer. (a) shows the tangent-tangent correlations, with $\rho = 0$ (—, black), 0.4 (- - -, green), 0.5 (- - -, red), 0.6 (· · · · · ·, blue), and 0.7 (— · —, black). The direction of increasing persistence in bundles is indicated by the arrow. The persistence lengths cover $\xi = 0, 0.1, 0.2, 0.3, 0.5, 1$ (0.7 is left out for better visibility). (b) shows the mean square end-to-end distance in dependence on the density ρ. Increasing persistence is indicated by the arrow. The persistence lengths cover $\xi = 0, 0.1, 0.2, 0.3, 0.5, 0.7, 1$.

tangents occurs on shorter length scales for increasing area fraction ρ [Fig. 4.39(a)] and the mean square end-to-end distance decreases on the increase of ρ [Fig. 4.39(b)]. A real simulation example for the purpose of clarification is given in Fig. 4.43.

In the last described regime ($\xi = 0.5$–1), the persistence length is larger than the correlation length of the potential ($\ell_p \approx 6l_0$). On the one hand there are no long range channels and hence the polymers are forced to bent in order to adapt to the potential. On the other hand the curvatures that are necessary to adapt to the potential are rather small. A remarkable feature thereof is the maintenance of the functional form of the tangent correlations [Eq. (2.2)] but with an effective βJ yielding via Eq. (2.11) a renormalized persistence length ξ_r. This is approved by the fits to Eq. (2.2) in the semi-log plot of Fig. 4.40. The renormalized persistence lengths for $\rho = 0.4, 0.5, 0.6, 0.7$ are $\xi_r = 0.51, 0.5, 0.47, 0.42$ for $\xi = 0.5$ and $\xi_r = 0.98, 0.93, 0.85, 0.73$ for $\xi = 1$.

Going to even higher persistence lengths ($\ell_p \gg l_0$, here e.g. $\xi = 10$) leads yet to another regime, which I am currently investigating[12]. The large persistence lengths are comparable to a very low temperature [cp. Eq. (2.11)]. Therefore the resulting polymer configurations converge to the ground state behavior: they approach the least energy path. Preliminary results suggest a renormalized persistence length that is independent of the original one and only depends on the length scales of the potential

[12]This is done in close collaboration of S. Schöbl (author of this work), S. Sturm, K. Kroy, and W. Janke.

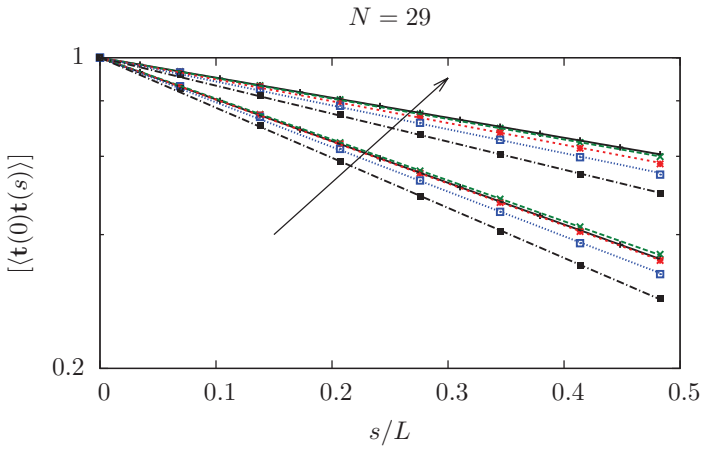

Figure 4.40.: Tangent-tangent correlation function for $\xi = 0.5, 1$ in semi-log scaling. The arrow indicates increasing persistence. The occupation probabilities are: $\rho = 0$ (—, black), 0.4 (- - -, green), 0.5 (····, red), 0.6 (·····, blue), and 0.7 (-·-, black). The connecting lines are fits to Eq. (2.2) and the direct application of Eq. (2.2) for $\rho = 0$, respectively.

(l_0 and σ).

In the typical spirit of "blob" arguments, this can be understood as a long series of uncorrelated void spaces along the polymer backbone inducing kinks of random magnitude and thus in the long run reestablishing a Gaussian diffusion process in tangent space, but with a larger, disorder-dependent variance [104].

After having discussed the leading behavior of a polymer when exposed to hard-disk fluid disorder, we now come to the issue of how the spatial correlations of the fluid are transferred to the spatial distribution functions of the polymer. Local effects (e.g. clustering) do not play a big role within the parameter range considered here. Therefore the fluid structure is not subject to strong inhomogeneities. A consequence thereof might be the maintenance of the free chain characteristics in, e.g., the end-to-end distribution function which can be seen at the bottom of Fig. 4.41. The main peaks are slightly shifted for increasing area fraction ρ, but the rough shape is kept. The transfer of the structure of the radial distribution $g(r)$ to the end-to-end distribution function $P(r)$ can be seen in Fig. 4.41. A plot of the void-space distribution function (VSDF) $g_V(r)$ (cp. Sec. 2.2.2) for $\rho = 0.7$ is shown at the top of Fig. 4.41. The peaks of the VSDF are approximately at the positions of the peaks of the end-to-end distribution function for $\rho = 0.7$.

Another attempt to analyze how the correlations of the radial distribution function $g(r)$ affect the end-to-end distribution function is a multiplicative superposition of the end-to-end distribution function of a free polymer (no disorder) at a certain persistence length ξ_0 and the VSDF $g_V(r)$ at a certain area fraction ρ. The result is compared to the end-to-end distribution function of a polymer with persistence length ξ_0 exposed to

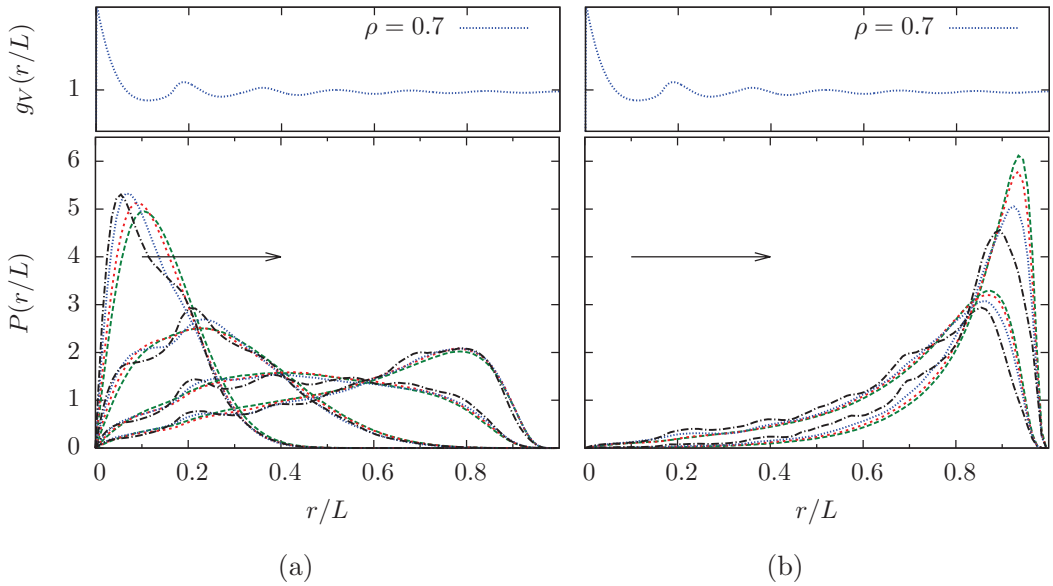

Figure 4.41.: End-to-end distribution function for $\xi = 0, 0.1, 0.2, 0.3$,(a), and $\xi = 0.5, 1$,(b). The occupation probabilities are: $p = 0.4$ (- - -, green), 0.5 (- - -, red), 0.6 (·····, blue), and 0.7 (— · —, black). There is a plot of the void-space distribution function [Fig. 2.7(b)] for $\rho = 0.7$ on top of the plots of the radial distribution function which gives an impression of the similarity of the periodic structure of end-to-end distribution and radial distribution function.

disorder at area fraction ρ. The results of the superposition as well as the corresponding end-to-end distribution functions for $\rho = 0.7$ can be seen in fig. 4.42.

The motivation of the multiplicative superposition is the assumption that a certain end-to-end distance depends on the probability to find a void space a distance r apart from the pinpoint in addition to the probability to find an end-to-end length of r. This has of course to be understood as a rough qualitative estimate, because the one-on-one multiplication of the end-to-end distribution function of the free polymer with the VSDF is an assumption. Nevertheless, the superposition gives a good impression of how the radial distribution function $g(r)$, resp. the void-space distribution function $g_V(r)$ of the fluid, is connected to the end-to-end distribution function of the polymer.

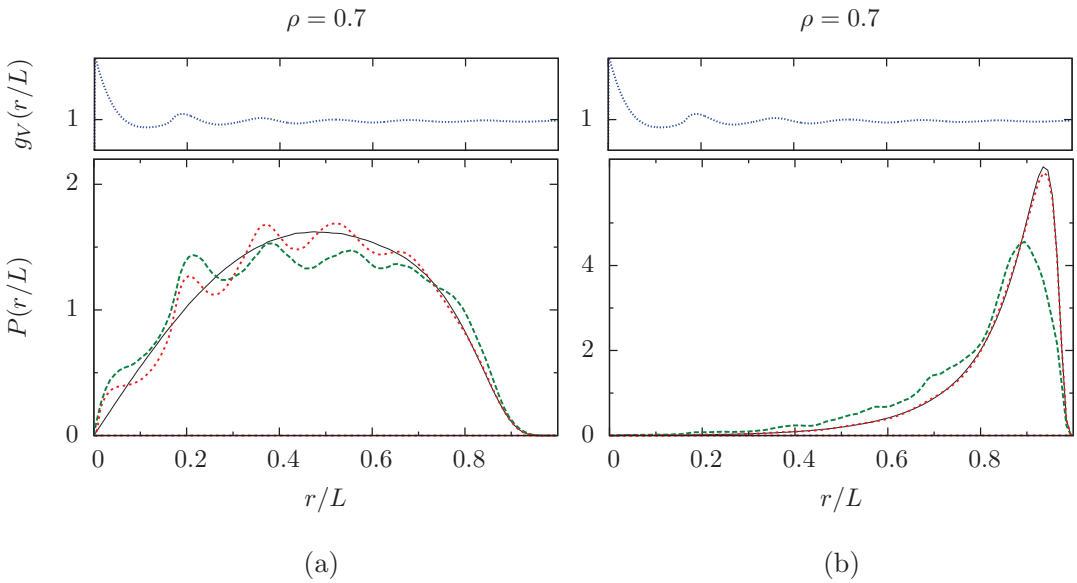

Figure 4.42.: The plot shows the void-space distribution function $g_V(r)$ at area fraction $\rho = 0.7$ as taken from simulations [top of (a) and (b)]. The solid (black) line in the bottom plots is the end-to-end distribution function of a free polymer for $\xi = 0.2$ (a) and $\xi = 1$ (b). The dashed (green) lines are the corresponding end-to-end distribution functions at $\rho = 0.7$ and the short-dashed (red) lines are the multiplicative superpositions of the end-to-end distribution function of a free polymer with the void-space distribution functions $g_V(r)$ of the fluid at $\rho = 0.7$.

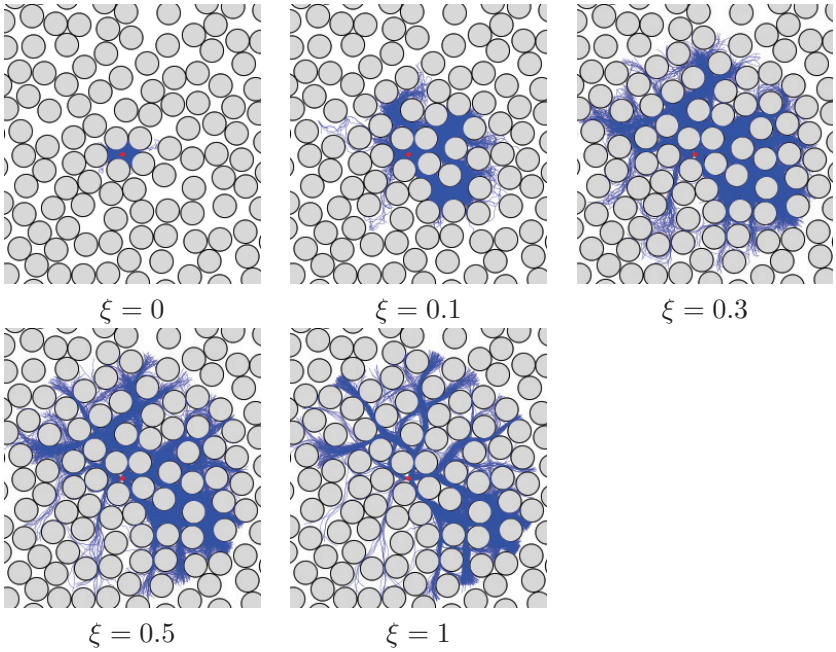

Figure 4.43.: Exemplary polymer distributions from a simulation of a polymer in hard-disk fluid disorder for increasing persistence length ξ.

4.5.1. Concluding remarks

In this section I examined in detail the response of a semiflexible polymer to a quenched random environment modeled as hard-disk fluid. The leading effects I found are determined by the competing length scales of the disorder and of the polymer—the average distance between the obstacles and the persistence length. Depending on their ratio, my findings include softening and stiffening of the polymer for persistence lengths up to the average distance of the obstacles. Going to higher persistence reverts this effect. The polymers are again softened. For the semiflexible case I found a renormalization of the persistence length that depends on the original one. Going to higher persistence lengths makes the polymer approach the minimum energy path. Preliminary results suggest that the corresponding renormalized persistence length no longer depends on the original one but only on the properties of the potential.

A higher order effect is the modulation of the spatial correlations of the disorder on top of the end-to-end distribution function of the free polymer.

4.6. Leaving the constraint of a fixed pinpoint

The discussion so far was subject to the constraint of a fixed pinpoint. In this section, I compare results of a non-fixed polymer to the previous case and discuss the differences that arise. The data for the non-fixed case originate from a multicanonical Monte Carlo simulation[13], in which the polymer may move through space by means of standard rotation and translation updates. Figure 4.44 shows results for exemplary parameters. It can be seen that for fully occupied lattices the end-to-end distributions do not differ, as it is the case for the free polymer and low disorder densities. In the high-density regime, on the other hand, the measured observables show strong differences especially in the crossover regime of $\xi = 0.3$. This can be understood considering the following entropic and energetic arguments. Other than the fully occupied or the low-density case, high disorder densities produce small void spaces of different sizes which are entropically more favorable than the alternative channels. In the case of non-fixed constraints, the polymers are able to move to those small spaces and thus they contribute stronger as long as the energetic cost for bending is not too high. The results can be seen in Fig. 4.44 where the end-to-end distribution shows deviations from the case of a fixed pinpoint in the crossover regime. This effect is less pronounced for large persistence lengths, since possible gains in entropy are dominated by the cost of bending energy.

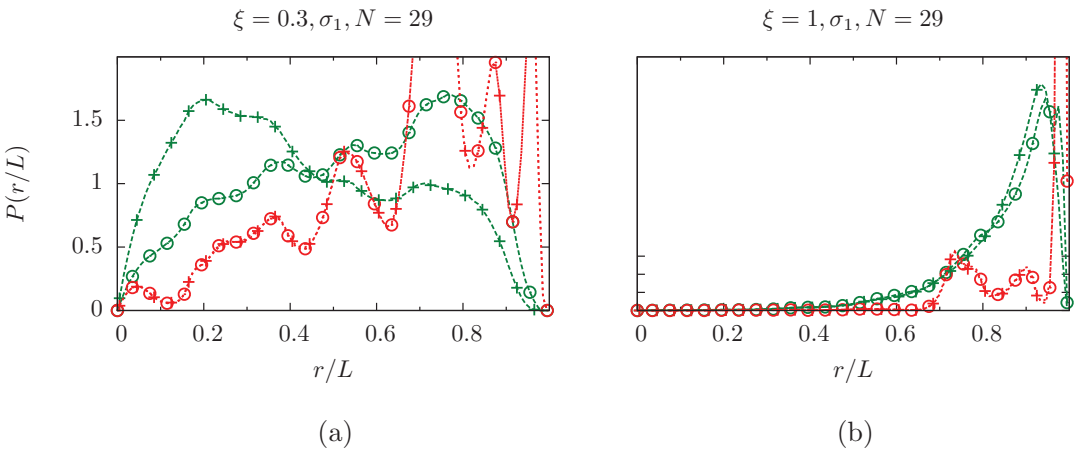

Figure 4.44.: End-to-end distribution function for $\xi = 0.3$ (a) and $\xi = 1$ (b). The occupation probabilities are: $p = 0.89$ (- - -, green), 1.00 (····, red). The data marked by + are for chains that are free to move throughout space (no pinpoint) and are done by a multicanonical Monte Carlo simulation. The data marked by ∘ are for fixed starting point and are obtained with the growth method.

[13]The data were simulated by Johannes Zierenberg who was participant in a BuildMoNa miniproject that was supervised by the author (see also Footnote 10).

5. Summary and conclusion

As alluded to in the beginning, the physical properties of semiflexible polymers are of considerable importance to cytoskeletal stability, cell division, cell motility and other biological processes. Consequently, these properties have received much attention during the last 20 years as new high-resolution measurement techniques such as optical tweezers or the atomic force microscope rendered the mechanical response of single molecules experimentally accessible. These single-molecule investigations have firmly established the *wormlike chain* model as a minimal, but accurate two-parameter description of semiflexible polymers in terms of the (constant) contour length L and the stiffness length, or *persistence length*, ℓ_p. However, the intrinsic persistence length exhibited by a polymer in isolation must fall short of an accurate description of the cytoskeletal reality as it completely neglects environmental interactions. Besides energetic interactions induced, e.g., by crosslinking molecules, the simple fact that the cytoskeleton is packed full of other macromolecules leaves a polymer little choice but to abandon its equilibrium conformation and instead adapt to the space available.

We have investigated this latter, steric type of interactions using extensive numerical simulations of a long, grafted wormlike chain polymer exposed to two different, archetypal classes of disorder: (i) lattice disorder, representing a highly correlated background potential at large densities and allowing for direct comparison to existing, less comprehensive results in the literature and (ii) fluid disorder which, though frozen during the simulation, bears the statistical structure of an equilibrium fluid and thus typifies a "natural" obstacle distribution. Both (i) and (ii) have been investigated over a broad range of background densities and polymer stiffnesses.

Algorithmically, the strong fragmentation of space into valleys separated by infinite energy barriers renders traditional methods of computational polymer physics infeasible. Typical Markov Chain Monte Carlo methods rely on the computationally cheap, but unguided generation of random trial conformations which must then be discarded if they collide with surrounding obstacles. At background densities above the gaseous phase, rejection rates quickly approach unity, limiting the resulting ensemble to a small number of metastable states. In the semiflexible regime, this difficulty is exacerbated by the energetic suppression of globular conformations, as a representative "equilibrium conformation" has to wind around a greater number of obstacles. Even generalized ensemble methods such as the multicanonical Monte Carlo technique, though they can do much to alleviate these problems, become increasingly inefficient at high disorder densities and persistence lengths.

Since hard obstacles prove so difficult to overcome, a solution that almost suggests itself is to go around; I chose to do so on the basis of a *breadth-first growth algorithm* due to Garel and Orland. The main idea is to generate equilibrium ensembles

of grafted polymers by successively polymerizing a number of shorter chains in all available directions at once. Because each polymerization step amounts to choosing a single bending angle on the unit circle, instead of trying to find a way through the high-dimensional polymer configuration space, as traditional simulation methods do, it is comparably easy to apply a certain amount of foresight in navigating around obstructed areas. To this end, I introduced guiding fields sampling preferentially those angles leading towards free spaces and not causing excessively large bending energies. A further technical advantage of growth algorithms in general is that simulations of a single polymer length already allow for scaling analyses, as the resulting chain ensembles remain equilibrated at each intermediate growth step.

To make sure that the physically motivated bias introduced by the guiding fields did not overwhelm the algorithm's natural convergence to thermal equilibrium (which, obviously, can only be blindly relied on in the fictive limit of infinite chain populations), I compared my results to data obtained from multicanonical MC simulations in close collaboration with my colleague Johannes Zierenberg. Though the multicanonical MC method failed to cover the full parameter range discussed here, it still managed to capture a large part of it and, where applicable, corroborated my findings.

The investigation of flexible polymers in low-density lattice disorder served as a further testbed, as results on similar systems are readily available in the literature. I confirmed existing results such as the saturation of the mean polymer extension for increasing monomer number, and extended them to greater densities than hitherto studied, finally maxing out at the fully occupied lattice. At increasing persistence lengths, the fully occupied lattice with its abundance of straight and narrow channels was shown to increase the apparent persistence length, in stark contrast to the effective flexibilization observed for fluid disorder.

In general, correlations of the background potential are directly imparted onto the polymeric end-to-end distribution function, with local minima and maxima of the latter reflecting the distribution of free space within the disorder landscape. More precisely, the locations of these minima and maxima can be inferred from a void space correlation function that formalizes the abovementioned notion of "free space distribution" and is easy to evaluate numerically. We expect this transfer of void space correlations to hold irrespectively of the exact choice of background potential. A similarly robust, and even more interesting, observation is that in the limit of long and stiff polymers, a statistically homogeneous, isotropic obstacle distribution with finite correlation length—such as the quenched hard disk fluid—produces wormlike chain behavior on long scales, albeit with a renormalized persistence length. Preliminary results suggest that this renormalized persistence length becomes independent of ℓ_p in the limit $\ell_p \to \infty$, as expected on theoretical grounds.

As a closing remark, let me mention that while a biologist may wonder at the rather superficial resemblance between a quenched ensemble of hard spheres and molecular crowding within the cytoskeleton, our qualitative results should remain true as long as energy barriers are large and the environment can be considered "frozen" on the timescale of polymer fluctuations. Besides allowing for direct experimental realization, for instance by a faithful implementation of our obstacle distributions using microflu-

idic lithography [105], our approach also permits further adaptation to the biological problem domain by, e.g., replacing the hard-core interaction potential with a soft force field or by making the switch to three dimensions. The most interesting avenue of further research might, however, lie within the reemergence of wormlike chain behavior in the limit $L, \ell_p \to \infty$, a subject that is currently under active investigation.

Appendices

A. Additional data for the polymer exposed to disorder on the lattice

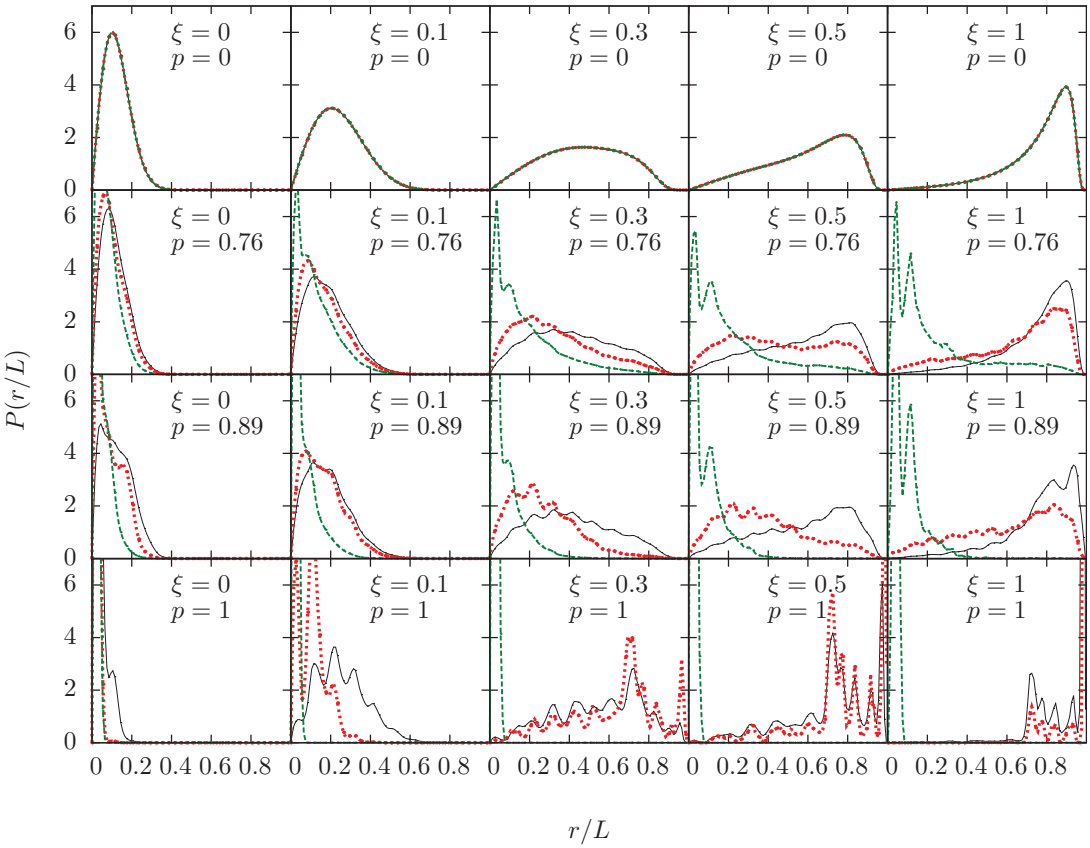

Figure A.1.: End-to-end distribution functions for the case of a semiflexible polymer in disorder modeled as hard disks on the sites of a square lattice for $N + 1 = 50$ monomers. The black curves (—) are for σ_1 (finite channel) and the red dashed curves (····) for σ_2 (pointlike channel), and (- - -) for σ_3 (no channel between neighboring disks).

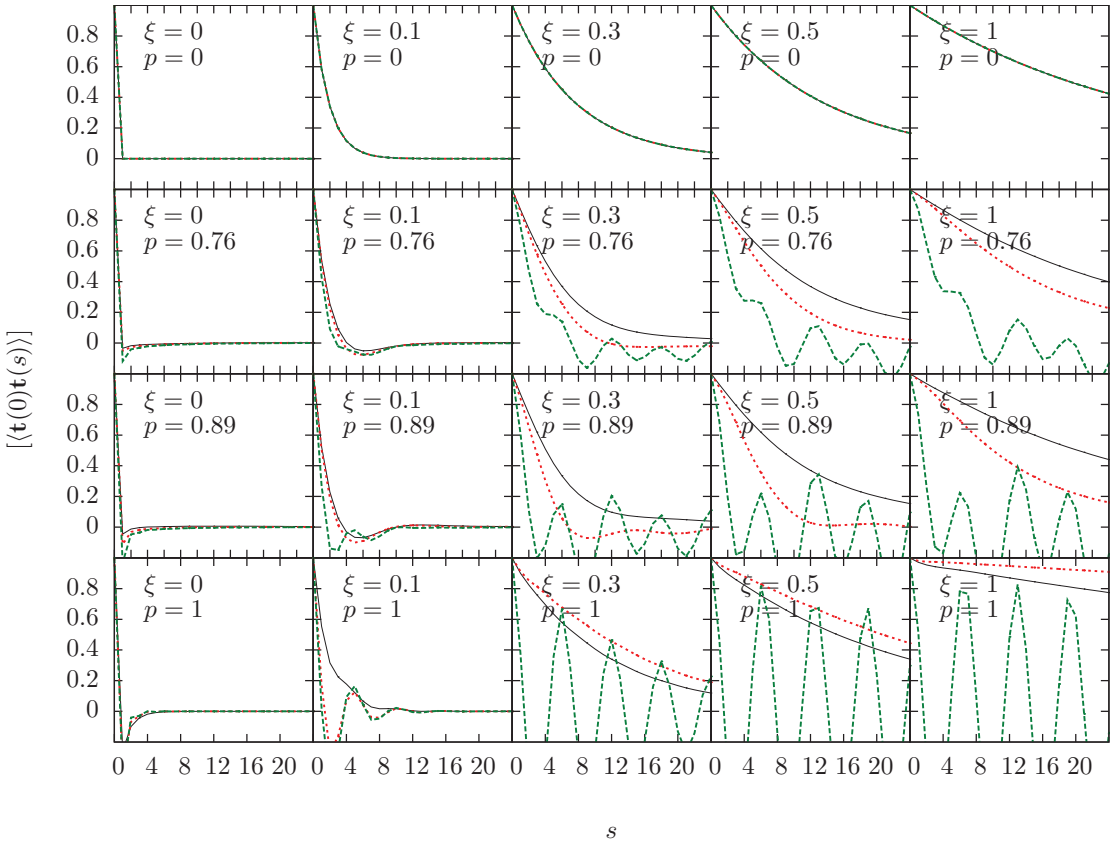

Figure A.2.: Tangent-tangent correlation functions for the case of a semiflexible polymer in disorder modeled as hard disks on the sites of a square lattice for $N + 1 = 50$ monomers. The black curves (—) are for σ_1 (finite channel) and the red dashed curves (- - -) for σ_2 (pointlike channel), and (- - -) for σ_3 (no channel between neighboring disks).

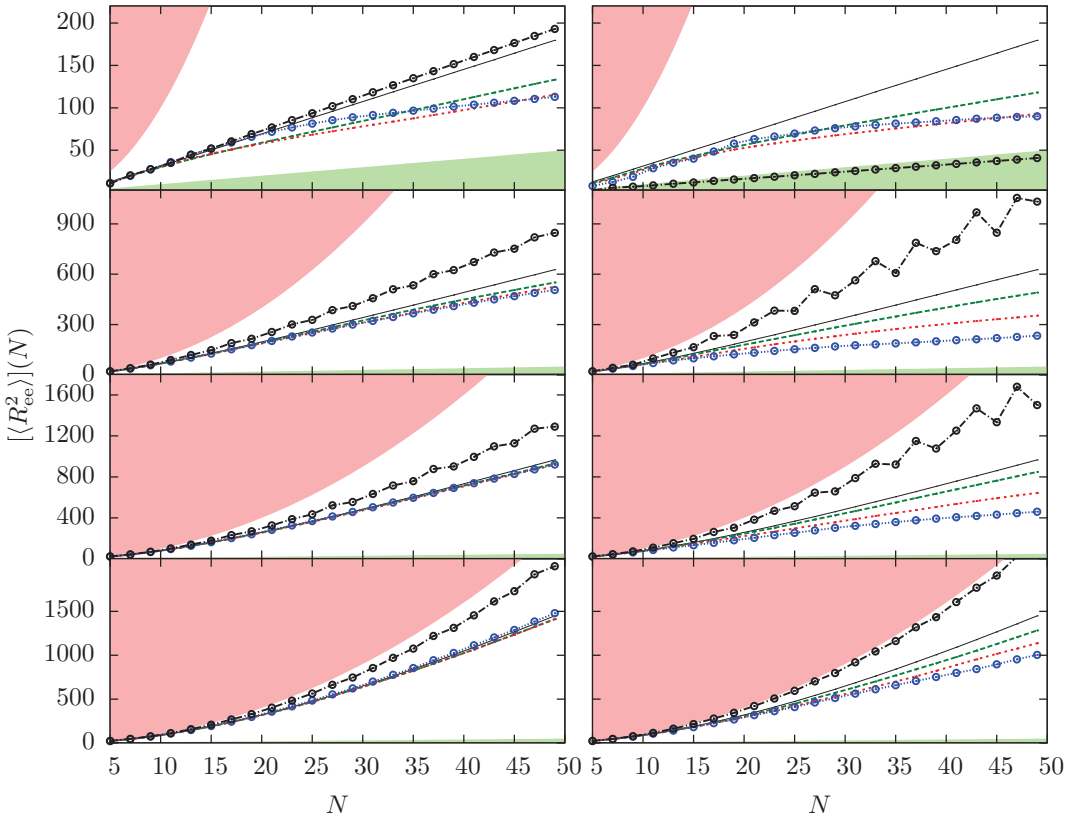

(a) (b)

Figure A.3.: The figure shows a linear plot of the scaling of the mean square end-to-end distance for σ_1 (a) and σ_2 (b) and $\xi = 0.1, 0.3, 0.5, 1$ (from top to bottom). The occupation probabilities are: $p = 0$ (—, black), $p = 0.64$ (- - -, green), 0.76 (- - -, red), 0.89 (·····, blue), and 1 (– · –, black).
The limiting case of random walk behavior $[\langle R^2_{ee}\rangle](N) \propto N$ is indicated by the green shading, the ballistic limit $[\langle R^2_{ee}\rangle](N) \propto N^2$ is indicated by the red shading.

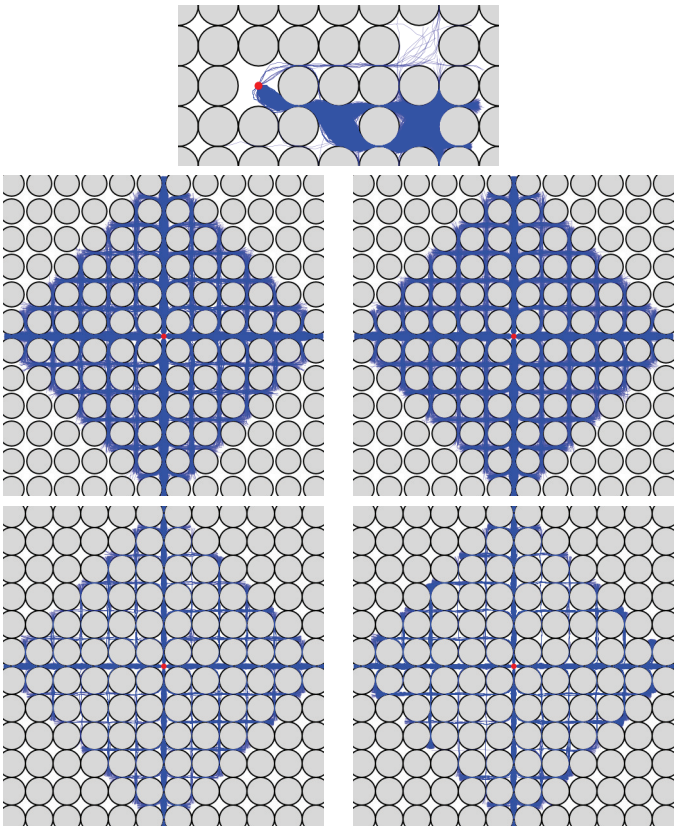

Figure A.4.: Simulations examples for polymers exposed to disorder arranged on a lattice. The persistence length for all cases that are shown here is $\xi = 1$. The first row is for $\sigma = 0.05$ (σ_2). The picture shows paradigmatically that the growth method finds void space that is far distant from the starting point and difficult to reach as it is separated by three pointlike channels. It also shows that the entropic contribution is only marginal even though the void space is relatively large. The reason is the poor connection to the starting point. The second row shows a fully occupied lattice with $\sigma = 0.045$ (σ_1). (a) is made with the growth algorithm; (b) with the multicanonical method. The finite channels allow for good sampling and lead to fully consistent results. The third row shows the same as the second but with $\sigma = 0.05$. The lack of symmetry in sampling although the pinpoint is at a symmetric position is a hint of a bad sampling. Both algorithms exhibit this problem. An adaption of the guiding field might cure this problem at least for the case of the growth algorithm.

B. Additional data for the polymer exposed to fluid disorder

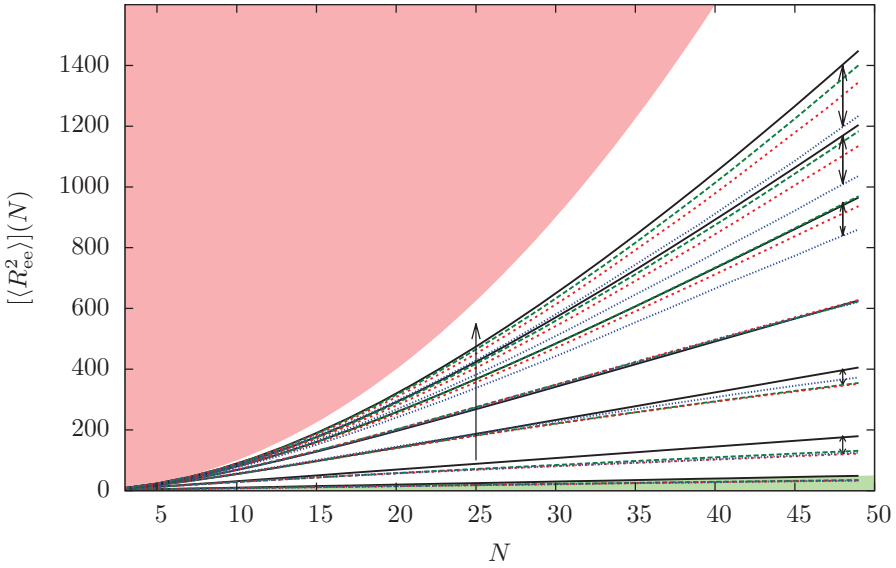

Figure B.1.: Scaling of the mean square end-to-end distance of a polymer in fluid disorder for $\xi = 0, 0.1, 0.2, 0.3, 0.5, 0.7, 1$ (increasing ξ indicated by the single headed arrow). The double headed arrows indicate data belonging to one value of the persistence (those that are clearly to be identified are not indicated by an arrow). The area fractions are: $\rho = 0$ (—, black), 0.5 (- - -, green), 0.6 (- - -, red), and 0.7 (·····, blue).
The limiting case of random walk behavior $[\langle R_{ee}^2 \rangle](N) \propto N$ is indicated by the green shading, the ballistic limit $[\langle R_{ee}^2 \rangle](N) \propto N^2$ is indicated by the red shading.

Bibliography

[1] B. Wagner, R. Tharmann, I. Haase, M. Fischer, and A. R. Bausch, Proc. Natl. Acad. Sci. USA **103**, 13974 (2006).

[2] C. Bustamente, Z. Bryant, and S. B. Smith, Nature **421**, 423 (2003).

[3] O. L. J. Harriman and M. C. Leake, J. Phys.: Condens. Matter **23**, 503101 (2011).

[4] S. B. Smith, L. Finzi, and C. Bustamante, Science **258**, 1122 (1992).

[5] M. D. Wang, H. Yin, R. Landick, J. Gelles, and S. M. Block, Biophys. J. **72**, 1335 (1997).

[6] T. T. Perkins, S. R. Quake, D. E. Smith, and S. Chu, Science **264**, 822 (1994).

[7] K. M. Taute, F. Pampaloni, E. Frey, and E.-L. Florin, Phys. Rev. Lett. **100**, 028102 (2008).

[8] C. Semmrich, T. Storz, J. Glaser, R. Merkel, A. R. Bausch, and K. Kroy, Proc. Natl. Acad. Sci. USA **104**, 20199 (2007).

[9] B. Alberts, A. Johnson, J. Lewis, M. Reff, K. Roberts, and P. Walter, *Molecular Biology of the Cell*, 4th ed. (Garland Science, New York, 2002).

[10] D. Humphrey, C. Duggan, D. Saha, D. Smith, and J. Käs, Nature **416**, 413 (2002).

[11] C. Zhu, G. Bao, and N. Wang, Annual Review of Biomedical Engineering **2**, 189 (2000).

[12] D. A. Fletcher and R. D. Mullins, Nature **463**, 485 (2010).

[13] L. Wolff, P. Fernandez, and K. Kroy, New Journal of Physics **12**, 053024 (2010).

[14] M. Doi and S. F. Edwards, *The Theory of Polymer Dynamics* (Oxford University Press, Oxford, 1986).

[15] J. Wilhelm and E. Frey, Phys. Rev. Lett. **77**, 2581 (1996).

[16] R. Götter, K. Kroy, E. Frey, M. Bärmann, and E. Sackmann, Macromolecules **29**, 30 (1996).

[17] A. Ott, M. Magnasco, A. Simon, and A. Libchaber, Phys. Rev. E **48**, 1642 (1993).

[18] F. Pampaloni, G. Lattanzi, A. Jon, T. Surrey, E. Frey, and E.-L. Florin, Proc. Natl. Acad. Sci. USA **103**, 10248 (2006).

[19] F. Gittes, B. Mickey, J. Nettleton, and J. Howard, J. Cell Biol. **120**, 923 (1993).

[20] M. Schopferer, H. Bär, B. Hochstein, S. Sharma, N. Mücke, H. Herrmann, and N. Willenbacher, J. Mol. Biol. **388**, 133 (2009).

[21] H. Isambert, P. Venier, A. C. Maggs, A. Fattoum, R. Kassab, D. Pantaloni, and M.-F. Carlier, J. Biol. Chem. **270**, 11437 (1995).

[22] O. Kratky and G. Porod, Rec. Trav. Chim. Pays-Bas. **68**, 1106 (1949).

[23] G. Guillot, L. Leger, and F. Rondelez, Macromolecules **18**, 2531 (1985).

[24] D. S. Cannell and F. Rondelez, Macromolecules **13**, 1599 (1980).

[25] M. T. Bishop, K. H. Langley, and F. E. Karasz, Phys. Rev. Lett. **57**, 1741 (1986).

[26] M. E. Cates and R. C. Ball, J. Phys. France **49**, 2009 (1988).

[27] S. F. Edwards and M. Muthukumar, J. Chem. Phys. **89**, 2435 (1988).

[28] Y. Y. Goldschmidt, Phys. Rev. E **61**, 1729 (2000).

[29] Y. Shiferaw and Y. Y. Goldschmidt, Phys. Rev. E **63**, 051803 (2001).

[30] J. Machta, Phys. Rev. A **40**, 1720 (1989).

[31] T. Nattermann and W. Renz, Phys. Rev. A **40**, 4675 (1989).

[32] S. Stepanow, J. Phys. A **25**, 6187 (1992).

[33] A. Baumgärtner and M. Muthukumar, J. Chem. Phys. **87**, 3082 (1987).

[34] Y. Y. Goldschmidt and Y. Shiferaw, Eur. Phys. J. B **32**, 87 (2003).

[35] J. Machta and T. R. Kirkpatrick, Phys. Rev. A **41**, 5345 (1990).

[36] S. F. Edwards, Proc. Phys. Soc. **92**, 9 (1967).

[37] P.-G. de Gennes, J. Chem. Phys. **55**, 572 (1971).

[38] H. Hinsch and E. Frey, ChemPhysChem **10**, 2891 (2009).

[39] M. Romanowska, H. Hinsch, H. Kirchgener, M. Giesen, M. Degawa, B. Hoffmann, E. Frey, and R. Merkel, Europhys. Lett. **86**, 26003 (2009).

[40] A. Dua and T. A. Vilgis, J. Chem. Phys. **121**, 5505 (2004).

[41] T. Odijk, Macromolecules **16**, 1340 (1983).

[42] F. Brochard-Wyart, T. Tanaka, N. Borghi, and P.-G. de Gennes, Langmuir **21**, 4144 (2005).

[43] P. Romiszowski and A. Sikorski, Journal of Non-Crystalline Solids **352**, 4303 (2006).

[44] F. Wagner, G. Lattanzi, and E. Frey, Phys. Rev. E **75**, 050902 (2007).

[45] P. Cifra, J. Chem. Phys. **136**, 024902 (2012).

[46] P.-G. de Gennes, *Scaling Concepts in Polymer Physics* (Cornell University Press, Brook Street, London, UK, 1979).

[47] D. W. Schaefer, J. F. Joanny, and P. Pincus, Macromolecules **13**, 1280 (1980).

[48] D. Bensimon, B. Dohmi, and M. Mézard, Europhys. Lett. **42**, 97 (1998).

[49] P. Debnath and B. J. Cherayila, J. Chem. Phys. **118**, 1970 (2003).

[50] S. Muhuri and M. Rao, J. Stat. Phys. **2010**, P02005 (2010).

[51] S. Schöbl, J. Zierenberg, and W. Janke, Phys. Rev. E **84**, 051805 (2011).

[52] V. Blavatska and W. Janke, J. Phys. A **42**, 015001 (2009).

[53] V. Blavatska and W. Janke, Europhys. Lett. **82**, 66006 (2008).

[54] J. D. Honeycutt and D. Thirumalai, J. Chem. Phys. **80**, 4542 (1989).

[55] V. Yamakov and A. Milchev, Phys. Rev. E **55**, 1704 (1997).

[56] D. Wu, K. Hui, and D. Chandler, J. Chem. Phys. **96**, 835 (1992).

[57] S. F. Edwards, NBS. Misc. Publ. **273**, 225 (1965).

[58] N. Metropolis, A. W. Rosenbluth, M. N. Rosenbluth, A. H. Teller, and E. Teller, J. Chem. Phys. **21**, 1087 (1953).

[59] R. H. Swendsen and J.-S. Wang, Phys. Rev. Lett. **57**, 2607 (1986).

[60] D. J. Earl and M. W. Deem, Phys. Chem. Chem. Phys. **7**, 3910 (2005).

[61] B. A. Berg and T. Neuhaus, Phys. Lett. B **267**, 249 (1991).

[62] B. A. Berg and T. Neuhaus, Phys. Rev. Lett. **68**, 9 (1992).

[63] W. Janke, Physica A **254**, 164 (1998).

[64] C. J. Thompson, *Classical Equilibrium Statistical Mechanics* (Oxford University Press, Oxford, 1988).

[65] M. Abramowitz and A. I. Stegun, *Handbook of Mathematical Functions* (Dover Publications, New York, 1965).

[66] L. D. Landau and E. M. Lifshitz, *Theory of Elasticity* (Pergamon Press, Oxford, 1959).

[67] B. Hamprecht, W. Janke, and H. Kleinert, Phys. Lett. A **330**, 254 (2004).

[68] B. Hamprecht and H. Kleinert, Phys. Rev. E **71**, 031803 (2005).

[69] D. Stauffer and A. Aharony, *Introduction to Percolation Theory* (CRC Press, Chestnut Street, Philadelphia, US, 1985).

[70] M. F. Sykes and M. Glen, J. Phys. A: Math. Gen. **9**, 87 (1976).

[71] M. D. Rintoul and S. Torquato, Phys. Rev. Lett. **77**, 4198 (1996).

[72] B. J. Alder and T. E. Wainwright, J. Chem. Phys. **27**, 1208 (1957).

[73] E. P. Bernard and W. Krauth, Phys. Rev. Lett. **107**, 155704 (2011).

[74] A. van Blaaderen and P. Wiltzius, Science **270**, 1177 (1995).

[75] W. Krauth, *Statistical Mechanics: Algorithms and Computations* (Oxford University Press, Oxford, 2006).

[76] J.-P. Hansen and I. R. McDonald, *Theory of simple liquids* (Academic Press, New York, 1986).

[77] *Theory and Simulation of Hard-Sphere Fluids and Related Systems*, edited by A. Mulero (Springer, Heidelberg, DE, 2008).

[78] M. Adda-Bedia, E. Katzav, and D. Vella, J. Chem. Phys. **129**, 144506 (2008).

[79] M. D. Rintoul and S. Torquato, Phys. Rev. E **52**, 2635 (1995).

[80] S. Sastry, D. S. Corti, P. G. Debenedetti, and F. H. Stillinger, Phys. Rev. E **56**, 5524 (1997).

[81] P. Holgate, Biometrika **68**, 712 (1981).

[82] N. G. van Kampen, *Stochastic Processes in Physics and Chemistry* (Elsevier, Amsterdam, 1981).

[83] J. Honerkamp, *Statistical Physics—An Advanced Approach with Applications* (Springer, Berlin, 1998).

[84] M. E. J. Newman and G. T. Barkema, *Monte Carlo Methods in Statistical Physics* (Oxford University Press, Oxford, 2001).

[85] S. Schöbl, Master's thesis, Universität Leipzig, 2008.

[86] W. Janke, NIC Series **10**, 423 (2002).

[87] B. Widom, J. Chem. Phys. **44**, 3888 (1966).

[88] C. Dress and W. Krauth, J. Phys. A. **28**, L597 (1995).

[89] T. M. Truskett, S. Torquato, S. Sastry, P. G. Debenedetti, and F. H. Stillinger, Phys. Rev. E **58**, 3083 (1998).

[90] M. Adda-Bedia, E. Katzav, and D. Vella, J. Chem. Phys. **128**, 184508 (2008).

[91] M. N. Rosenbluth and A. W. Rosenbluth, J. Chem. Phys. **22**, 356 (1954).

[92] T. Garel and H. Orland, J. Phys. A **23**, L621 (1990).

[93] P. G. Higgs and H. Orland, J. Chem. Phys. **95**, 4506 (1991).

[94] P. Grassberger and R. Hegger, J. Phys.: Condens. Matter **7**, 3089 (1995).

[95] P. Grassberger, Phys. Rev. E **56**, 3682 (1997).

[96] H. Frauenkron, U. Bastolla, E. Gerstner, P. Grassberger, and W. Nadler, Phys. Rev. Lett. **80**, 3149 (1998).

[97] F. T. Wall and J. J. Erpenbeck, J. Chem. Phys. **30**, 634 (1959).

[98] J. M. Hammersley and K. W. Morton, Journal of the Royal Statistical Society. Series B (Methodological) **16**, 23 (1954).

[99] N. C. Smith and R. J. Fleming, J. Phys. A **8**, 929 (1975).

[100] M. Rubinstein and R. H. Colby, *Polymer Physics* (Oxford University Press, Oxford, 2003).

[101] H.-P. Hsu, W. Paul, and K. Binder, Europhys. Lett. **92**, 28003 (2010).

[102] H.-P. Hsu, W. Paul, and K. Binder, Europhys. Lett. **95**, 68004 (2011).

[103] K. Kroy and J. Glaser, New Journal of Physics **9**, 416 (2007).

[104] S. Sturm and K. Kroy (unpublished).

[105] J. C. McDonald, D. C. Duffy, J. R. Anderson, D. T. Chiu, H. Wu, O. J. A. Schueller, and G. M. Whitesides, Electrophoresis **21**, 27 (2000).

Danksagung

Ich möchte mich an dieser Stelle bei all denjenigen bedanken, ohne die es nicht möglich gewesen wäre diese Arbeit zu erstellen.

In erster Linie gilt mein Dank meinem Doktorvater Prof. Dr. Wolfhard Janke, der mir die Arbeit auf diesem spannenden und aktuellen Gebiet ermöglichte. Von seinen langjährigen Erfahrungen konnte ich immer wieder stark profitieren und ein gutes Gespür für akkurates wissenschaftliches Arbeiten erlangen. Ein ausgeglichenes Verhältnis aus Wegweisung und Freiheit eigene Kreativität zu entfalten, schafften eine gute Grundlage, um meinen eigenen Stil beim Bearbeiten wissenschaftlicher Probleme zu finden.

Besonders bedanke ich mich auch bei Prof. Dr. Klaus Kroy für die Einführung in das Gebiet von "Polymeren in Unordnung" im Rahmen meiner Diplomarbeit. In weiteren Diskussionen habe ich neue Denkanstöße und physikalische Einsichten gewinnen können.

Für eine sehr gute Zusammenarbeit und großes Engagement bei Diskussionen und Erstellung von Vergleichsdaten bedanke ich mich bei Johannes Zierenberg. Niklas Fricke danke ich für viele hilfreiche Tipps und Ratschläge beim Entwickeln algorithmischer Ideen und für seine kritischen Kommentare bei Korrekturlesungen. Ich danke der gesamten CQT-Gruppe für einen lockeren, freundschaftlichen Umgang und der Bereitschaft, unkompliziert über physikalische und nicht-physikalische Probleme zu sprechen. Die hervorragende Arbeit unserer freiwilligen Administratoren Hannes Nagel und Martin Marenz, sich mit viel Mühe um das störungsfreie Funktionieren der Technik zu kümmern, hat eine einwandfreie Arbeitsgrundlage geschaffen. Die Sekretärinnen des Instituts für Theoretische Physik, Lea Voigt, Gabriele Menge und Susan Hussack haben mich bei organisatorischen Fragen immer unterstützt.

Ich danke Micha Wiedenmann, der mein Interesse am Programmieren und den Weg in das Gebiet der Numerik mit geprägt hat. Ich schaue dabei gerne auf eine gemeisame WG-Zeit und viele interessante abendliche Diskussionen zurück.

Ganz besonders bedanke ich mich bei Sebastian Sturm. Zuerst für die tiefe Freundschaft, die sich seit der Diplomzeit entwickelt hat und mich in einer persönlichen Lebenskrise während meiner Doktorarbeit mit getragen hat. Weiterhin habe ich durch seinen scharfen Geist und seine überragende physikalische Intuition, sowie die Fähigkeit sich in kürzester Zeit in sämtliche Problemstellungen einzudenken, immer wieder neue Sichtweisen und Ideen bekommen, sowie eine vielzahl an Aha-Momenten erlebt. Von Korrekturlesungen und kritischen Kommentaren zur Dissertation habe ich viel profitiert.

Zu guter Letzt möchte ich mich bei zahlreichen Menschen aus meinem universitären und nicht-universitären Umfeld bedanken, deren Zuwendung zum Gelingen der Arbeit

beigetragen hat. Meiner Freundin Kristin Härtig danke ich für ihre anteilnehmenden Motivationen und Unterstützungen. Ganz besonders bin ich meinen Eltern und meinen Schwestern für ihr tiefes und liebevolles Interesse und ihre Unterstützung in sämtlichen Situationen dankbar.

Für finanzielle Unterstützung bedanke ich mich bei der Graduiertenschule GSC 185 “BuildMoNa”, SFB/TRR102 (Projekt B04) und FOR877 sowie bei der Deutsch-Französischen Hochschule (DFH-UFA).